AUGMENTING STEEL DESIGN WITH DATA-DRIVEN AND ADVANCED ANALYSIS APPROACHES

by

Hyeyoung Koh

A dissertation submitted in partial fulfillment of
the requirements for the degree of

Doctor of Philosophy

(Civil and Environmental Engineering)

at the

UNIVERSITY OF WISCONSIN–MADISON

2022

Date of final oral examination: 12/12/2022

The dissertation is approved by the following members of the Final Oral Committee:

Hannah B. Blum, Assistant Professor, Civil and Environmental Engineering
Pavana Prabhakar, Associate Professor, Mechanical Engineering
Bu Wang, Assistant Professor, Civil and Environmental Engineering
Barry T. Rosson, Professor, Civil, Environmental and Geomatics Engineering
(Florida Atlantic University)

THESIS AUTHORSHIP ATTRIBUTION

This thesis contains material published or submitted for publication, based on the work presented in this thesis, for which I am the main author or co-author.

Journal Papers

Koh, Hyeyoung and Blum, Hannah B. (2022). "A review of current practice for testing by analysis of cold-formed steel structures." *Structures*, 245: 871-880. https://doi.org/10.1016/j.istruc.2022.01.017

Koh, Hyeyoung and Blum, Hannah B. (2022). "Machine learning-based sensitivity of steel frames with highly imbalanced and high-dimensional data." *Engineering Structures*, 259: 114126.
https://doi.org/10.1016/j.engstruct.2022.114126

Koh, Hyeyoung and Blum, Hannah B. (2022). "Data-driven design approaches for normal and high-strength hollow structural section capacities." *Journal of Construction Steel Research* (In preparation).

Koh, Hyeyoung, Rosson, Barry T., & Blum, Hannah B. (2022). "Stability analysis of rotary straightened W-shape members with various stiffness reduction models." *Journal of Construction Steel Research* (In preparation).

Xia, Yu, Koh, Hyeyoung, & Blum, Hannah B. (2022). "Experimental and numerical studies on residual stresses in press-braked advanced high-strength cold-formed steel angles." *Thin-Walled Structures* (In preparation).

Conference Papers

Koh, Hyeyoung and Blum, Hannah B. (2023). Data-driven buckling capacity prediction of normal- and high-strength steel tube section columns. *Proceedings of the Annual Stability Conference Structural Stability Research Council*, Charlotte, NC, 2023.

Koh, Hyeyoung and Blum, Hannah B. (2022). Calibration and validation of the hole-drilling method to determine residual stresses in advanced high-strength cold-formed steel members. *Proceedings of the Cold-Formed Steel Research Consortium Colloquium*, 2022, pp. 1-9.

Koh, Hyeyoung, Rosson, Barry T., & Blum, Hannah B. (2022). Machine learning-based stiffness reduction sensitivity analysis for rotary straightened steel members. *Proceedings of the International Colloquium on Stability and Ductility of Steel Structures*, Aveiro, Portugal, 2022, pp.1-10.

Koh, Hyeyoung, Rosson, Barry T., & Blum, Hannah B. (2022). Stiffness reduction factor requirements for the stability analysis of frames with rotary straightened W-shapes. *Proceedings of the Annual Stability Conference Structural Stability Research Council*, Denvor, CO, 2022, pp.1-19.

Koh, Hyeyoung and Blum, Hannah B. (2020). A state-of-the-art review of testing by analysis in cold-formed steel design. *Proceedings of the Cold-Formed Steel Research Consortium Colloquium*, 2020, pp. 1-9.

Research Report

Committee on Specifications for the Design of Cold-Formed Steel Structural Members, "Review of testing by analysis for potential implementation into AISI standards" (2021). American Iron and Steel Institute (AISI) Specifications, Standards, Manuals and Research Reports (1946 - present). 231.

https://scholarsmine.mst.edu/ccfss-aisi-spec/231

Preprint

Koh, Hyeyoung and Blum, Hannah B. (2021) "Machine learning-based feature importance approach for sensitivity analysis of steel frames.", *engrXiv*. https://doi.org/10.31224/osf.io/mvkf3

ACKNOWLEDGMENTS

Completing my PhD degree was one of the most challenging but exciting adventures in my life. I met many people who supported me throughout my doctoral journey.

This work was carried out under the supervision of Assistant Professor Hannah Blum. I am extremely grateful for all her expert help and advice on the project and her continuous encouragement. Her mentorship has been extraordinarily helpful and inspiring, making me think I want to be a mentor like her. I would also like to thank Professor Barry Rosson for his advice on my project and Associate Professor Pavana Prabhakar and Assistant Professor Bu Wang for serving on my dissertation committee.

I appreciate my fellow group mates Edward Sippel, Yu Xia, and Max Laracuente for their sincere support. I also thank Jacob Zeuske for his help with my experimental project.

I am always thankful to my mom, dad, and brother for their steady support and for believing in me throughout my life. I made this far because of my family.

Finally, I will always be grateful to my husband, Hohyun Yoon, for his immeasurable love, support, and encouragement over the years of my doctoral study. I would not have been able to complete my doctoral degree without him.

CONTENTS

LIST OF TABLES

LIST OF FIGURES

ABSTRACT

An extensive study on steel design using data-driven approaches and advanced analysis approaches was completed to provide insight into the implementation of these approaches for steel design. Data-driven approaches to solving structural engineering problems, such as machine learning techniques, have recently been introduced as efficient tools. However, the reliability and feasibility of the data-driven approaches should be examined before they are implemented into steel design and used in practice. This study discusses problems that could result from the application of data-driven techniques into steel design and provides ways to address the challenges.

Separate from data-driven approaches, advanced analysis approaches such as finite element analysis have been widely used for steel design. As finite element analysis estimates structural responses based on calibrated physics-based models, finite element model updating is critical to provide accurate results. This study also discusses stability design for steel members while considering the effect of residual stresses to improve finite element analysis for steel design.

This dissertation is organized into three broad parts. The first part focused on machine learning-based structural analysis methods. A sensitivity analysis method that estimates the effect of uncertainty on structural system failures was proposed. Two steel frames with different failure modes such as progressive yielding and inelastic buckling were considered. The proposed method was validated against the conventional method which is based on reliability analysis. In addition, the capacity prediction model for steel hollow section columns was developed using interpolation and machine learning approaches. Both experimental and numerical data were utilized for model development, which covered a wide range of geometric and material properties of steel hollow section columns. The

developed model results were compared with the results obtained from the current design provision, AISC 360-16.

The second part focused on the stability design and analysis of steel members with various residual stress distributions. A parametric study of the stiffness reduction methods considering different residual stress distributions of wide-flange sections was conducted. Particularly, an appropriate stiffness reduction factor for rotary-straightened members was examined based on the discussion on the stiffness reduction factor specified in the US specification and the Eurocode. Finite element analyses of columns and beam-columns were performed. Moreover, data-driven predictive models for the capacity of the beam-columns were developed to examine the applicability of machine learning techniques to steel stability design. The predictive performance of the developed data-driven models was compared with the finite element analysis results.

The last part of this study investigates updating numerical analysis for cold-formed steel design. An experimental study on residual stress measurements of advanced high-strength cold-formed steel members was performed. The hole-drilling method was utilized to measure residual stresses and estimate the calibration constants of the material. The residual stress distribution was compared with the sectioning test results, and it was demonstrated that the hole-drilling results are comparable to the sectioning distribution. In addition, a review on testing by analysis for cold-formed steel was conducted. International structural design codes and related research were covered in the review. Recommendations for the use of testing by analysis for cold-formed steel design were provided.

1 INTRODUCTION

1.1 Motivation

Structural steel design involves considering factors that affect the stability of structural members and systems, such as member deformations, second-order effects (P-δ and P-Δ), geometric imperfections, stiffness reductions, and uncertainty in member and system strength and stiffness. Significant advances in computerized structural analysis enabled engineers to perform steel design with the consideration of these factors. Although various sophisticated structural analysis software exist, however, it is difficult to predict the actual capacity or performance of steel members and systems with certainty due to ever-present uncertainties in material and geometric properties. In order to accurately capture structural responses, it must be understood how the uncertainties in all the factors affecting a structure influence structural behaviors.

The current US specification for structural steel buildings ANSI/AISC 360-16 [1] specify the design criteria for stability in Chapter C and inelastic analysis in Appendix 1, which indirectly or directly incorporates the affecting factors into the analysis. As steel fabrication technology is advanced, the current design provisions could result in errors because the influence of new materials and up-to-date manufacturing processes are not reflected in the provisions. For example, (1) although high-strength steel grades have been available due to the advancement of steel manufacturing technology in recent years, the design rules for them are a simple extension of those for normal-strength steels and do not directly address the influence of material yield strength [2]. Moreover, the applicable range of steel grades for hollow section members is limited to the steel grades currently available. (2) Rotary straightening is common practice in the steel manufacturing industry in recent years [3], but residual stresses of

rotary-straightened sections are not fully considered in the stiffness reduction factor used for stability analysis. Consideration of recent trends in steel fabrication technology can enhance accurate steel structural design.

Finite element (FE) analysis has been used to examine the structural responses of steel members and systems with a consideration of the affecting factors to the structural stability. However, if FE analyses are carried out to assess the response of complex structural systems, it may be a challenge for general structural engineers to perform the analyses due to limited advanced software and computational resources. This challenge is exacerbated for large-scale engineering problems which often carry a large quantity of uncertain parameters. Moreover, most structural steel design standards [1], [4]–[7] allow using FE analysis for design (testing), but there is a paucity detailed requirements for design by analysis.

In recent years, data-driven approaches such as machine learning (ML) techniques, have been introduced to predict and assess structural performance and identify structural conditions [8]. ML techniques can discover hidden patterns in data and thus provide predictive models and decision making tools. It is desirable to examine if the ML approaches are reliable and feasible prior to using them for the tasks. To implement data-driven approaches into structural design and analysis and improve the performance of the approaches, the followings should be addressed: (1) data sets for structural design problems are typically imbalanced because structures are designed to have a low probability of failure, where imbalanced data refers to unequal portions of samples in the data such as a small sample size of failures and a large sample size of safe structures. This may lead to the poor predictive performance of ML models. (2) A large number of uncertainty affects the dimension of data, which increases sparsity in data, storage space, and computational cost and time. (3) Investigation on considering both experimental and analytical data for ML model development is still rather limited while including both data sources can improve future

generations of design specifications [9]. In addition, multiple steel design codes [1], [4], [6], [7], [10] allow using both data sources for structural analysis and design. (4) The current steel design provisions [1], [4] have been developed based on a limited range of material and geometric properties, which may lead to errors in estimating the capacity of members that have properties out of range. Accordingly, additional research is needed to address these challenges and therefore provide recommendations on implementing data-driven approaches into structural design.

1.2 Scope and Objectives

The objective of this research is to examine the capability of using data-driven approaches for steel structural design and analysis. As machine learning has recently been demonstrated as an improved tool for demand forecasting, it can be an effective tool for structural analysis to predict structural responses. This research starts with an investigation into the prediction of structural system failure status and capacity of structural members. In addition, investigations on updating finite element analysis for hot-rolled and cold-formed steel design are presented.

The investigation into the machine learning-based sensitivity study is focused on identifying significant uncertainties in system failures. The research proposed the sensitivity analysis methodology that addresses how to develop classification models and examine the effect of uncertainty on system failures. Two planar steel frames with different failure modes, which were inelastic buckling and progressive yielding, were considered. The steel frames incorporated a low probability of failures and uncorrelated properties between structural members, thus the dataset was high-dimensional and extremely class-imbalanced. The ways to overcome these data-related challenges were covered. The proposed approach was validated against the conventional sensitivity analysis method, which

is based on reliability analysis and therefore requires repeated evaluations of the performance function to examine the effect of uncertainty. A discussion on the comparisons of the results from the machine learning-based sensitivity analysis and the reliability-based sensitivity analysis was presented.

In addition to the system-level investigation in the above work, data-driven approaches were employed to predict the capacity of steel members. Since the current design rules for hollow sections have a limited applicable range of yield strength, especially for high-strength steel, this investigation developed a consistent prediction method for predicting the buckling capacity of steel square and rectangular hollow section columns, which covers a wide range of steel grades, geometric properties, and forming processes. Both experimental and numerical data were used for model development. An interpolation model and two ML algorithms including Extreme Gradient Boosting [11] and Multi-layer Perceptron were implemented to develop buckling capacity prediction models. In addition to the capacity prediction, the effect of parameters was examined to interpret the relationships between the input and output parameters and thus capture the underlying physics. This research discussed the existing steel design rules [1], [4] for hollow section columns and provided recommendations that can improve the design provisions since the database used for the proposed model covered a wide range of material and geometric properties.

The research into rotary-straightened members focused on the stability analysis of columns and beam-columns by assuming different residual stress distributions in hot-rolled wide-flange sections. This investigation conducted a parametric study that evaluates multiple stiffness reduction models that consider different residual stress patterns for W-shapes including the patterns adopted by the steel design codes [1], [4] and that for rotary-straightened sections. Beam element FE analyses were carried out

in MASTAN2 [12], and second-order inelastic analyses were conducted. A range of W14 sections including both narrow and wide sections was considered in the analysis. The limit load capacity of hot-rolled and rotary-straightened members was compared to examine the effect of assumed residual stress patterns on the capacity. Moreover, correlation relationships between cross-section dimensional parameters of W-shapes and the limit loads were investigated. A discussion on the current stability design provision of AISC 360 [1] was provided to examine if they are appropriate for the analysis of rotary-straightened members.

Building upon the parametric study in the above work, data-driven models were developed to explore the applicability of a data-driven approach for the stability analysis of rotary-straightened members. ML regression models were developed to predict the limit capacity of beam-columns with different residual stress patterns. Two separate ML models for beam-columns under major or minor axis bending were developed based on the FE analysis results obtained from the parametric study. A detailed procedure to develop the regression models customized for the task of this work was provided. The beam-column limit loads derived from the developed data-driven models and the FE analysis were compared, and their prediction accuracy was discussed.

In addition to the data-driven research for structural steel design and analysis, investigations on cold-formed steel structures were conducted to update the current FE analysis method for cold-formed steel design: (1) a physical experiment on residual stress measurements of advanced high-strength cold-formed steel (AHSS) members; This experimental investigation quantified residual stress distributions of lipped angle members manufactured from an AHSS sheet. The hole-drilling method was utilized to measure residual stresses. The calibration constants, which are used to estimate residual stresses measured by hole-drilling, for AHSS material were estimated to improve the accuracy of the hole-drilling method.

The residual stress distributions of identical AHSS angles obtained from the hole-drilling method and the sectioning method were compared. (2) review on testing by analysis (virtual testing) for cold-formed steel; This review project aims to provide an overview of testing by analysis in existing structural design standards for cold-formed steel, structural steel, and concrete as well as recent research which covered good examples of testing by analysis. Recommendations for the use of testing by analysis based on the design standards and research were presented, which will assist with accurate and efficient design using testing by analysis.

1.3 Dissertation Layout

This dissertation consists of six chapters in which each chapter presents one aspect of the overall project.

Chapters 2 through 4 and Chapter 7 are journal papers that have either been published or are under review. Chapters 5 and 6 are papers in conference proceedings. Chapter 8 summarizes the results and conclusions of the projects covered in this dissertation and future work. It should be noted that the overall literature review is not separately provided because studies on a literature review relevant to each project are presented within the individual chapter. A brief summary of the content presented in each chapter is as follows:

Chapter 2 presents the proposed machine learning-based sensitivity analysis method for estimating the effect of uncertainty on steel frame failures. This chapter provides details on the proposed method, such as the mechanism of the approach, used machine learning techniques, data description, challenges in using data for structural engineering tasks, and validation of the proposed approach against a conventional method.

Chapter 3 contains a data-driven approach for capacity prediction of structural steel hollow sections. This chapter covers the design rules for

square and rectangular hollow section columns provided in AISC 360 [1] and Eurocode [4], data information, applied machine learning algorithms, the predictive performance of the developed models, and discussion on the proposed predictive model and the current design provisions.

Chapter 4 provides a parametric study on the stiffness reduction models for hot-rolled and rotary-straightened steel members. This chapter contains the background of four stiffness reduction models which consider different residual stress patterns, finite element model description, comparison of limit loads of columns and beam-columns, correlation investigation between input and output parameters, and discussion on the existing stiffness reduction models.

Chapter 5 presents a machine learning approach to the stability analysis of rotary-straightened members. This chapter discusses the stiffness reduction models, details on data collection and model development, and prediction results. The results were compared with the capacity derived by finite element analysis, and their accuracy was discussed.

Chapter 6 provides details on an experimental study on residual stress measurement of high-strength cold-formed steel members. This chapter addresses details on the experimental program including material properties, specimen fabrication, hole-drilling test procedure, and experimental calibration. Experimental results provide a residual stress distribution of the lipped angle. The results are compared with the results derived from the sectioning method.

Chapter 7 provides the overall review on testing by analysis for cold-formed steel structures. The review covers the existing design standards, which provide the numerical test-based design for cold-formed steel as well as other construction materials, and recent research. Recommendations for the use of testing by analysis are finally presented.

Chapter 8 provides a summary of the research, conclusions, and recommendations for future research.

2 MACHINE LEARNING-BASED SENSITIVITY OF STEEL FRAMES WITH HIGHLY IMBALANCED AND HIGH-DIMENSIONAL DATA

Koh, Hyeyoung and Blum, Hannah B. "Machine Learning-Based Sensitivity of Steel Frames with Highly Imbalanced and High-Dimensional Data." *Engineering Structures*, 259 (2022): 114126.
https://doi.org/10.1016/j.engstruct.2022.114126

Abstract

The machine learning-based feature selection approach is presented to estimate the effect of uncertainties and identify failure modes of structures that incorporate a low failure probability and high-dimensional uncertainties. As structures are designed to have few failures, a dataset classified based on the failure status becomes imbalanced, which poses a challenge for the predictive modeling of machine learning classifiers. Moreover, in order to improve the accuracy and efficiency of the model performance, it is necessary to determine the critical factors and redundant factors, especially for a large feature set. This study benchmarks the novel method for sensitivity analysis by using datasets that exacerbate the problems involved in class imbalance and large number of input features. This study investigates two planar steel frames with spatially uncorrelated properties between structural members. Geometric and material properties are considered as uncertainties, such as material yield stress, Young's modulus, frame sway, and residual stress. Six feature importance techniques including ANOVA, mRMR, Spearman's rank, impurity-based, permutation, and SHAP are employed to measure the feature importance and identify parameters germane to the prediction of structural failures. Logistic regression and

decision tree models are trained on the important feature set, and the predictive performance is evaluated. The use of the feature importance approach for structures with a low probability of failure and a large number of uncertain parameters is validated by showing identical results with the reliability-based sensitivity study and appropriate predictive accuracy.

2.1 Introduction

Structures have numerous variations and uncertainty in their properties, which may affect the load carrying capacity. A reliability-based sensitivity analysis estimates how uncertainty in the input parameters affects system performance by analyzing the dependence of the failure probability on the inputs, which requires repeated evaluation of the performance function, resulting in significant computational cost and time. This challenge is exacerbated for large-scale engineering problems which often carry a large quantity of uncertain parameters, which for machine learning is referred to as a large dimension in a dataset. Researchers have made efforts to improve the computational efficiency of sensitivity analysis. For example, Wu [13] proposed the adaptive importance sampling approach, which improves computational efficiency by minimizing oversampling in the safe region of the limit-state surface. The score function approach proposed by Rubinstein and Kroese [14] estimates all sensitivities by the gradient and derivative of parameters. The score function method does not require additional simulations for reliability sensitivity analysis. Torii et al. [15] applied polynomial expansions to the performance function and its derivatives for the probability of failure sensitivity analysis. Proppe [16] introduced the local reliability sensitivity analysis using the moving particles method, which estimates the failure probability based on the new locations of the moved data points in the design space.

For high-dimensional data, it is difficult to make a right decision on which features should be selected because of the curse of dimensionality [17], which refers to the phenomenon arising from too many feature variables that increase sparsity in data, storage space, and computational costs. The principal component analysis (PCA) [18], [19] is commonly used to mitigate high-dimensionality. However, PCA reduces the dimension by utilizing the correlation structure of random variables, thus it does not perform well for independent variables. Feature selection is one of the most crucial techniques in machine learning especially for high-dimensional datasets [20] because it can filter out redundant or irrelevant features. The success of feature selection techniques, which enables meaningful predictors to be obtained and derives results faster, has been proven by many researchers in various fields of study [21]–[24]. However, the high-dimensional problems often accompany other issues emerging from the nature of data, such as imbalanced classification [25], [26]. Class imbalance refers to a problem in machine learning classification where each class accounts for an unequal portion of the data, which may lead to poor predictive performance. If a classifier is applied on an imbalanced dataset, the classifier is biased towards the majority class [27] and a trivial classifier learns the majority class only and attributes the label to all instances, thereby no instance for predicted minority class occurs [28]. As the failure probability of structures can be estimated by the number of failures (minority class) out of the total number of simulations including failure and safe structures (majority class), datasets for structural design problems become extremely imbalanced. When a structure is designed to have little load redistribution, the target reliability index β_T is 2.7 [29], which corresponds to the failure probability P_f of 3.5×10^{-3}, derived from $\beta = -\Phi^{-1}(P_f)$, where Φ^{-1} = inverse standard normal cumulative density function. Moreover, ASCE 7 [30] suggests using a target reliability index between 3.0 and 4.0 for structural components subjected to dead, live, and

other loads except earthquake loads, depending on the risk category from I through IV where category I represents the lowest level of risk to human life. Likewise, a classification dataset for structural design problems will be severely imbalanced, which is indicated from the values of β_T and P_f. As structural design problems often include an imbalanced dataset, it is challenging to select an adequate statistical metric that provides informative and truthful results. This emphasizes that the use of feature selection techniques on structural engineering data with high-dimensionality and class imbalance should be explored, in which there are rather limited studies.

In recent years, the interest in artificial intelligence has been growing in the field of structural engineering because it provides efficient solutions to the problems in this field relative to traditional computational techniques. The use of artificial intelligence in steel structural design has been focused on artificial neural networks for design of steel members or connections such as compression members [31], steel panels [32], steel connections [33], [34], and cold-formed steel channels [35]. For reinforced concrete (RC) members or systems, machine learning techniques are implemented to predict structural responses such as the shear capacity of fiber RC beams [36], structural response of RC deep beams [37], RC slabs [38], and RC columns under fire resistance [39]. Data-driven machine learning approaches were used for fragility, risk, and vulnerability assessment of a special steel moment resisting frame building [40], [41] and RC building frames [42]. Also, machine learning approaches were used to identify failure modes and rank the significant factors affecting the failure mode of RC members [43], RC frames [44], and steel frames [45]. Data-driven design approaches for structural design have recently been developed, but it is desirable to determine if the approaches are viable before they are implemented in practice. To that end, this study benchmarks feature selection techniques on the structural analysis data that incorporate a high

imbalanced ratio, a larger set of uncertainties, and more data points. The importance of benchmark studies has been emphasized in the machine learning community [46], [47]. Machines carry out tasks based on learning from a given dataset, therefore the best algorithm will not be the same for all the datasets [48]. Therefore, benchmarking of the feature importance approach must be accomplished to draw conclusions for the use of the approach in a wide range of structural systems.

Koh and Blum [45] introduced the machine learning-based feature selection framework for structural sensitivity analysis. This framework measures the feature importance of all parameters and ranks them to determine the important or redundant parameters for the prediction of system failure. Two planar steel frames were investigated with the consideration of uncertainties that affect steel frame behaviors, such as yield stress, Young's modulus, frame sway, and residual stress. The frames have different failure modes and the ultimate frame strength obtained from finite element analysis was used as the response variable. The feature rankings derived by four feature importance techniques showed identical order of factors resulting in the largest failure probability, which matched those obtained from the conventional sensitivity analyses. It was demonstrated that the general procedure of the proposed feature importance method can be used for sensitivity analysis. The approach is efficient because all feature importances are estimated from a single training. Moreover, variable space can be reduced by removing irrelevant parameters to improve both computational efficiency and accuracy.

The steel frames investigated in this study have the same layout as for Koh and Blum [45] but have a different spatial correlation scenario. Unlike the correlated scenario where all columns (or beams) have the same properties, this study applies the uncorrelated scenario where all structural members have different properties. Sensitivity studies on structural systems with uncorrelated properties inform which specific structural

member largely influences the frame failure. However, the increased number of uncertainties poses additional challenges in performing reliability sensitivity studies, which require repeated evaluations of the performance function. Regarding the feature importance approach, a large set of uncertainties would make it difficult for the feature importance method to derive consistent rankings between various techniques. In general, the uncorrelated scenario contains a fewer number of failures than the correlated scenario [49], therefore the class-imbalanced ratio increases for the uncorrelated scenario. This study aims to examine how the feature importance approach performs for a structural sensitivity analysis when fitting high-dimensional and extremely class-imbalanced data, which presents challenges in model training for structural engineering problems.

This study implemented six existing feature importance methods to measure the importance score. There are typically two categories in feature importance methods: (i) data analysis techniques that directly analyze the data without model fitting to measure the feature importance and (ii) model analysis techniques that identify important features based on predictions from trained models [50]. (1) ANOVA (Analysis of variance), (2) mRMR (minimal-redundancy-maximal-relevance) [51], and (3) Spearman's rank correlation coefficient [52] are utilized as data analysis techniques. This study used a decision tree classifier [53] to measure the feature importance by using model analysis techniques. Model analysis techniques include two feature importance methods, which are (4) impurity-based importance and (5) permutation importance, and (6) SHAP (SHapley Additive exPlanations) [54]. Based on the measured feature importance, logistic regression [55] and decision tree [53] models are fitted to predict whether a steel frame fails. The predictive performance is evaluated by specificity, recall, and the Matthews correlation coefficient [56]. The results are compared with the reliability-based sensitivity analysis results to validate the feature importance framework. Finally, the best

feature importance technique depending on the failure modes is discussed.

2.2 Machine learning techniques for the feature importance approach

The primary task of this study is to estimate the effect of uncertainties on failure modes of steel frames using the machine learning-based feature importance approach. In a high-dimensional dataset, it is important to determine the relevant features and remove the redundant features in an effort to prevent overfitting of a model and reduce training time, thereby improving the model performance and computational efficiency. This study measures the feature importance and compares the critical features between the feature selection methods. Once the feature rankings are derived from the feature importance techniques, a classification model is employed to predict the failure status of a structure by increasing the size of the feature set used for training. The model accuracy of each feature importance method is measured to determine how many features are informative or irrelevant for identifying structural failures. The feature ranking as well as the model performance are considered when evaluating the feature importance techniques for structural sensitivity analysis.

2.2.1 Feature importance techniques

Feature selection involves reducing the number of feature variables to mitigate the curse of dimensionality. Feature selection improves the computational efficiency of the machine learning model and reduces the volume of feature space, which is a significant issue in a large dataset. Moreover, the prediction performance can be improved by removing redundant features that have a negative or no effect on prediction. There is a large number of feature selection techniques that estimate a feature importance score

and provide the feature ranking based on the score of all features. This study implemented four existing feature importance methods to identify the most and least important features in steel structures

ANOVA

The ANOVA test compares the relationship between features and response variables based on the value of F-statistic. The feature importance score J_{ANOVA} is equal to the value of F-statistic. The score can be calculated by Eq. 2.1:

$$J_{ANOVA}(x_i) = \frac{\sum_{m=1}^{M} N_m(\bar{x}_m^{(i)} - \bar{\bar{x}}^{(i)})/(M-1)}{\sum_{m=1}^{M} (N_m - 1)s_m^2/(N-1)} \tag{2.1}$$

where N_m = the number of instances that $y = m$, $\bar{x}_m^{(i)}$ = the sample mean of feature x_i for class m, s_m^2 = the sample variance of feature x_i for class m, $\bar{\bar{x}}^{(i)}$ = the grand mean of feature x_i, M = the number of classes, $M = 2$ in a binary dataset, N = the total number of instances. The importance score is the ratio of between-group variance to within-group variance, thus this technique assesses the difference between the mean values of the corresponding feature x_i between the classes. A higher value of the F-statistic indicates a larger difference between the mean values among the classes, thus the feature has a significant effect on the classes. Note that ANOVA is always positive because it is based on variance, which is always positive.

mRMR

The mRMR technique [51] ranks features by mutual information, which considers both relevance and redundancy of features. The feature relevance indicates a correlation with the response variable, and the feature redundancy represents the information duplicated between features. As

the dataset is discrete not continuous, the mutual information difference (MID) is used as the mRMR criterion, which can be estimated by Eq. 2.2:

$$J_{mRMR}(x_i) = I(x_i, y) - \frac{1}{|S|} \sum_{x_j \in S} I(x_i, x_j) \tag{2.2}$$

where $|S|$ = the feature set size (number of features), S = a feature set, x_j = a feature not selected in the set S, and I = the mutual information. The first term represents the relevance of the feature x_i about the response variable y. The relevance is determined from the outcome variable prediction. The second term estimates the redundancy, which is measured within the selected features x_i and x_j. By intuition, a feature with a negative J_{mRMR} value has a small relevance and large redundancy, therefore, including it in model training would decrease the predictive performance of the model.

Spearman's rank

The Spearman's rank correlation coefficient [52] measures a monotonic nonlinear relationship between two variables, a feature x_i and the response variables y. The measured coefficient varies between -1 as the perfect negative correlation and +1 as the perfect positive correlation. A feature with the largest absolute value is considered the most important.

Impurity-based importance

Impurity-based importance considers the node impurity in a tree to estimate the importance. A node containing instances of one class only is pure while a node with greater than or equal to two classes is impure. The impurity-based feature importance can be computed by Eq. 2.3 [57], which measures the impurities at a node j before and after splitting and then averages the impurity decrease by $N^{(i)}$, which is the number of nodes

in a tree split based on x_i. A negative feature importance value ($J_{impurity}$) indicates that including it in model training would decrease the predictive performance of the model.

$$J_{impurity}(x_i) = \frac{\sum_{i \in N^{(i)}} (\text{Impurity before node } k - \text{Impurity after node } k)}{|N^{(i)}|} \tag{2.3}$$

Permutation importance

Permutation importance measures the importance by removing a single feature column in a dataset. First, a tree-based algorithm is fitted to obtain the baseline model performance. After training the model, a single feature column is randomly shuffled to remove the association between the feature and the response variable. The performance of the permuted model is evaluated and compared with the baseline model performance. The difference in accuracy is considered to be the importance score as shown in Eq. 2.4. The feature that results in the largest Mean Decrease in Accuracy (MDA) is the most important. The permutation method provides a negative score when a feature has no effect and shuffled data are shown to be more accurate.

$$\begin{aligned} J_{permutation}(x_i) = &\text{ accuracy for dataset without permutation} \\ &- \text{accuracy for permuted dataset of } x_i \end{aligned} \tag{2.4}$$

SHAP

The SHAP algorithm [54] identifies how much each feature contributes to the response variable based on the predictions for linear models trained on all feature subsets. The difference of the predictions from the model $f_{S \cup \{i\}}$ trained on a feature subset S including a feature x_i and another model f_S

excluding x_i is interpreted as the effect of x_i. The SHAP importance score is a weighted average of all possible differences, as shown in Eq. 2.5:

$$J_{SHAP}(x_i) = \sum_{S \subseteq F \setminus i} \frac{|S|!(|F| - |S| - 1)!}{|F|!} [f_{S \cup \{i\}}(x_{S \cup \{i\}}) - f_S(x_S)] \tag{2.5}$$

where F = the set of all features, and S = all feature subsets without x_i. Since all possible subsets are used to measure the SHAP score, the computation time of the SHAP algorithm is expensive because the model is repeatedly trained on all possible feature subsets. SHAP measures the influence of features in terms of the prediction of either positive (minority class) or negative (majority class) outcomes.

2.2.2 Classification-based techniques

Two classification models from different classification model families were used to evaluate the performance. The selected models are logistic regression [55] from the regression-based classifier family and a decision tree [53] from the tree-based classifier family. Decision tree and logistic regression classifiers are fast and use a small amount of memory for training and prediction [58], indicating that they are appropriate for high-dimensional data and easy to use and interpret [8].

Logistic regression

Logistic regression [55] is trained using the top-k features obtained from the feature importance methods, where k = the number of important features. Logistic regression is used for the classification problems, which uses the logistic sigmoid function and transforms the output into a probability value between 0 and 1 as follows in Eq. 2.6:

$$P(Y = m) = \frac{1}{1 + \exp(-(w_0 + \sum_{i \in n} w_i x_i))} \tag{2.6}$$

where $P(Y = m)$ is the probability of presence of Class m; Class 0 represents no failure and Class 1 represents failure in this study, w_i = regression coefficients, x_i = input features, and n = the number of input features.

A linear function is embedded in the logistic regression model, which is given as the natural logarithm of the ratio of $P(Y = 1)$ to $P(Y = 0)$. Logistic regression estimates the regression coefficients by minimizing the value of the ratio shown in Eq. 2.7.

$$\log(\frac{P(Y = 1)}{1 - P(Y = 1)}) = \log(\frac{P(Y = 1)}{P(Y = 0)}) = w_0 + \sum_{i \in n} w_i x_i \tag{2.7}$$

Feature scaling was performed on the datasets used for training a logistic regression classifier, which is sensitive to the location of data points. A decision tree is scale-invariant because it trains the model based on decision rules. Therefore, the datasets for the logistic regression algorithm are transformed to a standardized scale, which has a mean value = 0 and standard deviation = 1.

Decision tree

A tree-based classifier, decision tree [53], is used to measure the performance in addition to estimate the feature importance score of the model analysis techniques including impurity-based, permutation, and SHAP. Decision tree continuously splits the data according to a certain parameter such as impurity or entropy. Decision rules for splitting and the leaf nodes are the final outcomes of the decision tree. The decision tree algorithm used in this study splits the nodes based on entropy (Eq. 2.8) until all leaves are pure:

$$H(S) = -\sum_{m=1}^{M} p_m \log_2 p_m \tag{2.8}$$

where M = the number of classes and p_m = the probability of Class m occurring in the data.

2.2.3 Evaluation metric

After training a model with a training set, the model performance is evaluated by using a test set, which was not involved in training. A confusion matrix provides a visualization of the model performance and it is used as a performance measurement for a machine learning classification problem. The confusion matrix for binary classification consists of the four different cases as shown in Eq. 2.9:

$$M = \begin{pmatrix} TP & FN \\ FP & TN \end{pmatrix} \tag{2.9}$$

where True Positive (TP) = the number of actual positives that are correctly predicted positives, True Negative (TN) = the number of actual negatives that are correctly predicted negatives, False Negative (FN) = the number of actual positives that are incorrectly predicted negatives, and False Positive (FP) = the number of actual negatives that are incorrectly predicted positives.

Several statistical rates can be computed based upon the values given in the confusion matrix. For example, Accuracy is defined as the ratio of the correctly predicted instances to all the instances, $(TP + TN)/(TP + TN + FP + FN)$. F1-score represents the harmonic mean of precision and recall, where precision is $TP/(TP + FP)$ and recall is $TP/(TP + FN)$. Accuracy and F1-score are the most popular metrics, but they lead to the overoptimistic inflated measures especially on imbalanced datasets [59] because several classifiers learn towards the majority class [27], [28]. For

instance, when a dataset has 0.01% minority class and a model predicts all minority classes incorrectly, i.e., all data points are classified as the majority class, the model accuracy is 99.99%, which is nearly perfect. In structural engineering practice, however, it is critical to identify structural failures (the minority class) rather than safe structures (the majority class), thereby necessitating using the right metric that can correctly predict both classes in a binary classification.

This study employed three statistical measures to evaluate the performance including specificity, recall, and the Matthews correlation coefficients (MCC) [56]. For imbalanced class distributions, the majority class is typically referred to as the negative outcome and the minority class is assigned to the positive outcome. Therefore, structural failure is the positive outcome and no failure is the negative outcome. Specificity is the probability that an actual negative will test negative and is calculated by $TN/(TN + FP)$, which is the true negative rate. Specificity refers to how well a model identifies the frames which have no failure. Recall, also called the true positive rate, is the ratio of correct positive predictions to the total positive examples and is computed by $TP/(TP + FN)$. Recall informs how many positive predictions are missed from the prediction. The MCC is a reliable measure for imbalanced classification problems because it takes into account the ratio between positive and negative outcomes, which are not considered in both specificity and recall. The MCC is independent of the class imbalance, thus can reduce misleading results on imbalanced datasets [28]. The value of MCC varies between -1 and 1, similar to other correlation coefficients. The score is high only when all four categories in the confusion matrix are generated correctly. The MCC is computed by:

$$MCC = \frac{TP \cdot TN - FP \cdot FN}{\sqrt{(TP + FP) \cdot (TP + FN) \cdot (TN + FP) \cdot (TN + FN)}} \tag{2.10}$$

2.3 Reliability-based sensitivity analysis

Existing steel design specifications [1], [4], [7], [10] provide guidance for inelastic analysis, also referred to as advanced analysis and GMNIA, which directly considers geometric and material nonlinearities and includes uncertainty in system, member, and connection strength and stiffness. Estimating structural performance with certainty is challenging because of the inherent uncertainty in a structural system which affects system performance. Reliability-based sensitivity analysis estimates the effect of an input variable by evaluating the structural performance with the variable under consideration as random while all other variables are at their nominal values. After repeated simulations for each property under consideration, the probability of failure P_f is estimated by n/N [60] where n = number of simulations which resulted in failure and N = total number of simulations. The system reliability index β is computed based on P_f. Unlike a reliability analysis which takes into account multiple random variables simultaneously, a sensitivity analysis considers only one random variable per simulation set to examine how the random variable affects the system behavior, therefore the strength distribution might have a smaller COV compared to that from a reliability analysis. The normal probability plot [61] is used to estimate P_f and β when no failure cases occur.

Researchers have investigated the system reliability of various steel structures estimated by considering uncertainties in the systems. A reliability sensitivity study was conducted on two steel frames by considering uncertainties in yield strength, elastic modulus, residual stress, and sway and bow imperfections [62]. Szyniszewski [63] investigated the effect of random geometric imperfections on progressive collapse propagation by analyzing 3-D steel framed buildings with uncorrelated geometric imperfections between structural members. Shayan et al. [64] presented a probabilistic study regarding modeling random geometric imperfections on regular and irregular sway and braced planar steel frames. Thai et al.

[65] evaluated the system reliability of steel frames with semi-rigid connections. Uncertainties in gravity loads, material properties, cross-sectional properties, and connection properties were included in the reliability analysis. Zhang et al. [66] examined the system reliability of five steel structures including a beam, a portal frame, and three low-rise frames. Randomness considered in the analysis includes gravity loads, material properties, cross-sectional properties, and sway imperfection. Cardoso et al. [67] calibrated the system reliability of cold-formed steel portal frames with uncertain parameters in material properties, cross-section thickness, joint properties, and geometric imperfections.

2.4 Data collection

2.4.1 Structural system

Two example steel frames designed according to AISC 360 [1] were analyzed in this study, which have the same layout but different member sizes and loads, adopted from [68]. Studies of these frames have been published in Zhang et al. [66] for Frame 1 and Buonopane and Schafer [69] for Frame 2. Fig. 2.1 and Table. 2.1 summarize the details of the example frames including geometry and applied loads. The frames were modeled in OpenSees [70] with displacement-based and fiber-type elements, which were subdivided into 16 elements per member. Connections were assumed to be fully-rigid, thereby disregarding any potential flexibility in the connections. All cross-sections contained the residual stress with the Galambos and Ketter pattern [71] and the fiber distribution as shown in Fig. 2.3. The nominal peak compressive residual stress value was $0.3F_{yn}$, where F_{yn} = nominal material yield strength of 248 MPa (36 ksi). Initial sway imperfection of $h/500$ was given to all columns in the frame, where h is the story height.

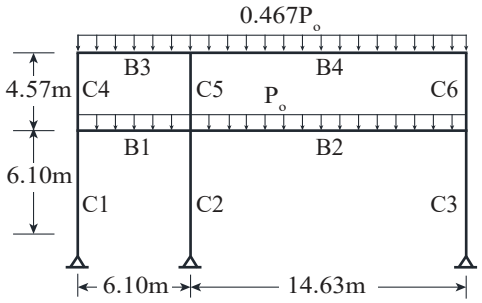

Figure 2.1: Frame layout

Second-order inelastic push-down analyses were performed, in which the applied load ratio is increased until the frame collapses. The finite element (FE) analyses were first conducted with all nominal properties to determine the nominal ultimate load ratio λ, which is the ratio of ultimate to factored design loads. Fig. 2.2 illustrates the load-deformation curves and the location of highly yielded zones ($\geqslant$ 75% of cross-sectional area yielded). The numbers represent the ratio of yielded cross-sectional area. The ultimate load ratios λ obtained from the analyses are 1.08 for both frames,which indicated that they have a limited capacity for load redistribution. Frame 1 failed by the instability (global inelastic buckling) of the slender ground floor column C2. Member C2 was partially yielded (53.5%) at the collapse limit, while the other members were within their elastic limits at failure, which matched the results presented in [66]. Frame 2 failed from a gradual sequence of yielding, whereby multiple members had highly yielded zones along the member length, which were B1, B2, B3, B4, C5, and C6.

To verify the accuracy of the FE models, the analysis output with nominal properties was compared to that from the previous studies [66], [69]. Load-deformation curves and yield ratios from Zhang et al. [66] and the model in this study (Frame 1) were well matched to each other as shown in Fig. 2.2a, where the number in parentheses indicates the

Table 2.1: Member sizes and applied loads

Element	Frame 1	Frame 2
C1	W6 × 20	W12 × 14
C2	W14 × 82	W14 × 99
C3	W14 × 68	W14 × 82
C4	W6 × 8.5	W10 × 12
C5	W14 × 145	W14 × 109
C6	W14 × 145	W14 × 109
B1	W30 × 132	W27 × 84
B2	W36 × 182	W36 × 135
B3	W24 × 55	W18 × 40
B4	W30 × 116	W27 × 94
Loads (P_o)	111.86 kN/m	109.45 kN/m

yield ratio recorded from Zhang et al. [66]. Next, a reliability analysis considering the effect of uncertainties in geometric and material properties in addition to applied loads was also performed. The variations of the loads are provided in Ellingwood et al. [72]. The resulting β value was 2.79, which had an error of 1.4% with the β results from the previous study [66], thereby validating the model for Frame 1.

As for Frame 2, it was confirmed that the Frame 2 model can capture the load-displacement curve when it follows the model description provided in Buonopane and Schafer [69], where residual stresses and sway imperfections were not included. As shown in Fig. 2.2b, the model without consideration of residual stress (rs) and sway imperfections (red line) had a load ratio of 1.70, which is within the range between the maximum and the minimum load ratios of the Buonopane and Schafer results (black line). This validates the modeling approach for Frame 2 with the previously published results [69]. After validating the model with nominal properties, residual stresses and sway imperfections were added into the model for Frame 2 and the resulting load ratio was 1.08 (blue line). This indicates that residual stresses and sway imperfections influence the capacity of Frame 2.

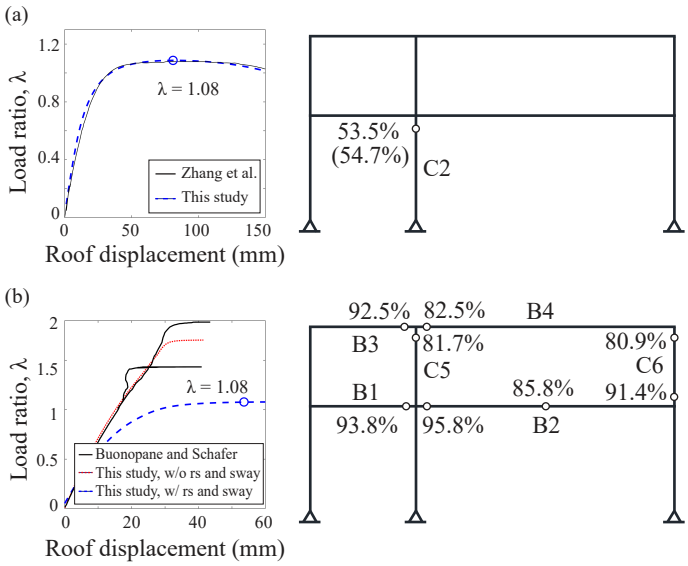

Figure 2.2: Load-deformation curves and location of highly yielded zones: (a) Frame 1 (b) Frame 2

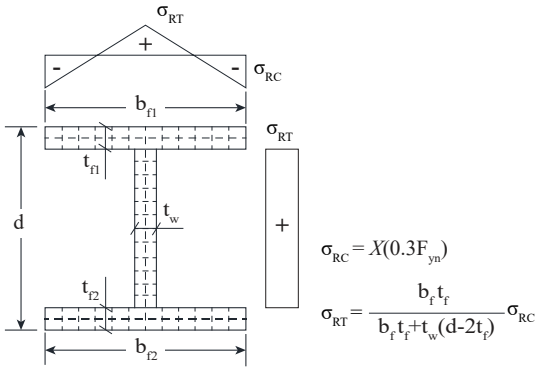

Figure 2.3: Residual stress pattern and fiber distribution

Table 2.2: Description of feature variables

Variable	Mean	COV	Distribution	References
F_y	$1.1F_{yn}$	0.06	Lognormal	Bartlett et al. [73]
E	E_n	0.04	Lognormal	Bartlett et al. [73]
Sway imperfection	1/770	0.875	Lognormal	Lindner and Gietzelt [74]
X	1.064	0.27	Normal	Shayan et al. [75]

2.4.2 Uncertainty

The Monte Carlo sampling method is used to generate samples of the uncertainties in material yield strength F_y, modulus of elasticity E, sway imperfection, and residual stress. Table 2.2 summarizes the statistical information of the uncertainties with referenced literature. Yield strength and elastic modulus are modeled following the distributions published in Bartlett et al. [73]. Nominal yield strength F_{yn} of 248 MPa and nominal elastic modulus E_n of 200 GPa are utilized to determine the mean value of yield strength and elastic modulus, respectively. The distribution of sway imperfection followed the distribution of Lindner and Gietzelt [74]. The scale factor of maximum compressive residual stress X is modeled as a normal distribution provided in Shayan et al. [75]. The random scale factor X was multiplied by $0.3F_{yn}$ to consider the uncertainty of residual stress magnitudes in compression. The peak tensile residual stress (σ_{RT}) within a cross section was determined by the geometry and the peak compressive residual stress (σ_{RC}), as shown in (Fig. 2.3). σ_{RT} includes X indirectly because it is calculated based on equilibrium. Once σ_{RC} and σ_{RT} are determined, the rest of the residual stresses in the cross section were set based on the residual stress pattern. The residual stress condition is constant along the length of a member. To account for the maximum number of uncertainties and to investigate the effect of each parameter on structural failure, the frames are assumed as spatially uncorrelated, i.e., all structural members have different random properties.

Cross-sectional imperfections, including web and flanges widths and thicknesses, were considered as random variables in preliminary studies using statistical information provided in Melcher et al. [76]. However, there were no observations of failure until 10^6 simulations were performed. An extremely small COV for the strength distributions occurred, likely due to the small COVs of the distributions of cross-section dimensions. This indicates a negligible effect of randomness in cross-sectional dimensions on the studied planar frames.

2.4.3 Dataset

As the structural members are uncorrelated, each individual member had a different realization of the random properties. In other words, there were no identical random values of the input variables shared between all beams or all columns. Input feature variables consist of thirty-three different parameters including ten different values each of yield strength, elastic modulus, and residual stress and three sway imperfections assigned to the three column locations – left, center, and right. The response variable is the binary outputs based on the ultimate load ratio λ obtained from the FE analysis containing random realizations of the input parameters. As the frame is designed according to the inelastic method provided in AISC 360 [1], this study applied the probability-based limit state design criteria $\lambda = 1.0$ as the classification criteria of the dataset. If the ultimate load ratio is less than 1.0, the frame experiences a structural failure and the observation is assigned to Class 1. An ultimate load ratio greater than or equal to 1.0 indicates that the frame is safe and the sample set is assigned to Class 0, which means no failure. A total of 500,000 simulations were run for Frame 1 and 1,000,000 simulations for Frame 2. A small percent of simulations had convergence issues and were excluded from the datasets. In total, Frame 1 had 309 failures (Class 1) out of 498,050 labeled data points. Frame 2 had 127 failures, which is less than that of Frame 1, out of

the total number of simulations, 903,272.

As discussed previously, a classification dataset for structural design problems will be severely imbalanced, based on the selection of β_T and the corresponding P_f. A no-information rate, which describes how much the dataset is imbalanced, is calculated by $\max(n_{Class\,0}, n_{Class\,1})$ / $(n_{Class\,0} + n_{Class\,1})$, where $n_{Class\,0}$ is the number of Class 0 examples and $n_{Class\,1}$ is the number of Class 1 examples. Therefore, the no-information rates of Frame 1 and Frame 2 are 99.94% and 99.99%, respectively, approximately equal to 100%.

The data points for each frame were randomly assigned into equal training and test sets, for a 50%-50% split between training and testing datasets for each frame. As a general rule of thumb, a train-test split for evaluating machine learning algorithms is 80% - 20% or 70% - 30%, which has been utilized in previous studies [35]- [44]. However, due to a small sample size of the minority class used in this study, there could be cases of no observations for the minority in a test set when a large training set is employed with conventional train-test split. Therefore, this study increased the testing set size to 50% of the dataset to observe both classes in the testing set and therefore evaluate the model performance for both classes.

Imbalanced classification data leads to biased prediction toward the majority class. Several sampling techniques have been developed to address class imbalance problems such as undersampling and oversampling. Undersampling deletes examples from the majority class in the training set, but it can pass over important information during removal. Oversampling simply duplicates examples from the minority class and certain examples can be dense at a specific location in the sample space, thereby leading to overfitting due to the repetitively used samples. This study employed one of the improved oversampling methods, Synthetic Minority Over-sampling Technique (SMOTE) proposed by Chawla et al. [77],

which is the most popular and perhaps most successful oversampling technique [78], [79] that creates new synthetic data from the minority class rather than simply duplicating the data. The minority class is oversampled to have the same number of samples as the majority class. For example, Frame 2 had 7,111 times greater number of the majority class than the minority class. The new minority class examples are generated 7,111 times in a training set to equal the number of majority class examples. The oversampled minority class are not duplicates of the existing samples, but are derived using k-nearest neighbors and interpolation parameters. Many studies [80]–[83] have proven that the SMOTE approach is simple and computationally efficient while providing superior performance.

2.5 Comparison of sensitivity analysis results

This section compares the sensitivity analysis results obtained by the feature importance approach and the reliability sensitivity analysis. For the reliability-based sensitivity study, 40,000 simulations for each uncertainty under consideration were conducted. The feature name consists of the structural member name following the property name. Residual stress and sway imperfection are shortened to 'rs' and 'sway', respectively. For example, E-B2 represents the elastic modulus of B2 and rs-C1 indicates the residual stress of C1. Sway imperfections at the column locations – left, center, and right – are labeled as sway-C1, sway-C2, and sway-C3, respectively.

Table 2.3 summarizes the reliability-based sensitivity analysis results including statistics of strength, probability of failure, and reliability index. Frame 1 has larger COVs than Frame 2, with a larger difference for random elastic modulus and sway imperfection, which indicates that Frame 1 is more sensitive to these factors. Although the nominal ultimate strength was equal to 1.08 for both frames, Frame 1 has smaller values of β compared

Table 2.3: Reliability-based sensitivity results for Frames 1 and 2

	Frame 1				Frame 2			
	Strength		Reliability		Strength		Reliability	
Random variable	Mean	COV	β	P_f	Mean	COV	β	P_f
Yield strength	1.13	0.034	3.41	3.3×10^{-4}	1.16	0.031	3.79	7.5×10^{-5}
Elastic modulus	1.07	0.007	9.01	≈ 0	1.07	0.004	16.8	≈ 0
Sway imperfection	1.01	0.030	2.65	4.0×10^{-3}	1.08	0.011	3.51	2.3×10^{-4}
Residual stress	1.07	0.003	27.7	≈ 0	1.07	0.002	37.2	≈ 0

to those of Frame 2 due to the larger COVs of Frame 1 resulting in a lower boundary of the strength distributions.

2.5.1 Frame 1: instability of a single column

The results of the feature importance method are shown in Fig. 2.4. The top row (Fig. 2.4a-c) shows the top ten feature rankings of Frame 1 derived from the data analysis methods including ANOVA, mRMR, and Spearman's rank. The feature orders obtained from the model analysis techniques including impurity-based, permutation, and SHAP are shown in the bottom row (Fig. 2.4d-f). As previously discussed in Section 2.2, the feature importance techniques can derive either positive or negative values or both. As the feature rankings show only ten highly-ranked features, the negative scores are not included in the figure except for Spearman's rank (Fig. 2.4c), which rated the features based on their feature importance value magnitude. Sway-C2 and F_y-C2 are top-ranked from all the feature importance methods. Sway-C3 or E-C3 is third-ranked but has a negligible importance score in comparison to the top two features. Although the order of the remainder of the features is different between the various techniques, only the two highly-ranked features have significant scores. In other words, only the first two features are significant to the prediction of failure for Frame 1. Most methods result in scores approximately equal to zero for the least important features. Frame 1 fails by the inelastic instability of C2, and this is reflected in the importance score results as the

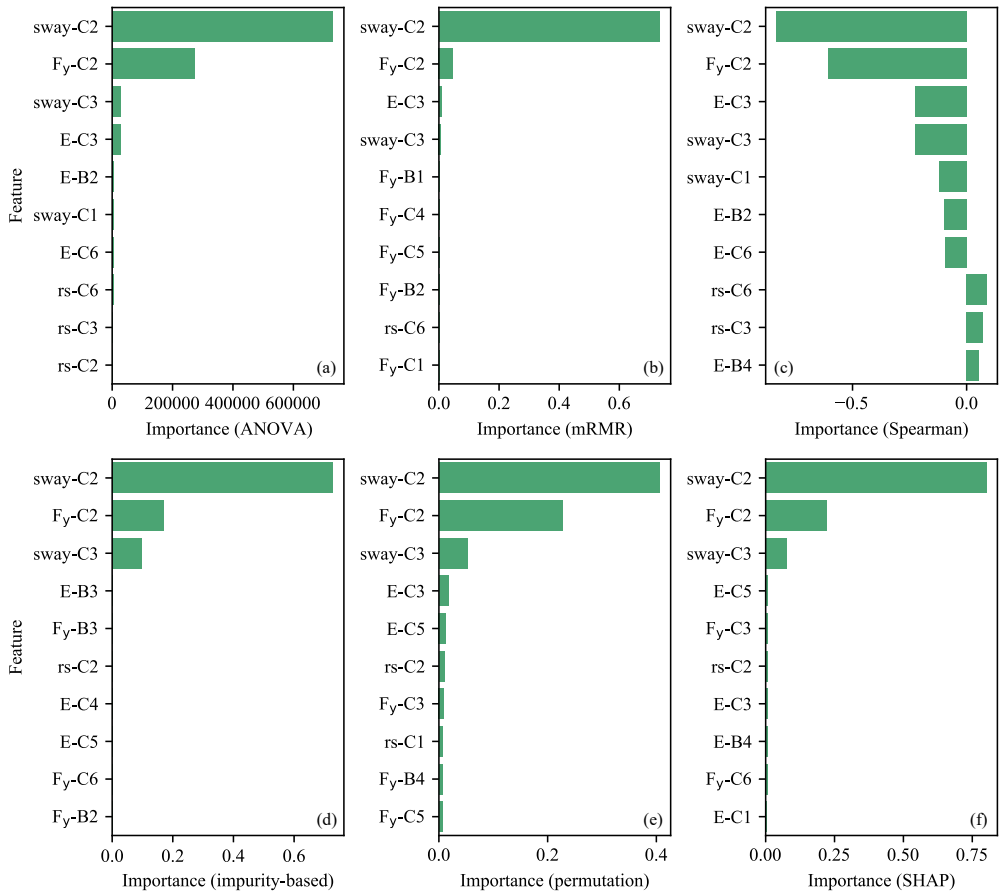

Figure 2.4: Importance ranking of the top ten features of Frame 1 derived by data analysis methods (top row) and model analysis methods (bottom row)

features related to C2 are the most highly ranked.

From the results of Table 2.3, random sway imperfection resulted in the lowest β in Frame 1, followed by yield strength, elastic modulus, and residual stress. A small elastic modulus and large sway imperfection increase lateral deflections, thereby increasing second-order bending moments. As Frame 1 fails by the instability of C2, the frame capacity is most influenced by the factors resulting in increased bending moments.

Fig. 2.5 illustrates the scatter plots of input random properties versus

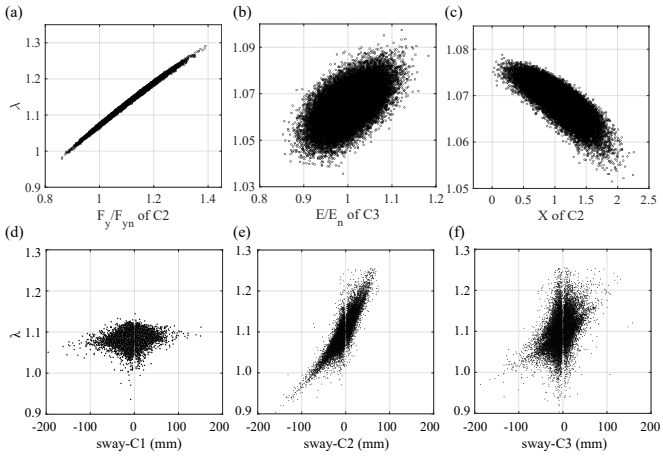

Figure 2.5: Scatter plots of Frame 1 strength versus random (a) F_y of C2 (b) E of C3 (c) X of C2 (d) sway imperfection of C1 (e) C2 (f) C3

the frame strength based on the reliability-based sensitivity studies. As shown in Fig. 2.5a, the yield strength of C2 and the frame strength have a nearly perfect correlation, which indicates that the strength of Frame 1 is controlled by C2. The yield strength of the other members showed no correlation with frame strength. Fig. 2.5b and c show that the frame strength has a weak correlation with the elastic modulus of C3 and the residual stress of C2. The sway imperfection at the center column (C2) has the most significant impact on the strength among the three column positions — left (C1), center, and right (C3) — by showing a strong positive correlation.

The highly-ranked features determined from the feature importance methods are identical with the factors that resulted in a lower β from the reliability-based sensitivity analysis. The feature rankings determined by the feature importance framework showed that sway-C2 and F_y-C2 are the most important features among the thirty-three random properties. The third-ranked feature is either sway-C3 or E-C3, which showed a positive correlation with the frame strength, but less significant than sway-C2

and F_y-C2. Overall, the random properties that have significant impacts on Frame 1's capacity determined by the reliability-based and machine learning-based sensitivity analyses are in agreement.

2.5.2 Frame 2: progressive yielding

Fig. 2.6 shows the top ten feature rankings of Frame 2 derived by the feature importance approach. As shown in Fig. 2.6a-c, the top-ranked feature is either F_y-C6 or sway-C2, and the remaining order varies for each data analysis technique, which identifies important features without model fitting. However, the model analysis techniques, which require model training to measure feature importance, derived the same top four features including sway-C2, F_y-C6, F_y-B2, and sway-C3 in descending order (Fig. 2.6d-f). The features ranked fourth through tenth are similar between the model analysis methods. At least four yield strengths are highly-ranked across all the methods, which indicates that yield strength is an influential factor in the failure of Frame 2 and the failure mode is progressive yielding. As previously shown in Fig. 2.2b, Frame 2 has six members that have critical impacts on the system failure, including four beams and two columns. In particular, B2 and C6 have two highly yielded zones each, and the yield strengths of these members are top-ranked among all the yield strengths. The feature importance results show the significant members in the system in addition to the influential properties. Due to the complex failure mode of Frame 2, the feature orders are not as straightforward as Frame 1, however the results indicate that the feature importance approach is accurate for steel frames with various failure modes.

The reliability-based sensitivity study investigated the effects of random properties on the frame strength. As shown in Fig. 2.7, the properties that have a significant effect are identical with the features that are highly ranked by the feature importance methods. Fig. 2.7a and b show dents on

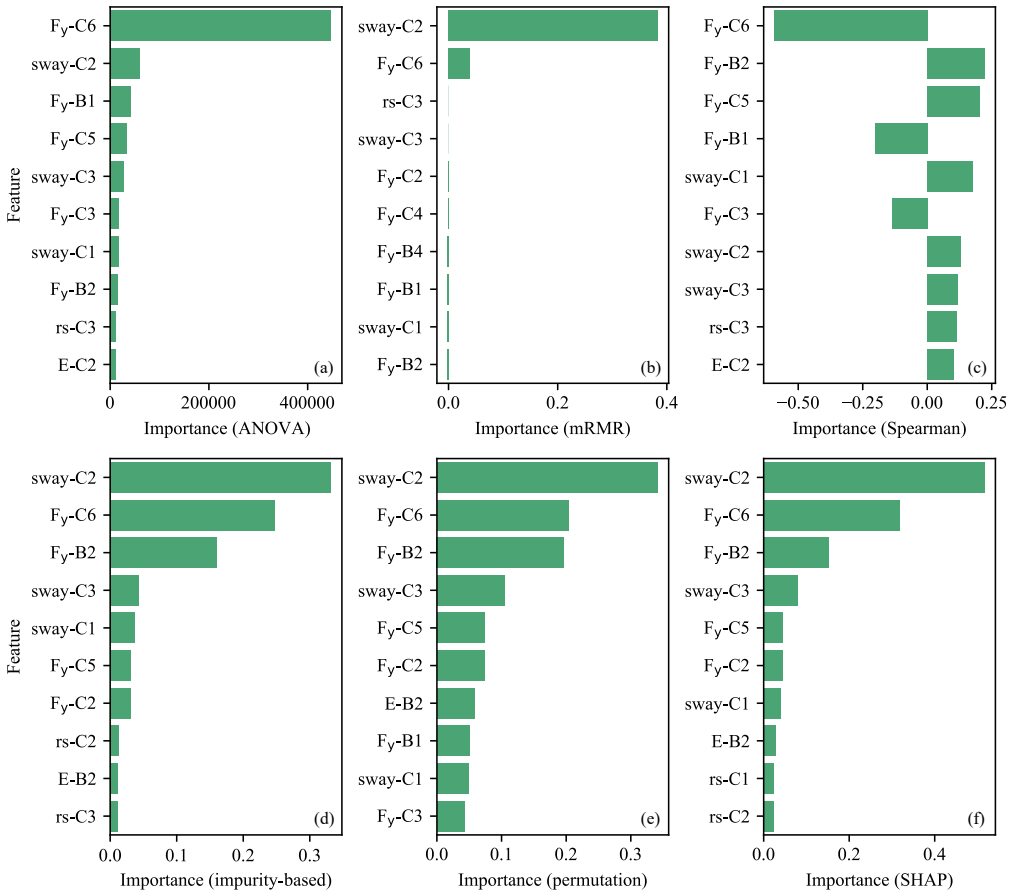

Figure 2.6: Importance ranking of the top 10 features of Frame 2 derived by data analysis methods (top row) and model analysis methods (bottom row)

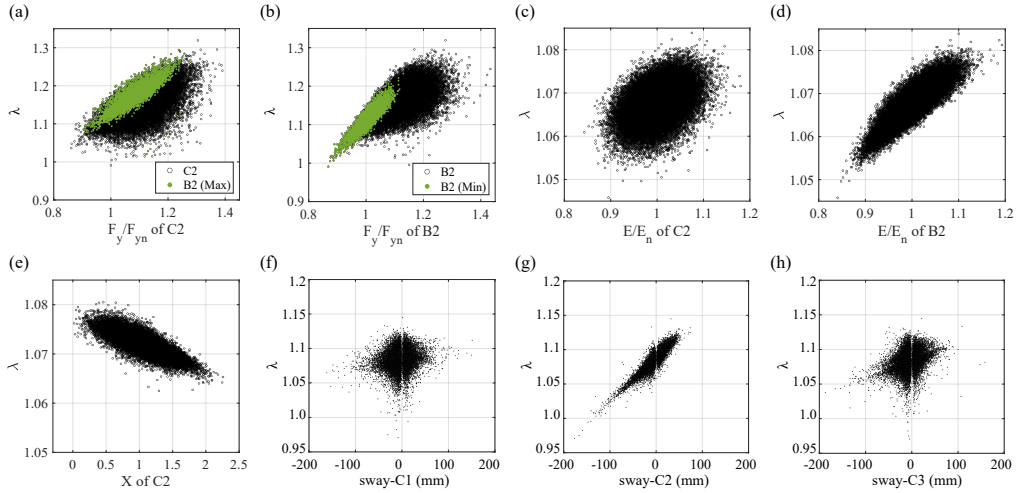

Figure 2.7: Scatter plots of Frame 2 strength versus random (a) F_y of C2 (b) F_y of B2 (c) E of C2 (d) E of B2 (e) X of C2 (f) sway imperfection of C1 (g) C2 (h) C3

the upper left side, and they occur when the value of the B2 yield strength is the maximum or the minimum among all members, respectively. Fig. 2.7c and d indicate that Frame 2's strength has positive correlations with elastic moduli of C2 and B2. As X of C2 increases, the frame strength decreases (Fig. 2.7e) because the presence of residual stresses leads to the onset of yielding at a lower applied load [62]. Random elastic modulus and residual stress of C2 and B2 are correlated with the frame strength but showed small COVs, which represents less significant influence. The effects of random sway imperfection are shown in Fig. 2.7f-h. The center columns sway have the most significant impact on the frame strength than the sway of other columns. This example illustrates that not all factors influence the system behavior, and it is therefore unnecessary to assess the effects of each factor individually, as is done in a reliability-based sensitivity analysis. On the other hand, the feature importance approach analyzes all the factors at once to estimate the effects on system behavior.

Overall, Frame 2 has smaller magnitudes of the importance scores than

for Frame 1. Moreover, Frame 1 has a large difference between the two top-ranked features and the remainder of the features, while the score difference between the features in Frame 2 is smaller. In other words, the importance score of Frame 2 decreases smoothly from the top to the bottom of the rankings. When a structural system fails by a single member (Frame 1), the properties of that member has a critical impact on the entire system. On the other hand, when various members lead to a system failure, such as progressive yielding (Frame 2), the properties of multiple members have a significant impact on the entire system. A comparison of the importance values between Frame 1 and Frame 2 indicates that the number of structural members involved in system failure influences the magnitude of importance as well as the number of features considered to be important.

2.6 Performance evaluation

The test set, which accounts for 50% of the dataset, is employed to evaluate the models fitted on the training set. The accuracy metrics include specificity and recall to measure the correct prediction of Class 0 (no failure) and Class 1 (failure), respectively. In addition, the Matthews correlation coefficient (MCC) is used, which is a suitable metric for the imbalanced dataset.

The predictive performance of the machine learning models for Frame 1 is shown in Fig. 2.8. The specificity curves for both logistic regression and decision tree algorithms (Fig. 2.8a and b) show that the specificity score reaches the nearly perfect value of approximately 1.0, even with only a few features. In this study, specificity represents the proportion of safe structures that are correctly predicted. The Frame 1 dataset is severely imbalanced with the no-information rate of 99.94%, therefore the model performance measured by specificity shows inflated results due to the

biased classification towards the majority class. Recall is computed to evaluate how good a model is at detecting a structural failure, which is the positive class. As it is critical to identify system failure rather than safe structures in structural design practice, recall is a more crucial measure than specificity in this study. Fig. 2.8c shows the recall curve obtained from the logistic regression model. When the feature set contains the top three features of the model analysis techniques and ANOVA, which are sway-C2, F_y-C2, and sway-C3, the recall score rapidly increases up to 0.77. Spearman and mRMR ranked the sway imperfection of C3 at fourth and therefore the score abruptly rises when the feature set increases to four. The recall curve of the decision tree (Fig. 2.8d) shows the highest value when only two or three features are selected. The outcome recall scores converge to a lower score of 0.72 after reaching the peak point. This indicates that bottom-ranked features could be removed to reduce the computational effort without compromising model predictive performance to improve the computational efficiency Fig. 2.8e and f show the outcome MCC scores for the logistic regression and decision tree models, respectively. The MCC curves have a similar shape as the recall curves; the logistic regression model performance improves as the feature set increases, and the decision tree model reaches the peak point when the feature set is small. This indicates an overfitting issue which occurs when the model is trained on a large feature set. Feature selection based on the feature importance score can improve the overfitting by excluding the redundant features from training. The least important features, which are ranked after the fifteenth, could be removed to obtain a better performance.

The model performance of Frame 2 measured by specificity is shown in Fig. 2.9a and b. The specificity generates overoptimistic results due to the high imbalanced ratio of 99.99%. When the yield strength of C6 is ranked as the most important feature by ANOVA or Spearman, the decision tree model shows the nearly-perfect score even though the dataset

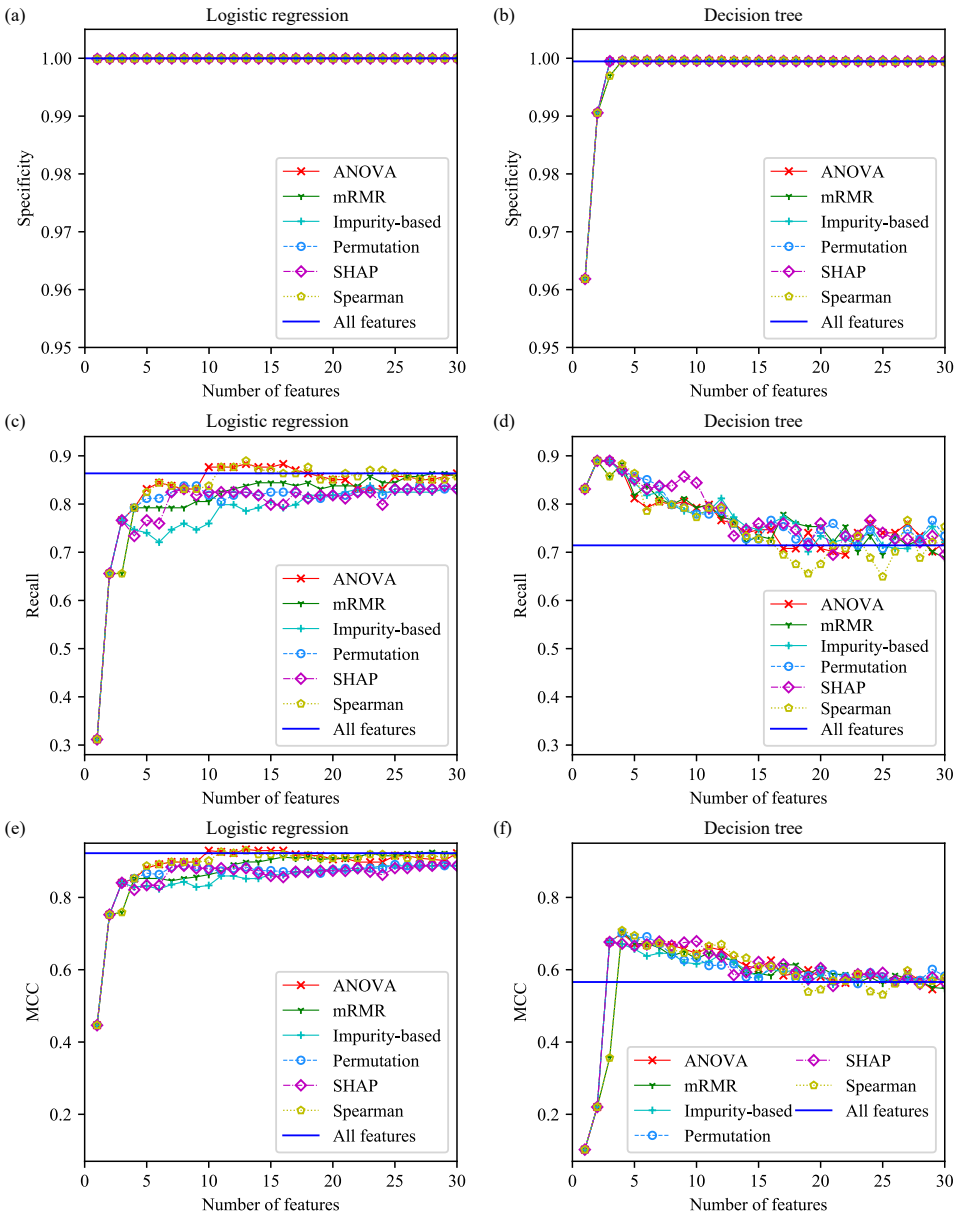

Figure 2.8: Frame 1 specificity, recall, and MCC for logistic regression (left column) and decision tree (right column)

includes only one feature (Fig. 2.9b). The lowest score of specificity is 0.92, indicating that both logistic regression and decision tree models can identify safe structures with high accuracy. The recall curves of Frame 2 are shown in Fig. 2.9c and d. The logistic regression model can correctly predict the failure only when the sway imperfection of C2 is included in the feature set. For example, the recall curve of Spearman's rank shows zeros until the feature set size is seven because the feature ranking rated the sway imperfection of C2 at seventh. The recall curve of the decision tree model (Fig. 2.9d) shows a large variation between the data analysis methods because they had completely different feature rankings. However, each curve merges to about 0.32 as the number of features increases. The MCC curve of the logistic regression model (Fig. 2.9e) shows a similar shape as the recall curve because the specificity scores had a single value, which is close to 1, regardless of the feature set size. The MCC values of the decision tree model merge to 0.15, which is the score of the entire feature set (Fig. 2.9f). When a high-dimensional dataset is used, the class imbalance leads to additional challenges in misclassification of the minority class [27]. As previously discussed in Section 2.4.3, Frame 2 consisted of a larger sample space and a fewer number of failures than for Frame 1. Moreover, the feature orders of Frame 2 were inconsistent between the feature importance techniques, as multiple features were significant to the prediction of system failure. The higher imbalanced ratio and the complex failure mode of Frame 2 result in a low performance measured by recall as well as the MCC. The extremely imbalanced classification of Frame 2 led to a lower performance for predicting structural failure because the machine learning classifiers had only a few minority class examples to oversample in the training set as well as to test the model prediction. The model performance, which measures the prediction of minority class, can be improved by obtaining more number of failures in a dataset or reducing the class imbalanced ratio.

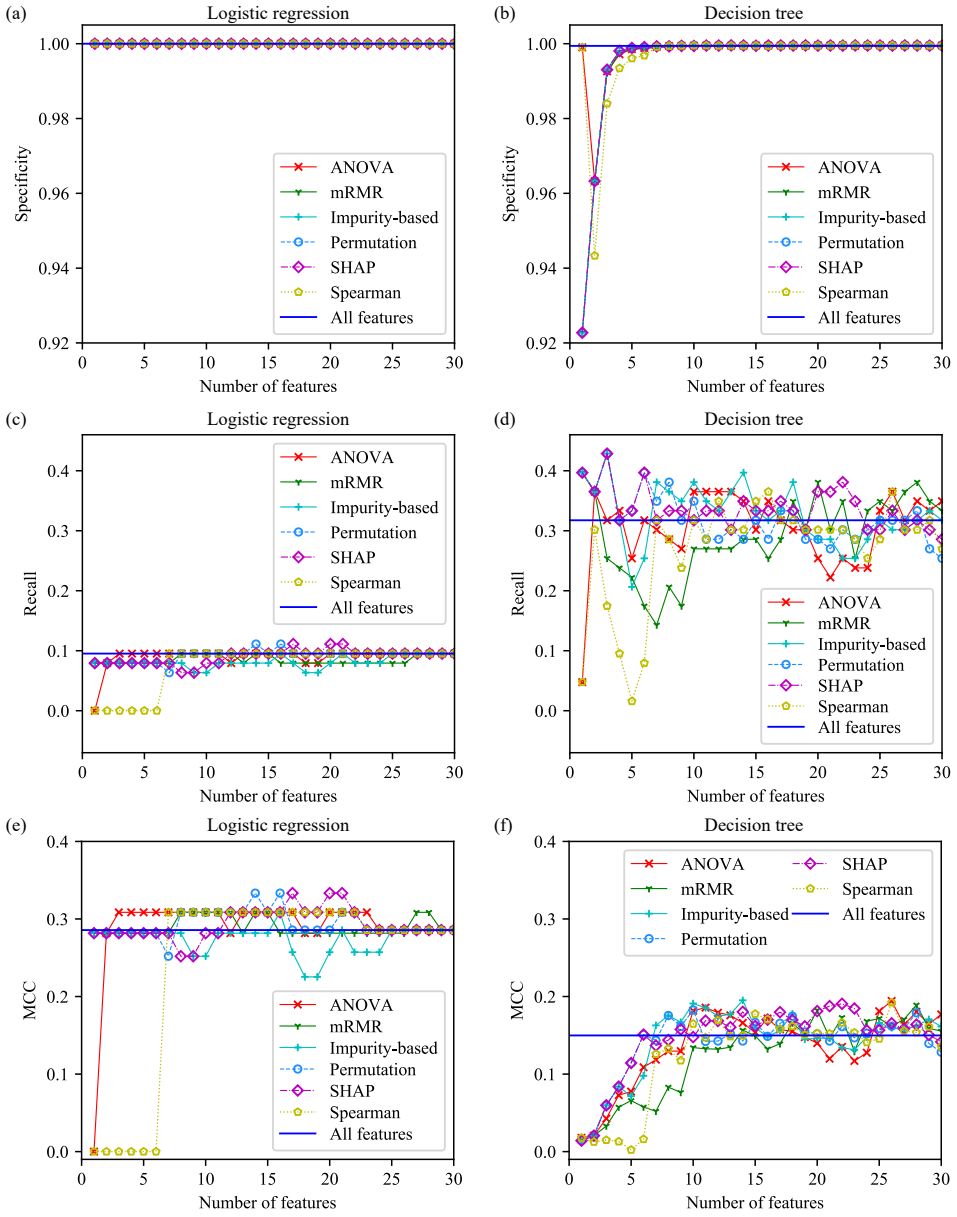

Figure 2.9: Frame 2 specificity, recall, and MCC for logistic regression (left column) and decision tree (right column)

The six feature importance techniques showed similar performance of Frame 1 measured by the MCC. The performance was improved after containing the three top-ranked features (Fig. 2.8e and f). In Frame 2, however, the model analysis methods showed more accurate results than the data analysis methods. In particular, the permutation and SHAP methods showed the best performance until the feature set size increases to seven (Fig. 2.9f) because they ranked F_y-C5 and F_y-C2 at fifth and sixth, respectively, whereas the impurity-based method ranked F_y-C2 at seventh, and F_y-C5 and F_y-C2 have a significant influence on the system failure of Frame 2. In summary, based on the feature rankings and the model performance results of both frames, SHAP and permutation methods are the best techniques for estimating the importance of features.

2.7 Conclusions

This study examined the feature importance approach using datasets with a large number of uncertainties and severely imbalanced classification. Two designs of a non-symmetric planar steel frame were investigated with uncertainties in material yield strength, Young's modulus, sway imperfection, and residual stress. The dataset information consisted of thirty-three uncorrelated uncertainties and the ultimate load ratios obtained from the finite element analyses. A scarce number of failures occurred, as is common in structural engineering design, thus the datasets were extremely class-imbalanced with the two classes being safe and fail. To observe the minority class in a test set split from the severely imbalanced data, a 50%-50% split for training and test sets were employed instead of the conventional train-test split ratio. Feature importance techniques including ANOVA, mRMR, Spearman's rank, impurity-based, permutation, and SHAP were trained on the high-dimensional and severely class-imbalanced datasets to identify the important features. The important features identified using

the machine learning based feature importance approach were compared with the results of a conventional reliability-based sensitivity study to identify factors which result in a lower system reliability index. The SHAP and permutation methods showed the best performance by ranking the same significant factors from the reliability-based sensitivity results at the top of the features. The feature importance method was not only shown to be straightforward in selecting the significant features by comparing their importance scores, but also in determining which structural members (e.g. specific columns and beams) have large impacts on structural failure without additional evaluation of performance. Overall, both methods identified the same factors which reflected the system failure modes, thus validating that machine learning techniques can be utilized in lieu of conventional reliability-based sensitivity studies.

After rating the features according to the importance score, the logistic regression and decision tree algorithms were trained to predict the classes using the feature set containing the top-ranked features. The overall performance showed that low-ranked features do not improve or even deteriorate the prediction accuracy, which indicates that they could be removed from the feature set to improve the computational efficiency. The model performance evaluated by specificity showed nearly-perfect performance for both frames because most examples were assigned to the majority class, safe structure. As for the failure prediction, Frame 1, which failed by the global buckling of a single column, showed good performance even with the highly imbalanced classification. This study determined that the machine learning-based sensitivity analysis can identify the influential features affecting system failure even when there are high-dimensional uncertain parameters and a highly imbalanced dataset, for a relatively simple failure mode. However, for Frame 2 which had a complex failure mode of progressive yielding in addition to an extremely low failure probability, it was challenging to obtain the accurate prediction

of the minority class. As class-imbalanced data is inevitable in structural engineering, it is necessary to be cautious in assessing the predictive accuracy of structures with a complex failure mode and a failure probability approximately equal to zero.

3 DATA-DRIVEN DESIGN APPROACHES FOR NORMAL AND HIGH-STRENGTH HOLLOW STRUCTURAL SECTION CAPACITIES.

Koh, Hyeyoung and Blum, Hannah B. "Data-Driven Design Approaches for Normal and High-Strength Hollow Structural Section Capacities." *Journal of Constructional Steel Research* (In preparation).

Abstract

Data analytics in structural design can provide engineers insight into identifying and analyzing behavioral data and trends that may inform the design and structural decisions. In the structural engineering industry, it is not unlikely to imagine a future industry where the design process is navigated by data-driven design tools and software that can further optimize designs based on data acquired through physical experiments and advanced technical computing systems.

This study focuses on data analytics in structural design and how it helps with incorporating new materials, such as high-strength steel, into existing design rules. To this end, a data structure for structural design is organized to accommodate structural tests with varying test variables. A large database from the literature for steel hollow section column experiments and finite element analyses was established, which accounts for a range of member slenderness, steel grades ranging from normal to high-strength, and both hot-rolled and cold-formed formation processes. Data-driven approaches using conventional interpolation and newer machine learning algorithms are adopted to predict the column buckling strength, and their time and performance are compared to justify the use

of machine learning tools. The predictive performance of the proposed model is compared with the results from the current design standards including AISC 360 and Eurocode 3. The database and all analysis methods are coded in a user-friendly computational notebook format for ease of use and saved in the open-source repository so future researchers and users can update and modify the analysis as future data is generated. In addition, practical applications in the use of data-driven approaches using the proposed data structure are provided to encourage structural designers and fabricators to get benefit from data-guided structural design.

3.1 Introduction

Big data is going to transform the civil engineering industry with the help of its vast variety of tools and techniques. In structural engineering, big data can be used for descriptive and predictive analytics. Descriptive analytics generate accessible insights from uninterpreted data, providing an understanding of relationships between parameters that affect complex structural scenarios or behaviors. Predictive analytics provide data-driven models that identify the likelihood of future outcomes, which can predict structural responses in support of physics-based models. Using data analytics, data is extracted from these databases in order to identify and analyze behavioral data and trends that may inform design and structural decisions.

The advances in computational capabilities have enabled to access comprehensive data that includes a large number of observations and parameters. Structural engineers can exploit data to make use of huge amounts of data acquired through physical experiments and advanced technical computing systems. To efficiently perform operations for tasks using the data, it is necessary to design data structures. A data structure is a storage that is used to store and organize data, and it is a way of arranging

data on a computer so that it can be accessed and updated efficiently by users. The industry has looked for help from specialists to handle a vast amount of field data for data review and mapping data, which can be time- and resource-consuming. Publicly available data structures for structural design can advance data analytics for structural engineering, which has not taken full advantage of advancements in data analytics [84].

Data-driven design approaches such as interpolation and regression have broad applications for predictive analysis using the data. However, interpolation and regression are theoretically derived from univariate prediction, therefore they become challenging when a large data is applied while maintaining tractable computational complexity [85]. Recently, machine learning (ML) techniques have shown significant advantages in estimating underlying complex relationships of parameters and could help the structural design industry benefit from the vast quantities of available data. ML has been implemented to predict responses of steel structural components [31], [32], [86]–[94], which have demonstrated the ability to improve the regression accuracy of capacity prediction of steel components. However, most of the studies listed above considered either only experimental or numerical results to predict the structural responses while both physical testing and numerical results can be used for structural analysis and design per multiple steel design codes [1], [4], [6], [7], [10].

To introduce a data structure for structural design and data-driven models using a database that includes both experimental and numerical data, this study explores the buckling capacity of square and rectangular hollow section (SHS and RHS) columns. Hollow sections are widely used as structural elements in buildings and other structures due to their structural efficiency coming from a high strength-to-weight ratio, therefore a large data from the literature is available. The predominant manufacturing processes of SHS and RHS members are hot-rolling, cold-forming, or welding four steel plates into a box shape.

Design rules for SHS and RHS members in compression are codified in structural steel design codes such as the US code (AISC 360 [1]) and the European code (Eurocode 3 [4]). Experimental and numerical results for various cross-section types and sizes with geometric imperfections were incorporated to build the buckling curves given in the codified provisions. For example, AISC 360 [1] has a single buckling curve based on the numerical results of columns with an initial out-of-straightness, which were studied by Tide [95], Bjorhovde [96], and Galambos [97]. Eurocode 3 (EC 3) [4] developed five different buckling curves built upon experimental and numerical results [98]–[102]. Although the codified provisions have been broadly used in the structural steel industry, the accuracy and efficiency of the design rules can be improved by addressing several challenges; (1) Although high-strength steel grades have been available due to the advancement of steel manufacturing technology in recent years, the design rules for them are a simple extension of those for normal-strength steels and do not directly address the influence of material yield strength. Meng and Gardner [2] proposed an SHS and RHS column design approach that reflects the influence of material yield strength by modifying the imperfection factor as a continuous function of yield strength. EC 3 [103] has codifications for steel grades up to 700 MPa for hollow sections, but AISC 360 [1] still has limited provisions for hollow sections with steel grades greater than 485 MPa. A predictive model that addresses a wide spectrum of steel grades could address this issue. (2) Formation methods are not incorporated into the design rules. Cold-formed hollow sections should follow the design rules for hot-rolled steel. Therefore, the current design provisions are unable to accurately predict the actual capacity of SHS and RHS columns particularly for high-strength steel and cold-formed steel members. The test capacity of high-strength steel columns [2], [104]–[106] predicted by EC 3 [4] or AISC 360 [1] were shown to be overly conservative [2]. Moreover, it was reported that the

AISC method even provided unconservative predictions compared with the actual results for cold-formed steel hollow section columns [2], [105], [107]–[112]. These under- and over predictions resulting from the existing design provisions indicate the necessity of an accurate prediction model for the buckling capacity of high-strength steel RHS and SHS columns fabricated by different techniques. (3) A set of design formulae is necessary to estimate the buckling resistance, and an appropriate equation should be selected depending on the factors that affect failure modes of columns, such as formation process, member and element slendernesses, and yield strength of the material. The lack of a unified design equation leads to inconsistent predictions for structural members at the boundary of failure modes [86]. Thus, it is necessary to provide a unified model that covers various geometric and material properties and forming processes which may impact the controlling failure modes.

This study focuses on data analytics in structural engineering and how it helps with incorporating new materials, such as high-strength steel, into design. The objectives of this study are: (1) Design a data structure that includes both experimental and computational data, To this end, the SHS and RHS column buckling capacity was explored in this study. The database includes a wide range of steel grades and geometric properties and both cold-forming and hot-rolling forming processes. Therefore, prediction models based upon the database can address the limitations of the current design rules for hollow section columns and therefore engage future generations of design specifications. (2) Develop data-driven models including conventional interpolation and newer machine learning algorithms. To this end, a multi-variate linear interpolation model is developed first to examine if enhanced data-driven techniques, such as extreme gradient boosting and multilayer perceptron, need to be deployed. (3) Discuss the existing design rules for SHS and RHS capacity estimation. Since the database covers a range of material and geometric

properties and formation processes, comparisons between the predictions by the proposed ML models and the current design rules can provide recommendations to improve the design provisions. (4) Provide practical application of implementing the data-driven method for steel design. Therefore, the data and models are publicly available on an open-source repository, GitHub. The open-source tools will enable future modifications as more data is obtained. The provided guidance will invite the structural designers and fabricators to data analytics so they can benefit from data-guided structural design.

In this paper, the current provisions for the design of hollow section columns are discussed. Second, an extensive database is constructed, which contains 695 experimental results and 3,794 FE analysis results of SHS and RHS columns from the literature. Columns with a wide spectrum of geometric and material properties are investigated. Third, a procedure to develop interpolation and machine learning regression models customized for the task of this study is provided. An N-dimensional linear interpolation model and two different ML algorithms including Extreme Gradient Boosting [11] and Multi-layer Perceptron were fitted to the database. Fourth, results are discussed in terms of computation time, prediction accuracy, and feature importance. Lastly, the developed ML models for SHS and RHS columns are evaluated by comparing the capacity obtained from the existing design methods provided in AISC 360 [1] and Eurocode 3 [4]. Fifth, guidance of implementing the proposed method is provided, which can engage practitioners to use it without hurdles. The predictions derived by the developed ML models showed a high accuracy with a low variance which demonstrates the potential of using machine learning to consistently estimate the strength of hollow section columns with various steel grades and forming processes.

3.2 Data-driven approaches

As samples in the database are sparsely- and unevenly-scattered, linear multivariate interpolation was implemented to predict the hollow section column buckling capacity for the unsampled locations. In addition, two ML algorithms including Extreme Gradient Boosting (XGBoost [11]) and Multi-layer Perceptron (MLP) were implemented, which have shown success in similar regression tasks for predicting the strength of steel and reinforced concrete structural members and systems [35], [36], [40], [86], [88]. The open-source libraries $scipy$ [113] and $scikit-learn$ [114] in Python 3 were used to implement the algorithms.

3.2.1 Linear multivariate interpolation

Linear interpolation is a simple mathematical method, involving the generation of new values based on an existing set of values. This method is achieved by rendering linear polynomials to construct new data points within the range of a discrete set of known data points. In this study, piecewise-linear interpolation was adopted, which finds interpolated values using triangulation of scattered data.

3.2.2 Extreme Gradient Boosting

XGBoost is a decision tree-based model, which is illustrated in Fig. 3.1a. A decision tree algorithm [115] builds regression models in the form of a tree-like structure. A decision tree algorithm starts from the root of the tree that contains the whole training set. The root node is further split into sets of internal nodes in which observations are conditionally based. A final prediction is determined by a series of decision rules for how to split the subsets from a root node to a leaf node which is not divided into further nodes. The mechanism of the XGBoost algorithm is continuously adding and training new trees to fit residual errors of the last iteration.

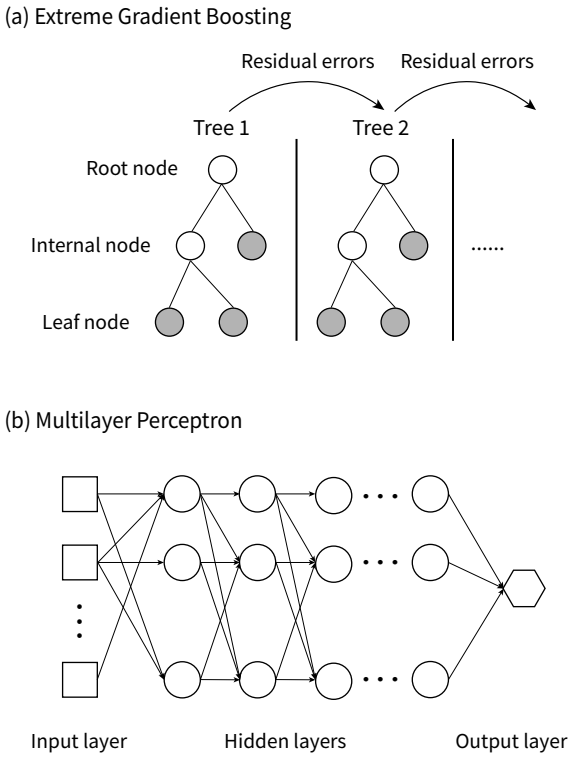

Figure 3.1: Graphical illustration of the machine learning algorithms (a) Extreme gradient boosting (b) Multilayer perceptron

In short, XGBoost builds a model consisting of multiple decision trees and implements a gradient boost training approach that improves a single weaker model by combining it with other existing weaker trees to develop a strong prediction model. Thereby, XGBoost offers more accurate and faster predictions than tree algorithms without boosting.

3.2.3 Multi-layer perceptron

An MLP consists of interconnected neurons transferring information to each other, which is much like the human brain and nerve system, to

implement function approximations. The network can be divided into three main layers including an input layer, hidden layers, and an output layer as illustrated in Fig. 3.1b. The input layer is an initial layer of a network that incorporates input variables that will be used to generate an output. The network requires at least one hidden layer which performs computations and operations on the previous layer through a function involving the weights and values in a mathematical form. The weights assigned to the connections between the layers specify the importance of neurons.

3.3 Design rules for RHS and SHS columns

3.3.1 ANSI/AISC 360-16

Chapter E of the US specification ANSI/AISC 360-16 [1] provides the design criteria for members under compression. When an SHS and RHS section has a nonslender element that has the width-to-thickness ratio, b/t, of equal or less than $1.4\sqrt{E/F_y}$, where b is width of flat regions and t is thickness (Fig. 3.2), Eq. 3.1 is used to derive the design buckling resistance $N_{u,AISC}$ of the section, where F_y is yield strength of material and E is Young's modulus. Cross sections with slender elements, which have b/t greater than $1.4\sqrt{E/F_y}$, should use Eq. 3.2 which considers an effective cross-sectional area to estimate the buckling resistance:

$$N_{u,AISC} = \phi_c \chi_{AISC} F_y A_g \text{ for SHS and RHS with nonslender elements} \tag{3.1}$$

$$N_{u,AISC} = \phi_c \chi_{AISC} F_y A_e \text{ for SHS and RHS with slender elements} \tag{3.2}$$

where ϕ_c is the resistance factor for compression, equal to 0.9 in AISC 360 [1], A_g is the gross cross-sectional area, and A_e is the effective cross-

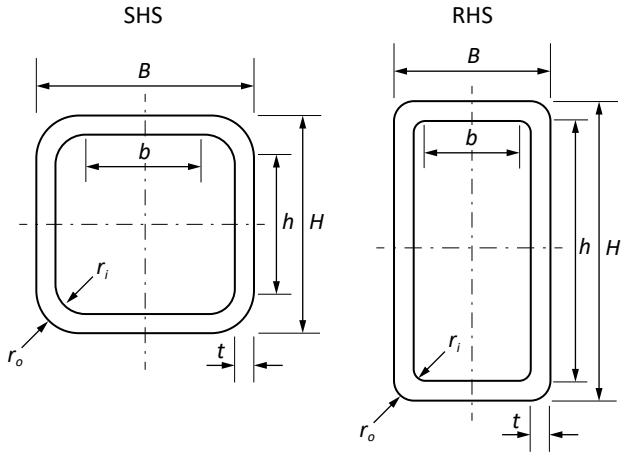

Figure 3.2: Cross section geometry for SHS and RHS

sectional area. χ_{AISC} is the AISC column buckling reduction factor, which can be calculated by either Eq. 3.3 or Eq. 3.4 depending on the member slenderness ratio L_c/r or relative slenderness ratio $\lambda_c = (L_c/\pi r)\sqrt{F_y/E}$, in which L_c is the effective member length determined by $KL = L_c$, where K is the effective length factor and L is member length, and r is radius of gyration of a cross section:

$$\chi_{AISC} = 0.658^{\frac{F_y}{F_e}} \qquad \text{for } \frac{L_c}{r} \leqslant 4.71\sqrt{\frac{E}{F_y}} \ (\text{or} \lambda_c \leqslant 1.5) \tag{3.3}$$

$$\chi_{AISC} = 0.877\frac{F_e}{F_y} \qquad \text{for } \frac{L_c}{r} > 4.71\sqrt{\frac{E}{F_y}} \ (\text{or } \lambda_c > 1.5) \tag{3.4}$$

where F_e is elastic buckling stress, which can be calculated by $(\pi^2 E)/(L_c/r)^2$.

Fig. 3.3 illustrates the χ_{AISC} value as a function of the relative slenderness λ_c. AISC 360 [1] developed the buckling curve based on columns with an initial out-of-straightness of $L_c/1500$ [95]–[97]. The buckling curve for hollow sections is applicable to all forming processes and is limited to steel grades up to a yield stress of 485 MPa (70 ksi), however,

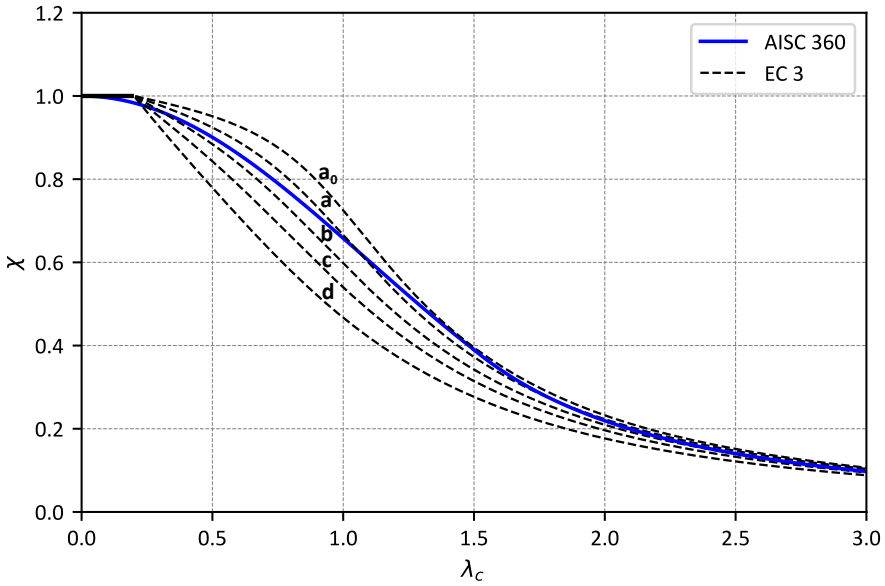

Figure 3.3: Buckling curves provided in the Eurocode 3 [4] and AISC 360 [1]

AISC 360 [1] does allow the general use of steel up to 690 MPa (100 ksi) yield stress.

3.3.2 Eurocode 3 Part 1-1

Chapter 6 of Eurocode 3 [4] provides the design provisions for column buckling. The EC 3 buckling resistance $N_{u,EC}$ can be calculated for two different ways depending on the cross-section classification. Cross sections are classified into four types based on cross-sectional element slenderness; Class 1 sections have sufficient rotation capacity to form a plastic hinge; Class 2 sections develop plastic moment resistance but have limited rotation capacity; Class 3 sections have both plastic and elastic distributions; Class 4 sections tend to have local buckling occur prior to reaching full yield stress of the cross-section. For Classes 1-3 cross-sections, which are referred to as compact sections, a gross area of section A_g is used to cal-

culate the buckling resistance as given in Eq. 3.5. Class 4 cross-sections, referred to as slender sections, utilize an effective area A_e instead as given in Eq. 3.6. The partial factor γ_{M1}, which can be regarded as a safety factor, is 1.0 in most cases as suggested in EC 3 [4].

$$N_{u,EC} = \frac{\chi_{EC} f_y A_g}{\gamma_{M1}} \qquad \text{for Classes 1-3 cross-sections} \tag{3.5}$$

$$N_{u,EC} = \frac{\chi_{EC} f_y A_e}{\gamma_{M1}} \qquad \text{for Class 4 cross-sections} \tag{3.6}$$

Fig 3.3 provides the five EC 3 buckling curves plotted against the relative slenderness λ_c. The EC 3 relative slenderness equals to $\sqrt{A_g F_y / N_{cr}}$ for Classes 1-3 cross-sections and $\sqrt{A_e F_y / N_{cr}}$ for Class 4 cross-sections. N_{cr} is the elastic critical load for the relevant buckling mode, which is $(\pi^2 EI)/L_c^2$. If the relative slenderness is equal to or less than 0.2 ($\lambda_c \leqslant 0.2$), only cross-sectional checks are required, and the buckling effects can be neglected. Each buckling curve is built upon the proper value of χ_{EC}, which can be calculated by Eq. 3.7. The buckling curves have been calibrated against experimental and numerical data for various cross sections [98]–[102] building upon the Ayrton-Perry formulation [116].

$$\chi_{EC} = \frac{1}{\Phi + \sqrt{\Phi^2 - \bar{\lambda}^2}} \leqslant 1.0 \tag{3.7}$$

The Φ factor used to calculate χ_{EC} is provided in Eq. 3.8. An imperfection factor α determines the difference in the five buckling curves, and its value varies between 0.13 and 0.76 depending on the forming process, yield strength of the material, the type of cross-section, cross-sectional height-to-width ratio, and/or flange thickness. According to EC 3 [4], hot-rolled hollow sections with steel grades between 235 MPa - 460 MPa adopt the buckling curve a where the α value is 0.21. Hot-rolled hollow sections with high-strength steel that have a nominal yield strength between 460

MPa and 700 MPa adopt the buckling curve a_o in which the α value is 0.13. Cold-formed hollow sections adopt the buckling curve c where the α value is 0.49. The height-to-width ratio is not considered to estimate the α value for hollow sections.

$$\Phi = 0.5\left[1 + \alpha(\overline{\lambda} - 0.2) + \overline{\lambda}^2\right] \tag{3.8}$$

3.4 Database

Data-driven models undergo a training procedure to recognize the patterns in data. Therefore, using reliable training data is crucial for developing an accurate data-driven model. This study established a database of steel SHS and RHS members under compression from the literature including journal papers and technical reports. A total of 695 experimental results [2], [104], [105], [107]–[110], [112], [117]–[121] and 3,974 FE results [2] were assembled. Meng and Gardner [2] developed shell FE models to simulate the buckling test results on hot-rolled and cold-formed steel SHS and RHS columns. Geometrical and material nonlinear analyses with imperfections (GMNIA) were performed in Abaqus [122]. The FE models were validated against the column test results and then utilized in parametric studies with a range of steel grades and geometries to expand the data pool for SHS and RHS column buckling. The detailed FE model description is provided in Meng and Gardner [2]. Table 3.1 lists the data grouped by key characteristics of hollow section columns such as formation process, steel grade, element slenderness, and member slenderness. The experimental, FE, and combined data show different proportions of samples when they are divided up into two groups according to each criterion. For example, hot-rolled columns have a small quota in the experimental data compared with cold-formed columns while the FE data has similar numbers of samples between hot-rolled and cold-formed steel

columns. As for member slenderness, the experimental data have limited numbers of slender columns, while the FE data supplemented the slender column data pool.

Table 3.1: Database grouped based on key characteristics of hollow section columns

Criteria		Experiment	FE	Combined
Forming	Hot-rolled	111	1993	2104
	Cold-formed	584	1981	2565
Grade	High-strength ($F_y \geqslant 460$ MPa)	351	797	1148
	Normal-strength ($F_y < 460$ MPa)	344	3177	3521
Member slenderness	Nonslender ($L_c/r \leqslant 100$)	590	3120	3710
	Slender ($L_c/r > 100$)	105	854	959
Element slenderness	Nonslender ($b/t \leqslant 1.4\sqrt{E/F_y}$)	333	2680	3013
	Slender ($b/t > 1.4\sqrt{E/F_y}$)	362	1294	1656

Eight input variables which are known to govern the buckling behavior of SHS and RHS members under axial compression were considered, including five geometric parameters, two material properties, and formation process. The geometric parameters include four cross-section dimensional properties, such as the overall width B, overall height H, outer corner radius r_o, and thickness t (Fig. 3.2), and the effective length L_c. Cross section-related properties required to calculate the column buckling capacity, such as radius of gyration r, cross-sectional area A, and inner corner radius r_i, were not considered for input parameters because they can be derived indirectly based on the four cross-section dimensional parameters. For stub columns that are fixed at both ends, the effective length factor K was taken as 0.5. Two material properties include yield strength F_y and Young's modulus E. The yield stress of cold-formed steel involves corner strength enhancements that emerge as a result of cold work during production, and appear in cold-formed steel tube sections [123], [124]. This study used the weighted average yield stress given in Eq. 3.9 to estimate the yield stress of cold-formed steel members incorporating the corner strength enhancements:

$$F_y = CF_{yc} + (1 - C)F_{yt} \tag{3.9}$$

where F_{yc} is the yield stress of the corner region, F_{yf} is the yield stress of the flat region, and C is the ratio of total corner cross-sectional area to total cross-sectional area of full section for compression members. Lastly, the forming process was taken into account as an input parameter to develop a consistent prediction model regardless of the manufacturing techniques.

Fig. 3.4 provides the distribution of the input and output variables grouped by the data source, which are the experimental and FE data, respectively. The histograms include statistical information such as the minimum and maximum values, mean, and coefficient of variation (CV). Histograms with a large CV enable data-driven models to fit a wide range

of the variables and hence a larger CV is desirable. Comparing the distributions for the experimental and FE data, it can be seen that overall the FE data has a larger density than the experimental data due to its comparatively larger sample size. For some variables that have a significant effect on the buckling capacity as previously discussed in Section 3.3, the FE data supplements sparse regions of the experimental data. For example, the experimental results focus on yield strength of less than 600 MPa, while the FE data augments the limited samples for high-strength steel columns. Moreover, concerning outer corner radius r_o, thickness t, and the member effective length L_c, the FE data considers larger CVs and adds samples to the database where the experimental data is limited. Distributions for the input features H and B in the FE data are discrete because the FE simulations [2] employed only two values for H and B. Variations for E in the experimental and FE data show minimal CV, which is consistent with the literature [72], [73].

Correlation relationships between the input variables and the output variable (N_u) were explored. The correlation coefficient ρ provided in Eq. 4.20 was utilized to measure a linear correlation:

$$\rho = \frac{cov(X_1, X_2)}{\sigma_{X_1}\sigma_{X_2}} \tag{3.10}$$

where cov is the covariance, σ_{X_1} and σ_{X_2} is the standard deviation of input variables X_1 and X_2, respectively. The coefficient ρ has a range from -1 as the perfect negative correlation to 1 as the perfect positive correlation. When a pair of features have a coefficient close to 1 or -1, the features have strong relationship. A coefficient of 0 indicates that the two variables are uncorrelated.

Fig. 3.5 shows the correlation matrix of the variables. The matrix for the experimental data (Fig. 3.5a) indicates that the response variable N_u is highly correlated only with cross-section thickness with a coefficient value of $\rho = 0.67$. The other input parameters have correlation coefficients

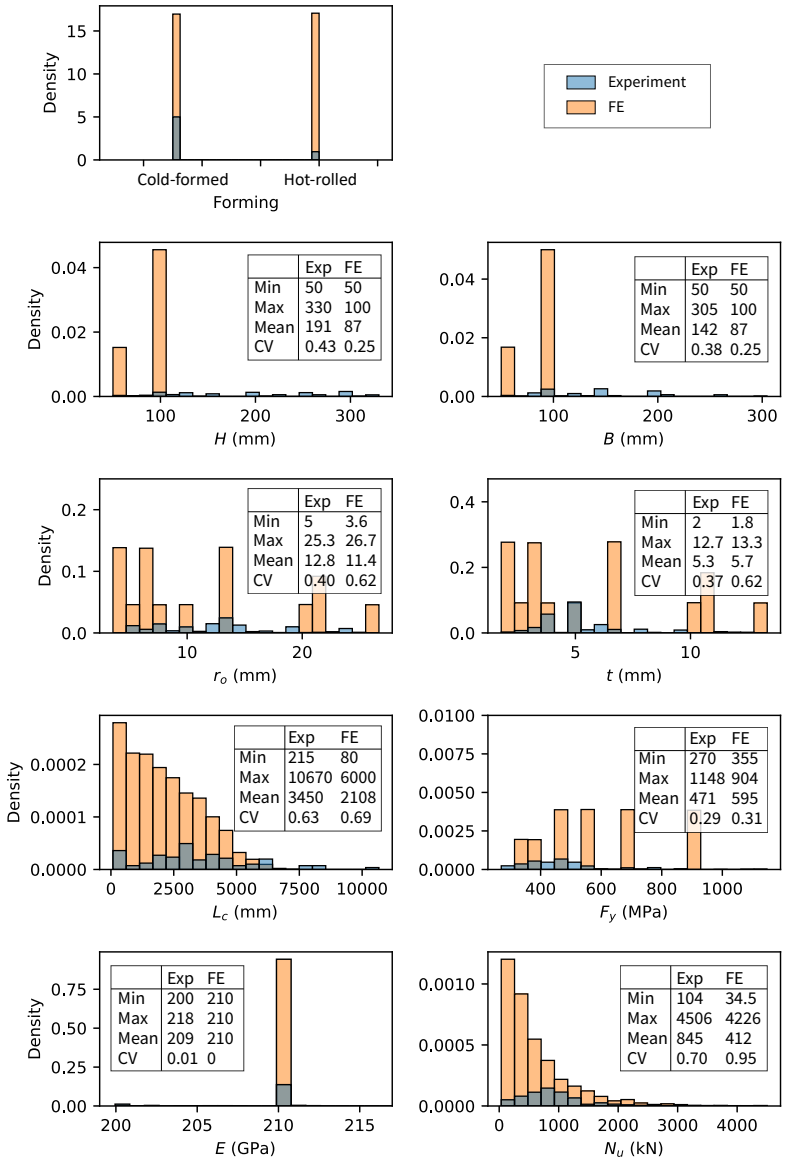

Figure 3.4: Statistical distributions of the input and output variables

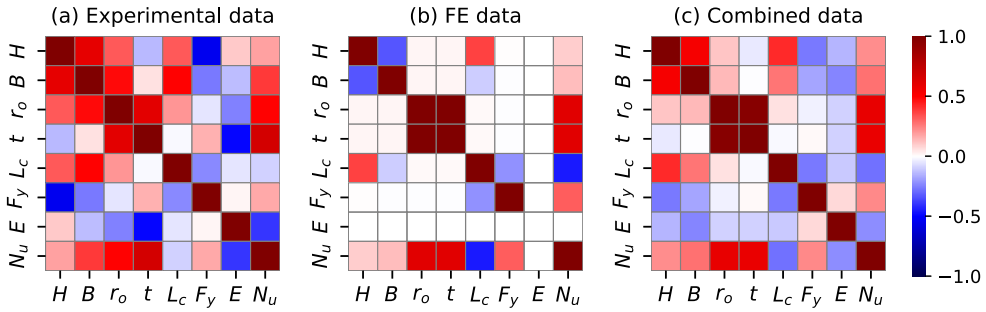

Figure 3.5: Correlation matrix of the input parameters (a) experimental data (b) FE data (c) combined data

lower than 0.5 with the output variable. The buckling capacity N_u in the FE data (Fig. 3.5b) shows a strong relationship with r_o and t with the same coefficient value of $\rho = 0.61$. It should be noted that those two input features are perfectly correlated with each other according to the FE simulation setup [2]. Since a single value of Young's modulus of 210 GPa was utilized in the FE analysis, E in the FE dataset has no relationship with any other variables. The combined data (Fig. 3.5c) more closely resembles the correlation coefficients for the FE data than the experimental data, which reflects the relatively larger size of the FE data set.

3.5 Model development

The models were trained on a set of different sizes of the data, which ranges from 10% to 90% of the data, and tested on the remaining data where the training and test sets were randomly split. Identical training and testing sets were used for the interpolation and ML algorithms for consistency. A multivariate interpolation model was created in the form of $N_u = f(H, B, r_o, t, L_c, F_y, E)$, where the seven input variables were used to approximate the buckling capacity, N_u. The parameters required by

XGBoost and MLP were determined by hyperparameter tuning based on a grid search algorithm with 10-fold cross-validation, which is a technique to search through the best parameter values from a given set of the grid of parameters. It runs through all the different parameters that are fed into the parameter grid and produces the best combination of parameters, based on a scoring metric such as a coefficient of determination. The algorithm evaluates the model performance for each combination to obtain the optimal combination of values from this set. The cross-validation process was performed to reduce errors arising from a random sampling of a training set. During cross-validation, the training set was split into k subsets (folds) and then $k-1$ subsets were used for model fitting and the remaining subset was used for model validation. A test set was held out for a final evaluation. The model performance from k-fold cross-validation takes an averaged accuracy over k folds, and this study divided the training set into ten folds.

The hyperparameter set for XGBoost algorithm determined by the grid search algorithm for this study is as follows: the sub-sample ratio of features when constructing each tree was set to 0.5; the maximum depth of a tree was set to 8; the minimum sum of instance weight was set to 5; the learning rate was set to 0.3; the regularization parameter gamma was set to 0.1. In addition, this study limited overfitting by conducting early stopping when there was no improvement observed during the XGBoost model training. Overfitting refers to a modeling error that occurs when a model is too exactly fit to a training set, thus the model may not perform well with new data. Early stopping works by monitoring the model performance on a test set and stopping the training procedure once the performance on the test set has not improved after a fixed number of training iterations.

The parameters for the MLP algorithm determined by the hyperparameter optimization are as follows: the size of hidden layers was set to (100, 150, 50) in which the first, second, and third hidden layers have 100, 150,

and 50 units, respectively; the activation function for the hidden layer was set to the rectified linear activation function 'ReLU'; the solver for weight optimization was set to 'lbfgs' which uses a limited amount of computer memory; the regularization parameter alpha was set to 0.00005; and the learning rate was set to 'constant' which adopts a constant learning rate with a step size of 0.001; the maximum number of iterations was set to 1000.

3.6 Data-driven prediction results

After developing the three data-driven models, the test set was utilized to assess the model performance. The predictive performance was evaluated by estimating the evaluation metrics including the coefficient of determination (R^2) and root mean square error (RMSE), which can be calculated by Eq. 3.11 and Eq. 3.12, respectively:

$$R^2 = 1 - \frac{\sum_1^m (y_i - y_{pi})^2}{\sum_1^m \left(y_i - \frac{1}{m}\sum_1^m y_i\right)^2} \tag{3.11}$$

$$\text{RMSE} = \sqrt{\frac{1}{m}\sum_{m=1}^{m} (y_i - y_{pi})^2} \tag{3.12}$$

where m is the total number of test data, y_i is the test value, and y_{pi} is the predicted capacity by the prediction models. The R^2 value represents how well the proposed function can predict the experimental data. The RMSE score quantifies how spread out the prediction errors are, i.e., how concentrated the data is around the line of best fit.

3.6.1 Computation time and accuracy

Interpolation, XGBoost, and MLP models were developed using a subset of data and tested based on the rest of the data. Fig. 3.6a compares

computation time executed for developing the data-driven models. The interpolation model requires the process of tessellating triangles in the data, time for triangulation is additionally shown. Comparing the model development time between the three models, the XGBoost model apparently outperforms the other models as the training set size increases. As the data size increases, the complexity of data become exacerbated. Interpolation has a considerable theoretical foundation in one dimension [125]. and it is challenging to implement interpolation when the data size is large while maintaining tractable computational complexity [85]. Therefore, time for the triangulation process largely increases as the training set size increases. Although the MLP model demands a higher computational time than the interpolation model with regards to model development, the interpolation model ultimately needs a larger computation cost due to triangulation in a data. When 90$ of data was used for model development, the interpolation model demands 16 times the computation times for MLP and 6430 times more than for XGBoost.

Fig. 3.6b compares the train and test accuracy estimated based on the R^2 score. The data-driven models have a higher curve for the training set than the test set because model tests were accomplished using the unseen data. Comparing the test performances of the models, the MLP model outperforms the other models with the highest accuracy of 0.983 at 0.8 of the training set. The XGBoost model shows higher accuracy when the training set is equal or greater than 0.4. Considering the XGBoost model showed the fastest training time in Fig. 3.6a, it is more efficient than the interpolation model in terms of computational cost and accuracy. The interpolation model shows the highest test accuracy only when the training set is 0.1. However, the model was developed based on a small sample size, thus the model can be applied on a limited range of parameters. The case of 0.1 is inappropriate to decide as a final model because multiple sample sets in the test set were shown to be out of range. According to

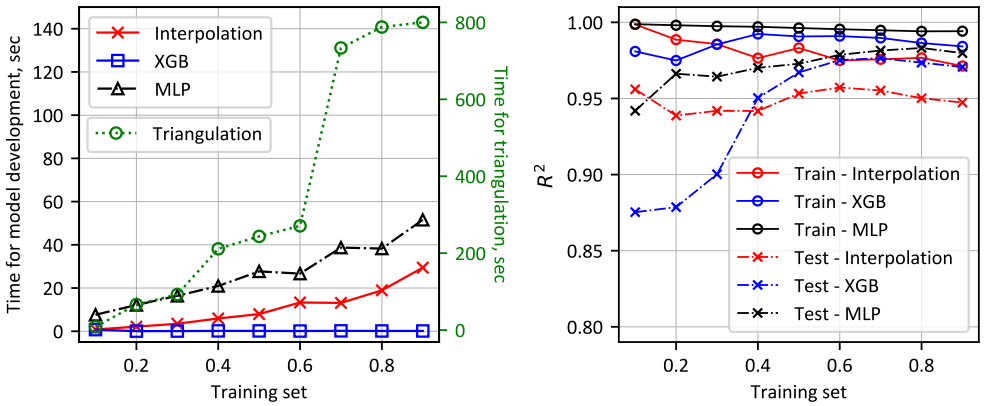

Figure 3.6: Performance comparison of the data-driven models developed based on the experimental data (a) Computation time (b) computation accuracy

the comparisons of time and accuracy, it is expected that the interpolation model could lead to inefficient predictive performance. As structural design problems often carry large data, the comparison of computation efficiency and accuracy poses the necessity of implementing enhanced data-driven approaches, such as machine learning,

3.6.2 Predictive performance

After demonstrating the benefits of ML models to computational performance, the XGBoost and MLP models were developed using the entire database that includes both experimental and FE data. Fig. 3.7 visualizes comparisons of the buckling capacity predicted by the developed models and the actual capacity measured by experiments or FE analyses in the test set. The coefficients of determination (R^2) are provided separately to assess the performance of the experimental data and FE data. The R^2 value equal to 1.0 represents the perfect prediction. Since the experimental data has a limited sample size compared with the FE data, it showed a lower performance. Comparing the performance of the developed data-

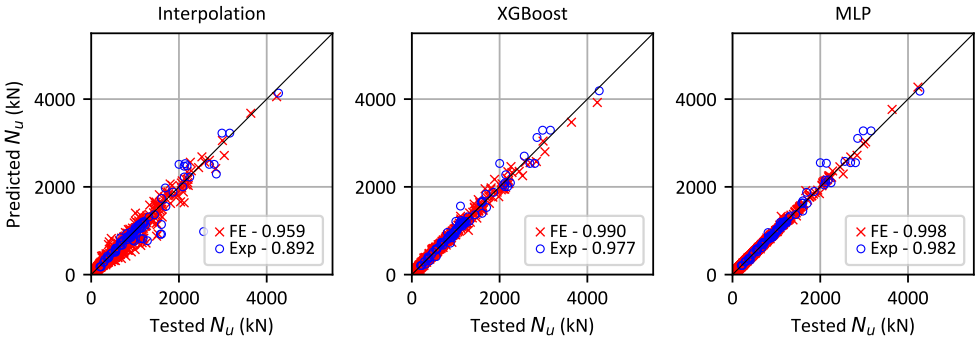

Figure 3.7: Comparison of the predicted and actual N_u of hollow section columns

driven models, the MLP model produced the best performance by showing higher R^2 scores, which are 0.998 and 0.982 for the FE and experimental data, respectively. The maximum performance difference in R^2 between the two ML models is minimal, which is 0.008 for the FE data and 0.005 for the experimental data. The interpolation model showed the lowest accuracy with scores of 0.959 and 0.892 for FE data and experimental data, respectively. The XGBoost model with the experimental data showed the poor performance between the two machine learning models, it is improved when compared with the previous machine learning studies for predicting structural responses using experimental data [36], [126], [127], in which the R^2 values ranged between 0.66 and 0.96. This indicates that the developed models are within an acceptable level of accuracy, and the models can be used for both data sources (experimental and FE) separately or combined. The high performance in the test data demonstrates the generalization ability of the models, which refers to how well a model can predict unseen data.

Prior to finalizing the ML models, they were further inspected with regard to overfitting by performing a 10-fold cross-validation on the training set. Fig. 3.8 presents box plots that provide the cross-validation accuracy of

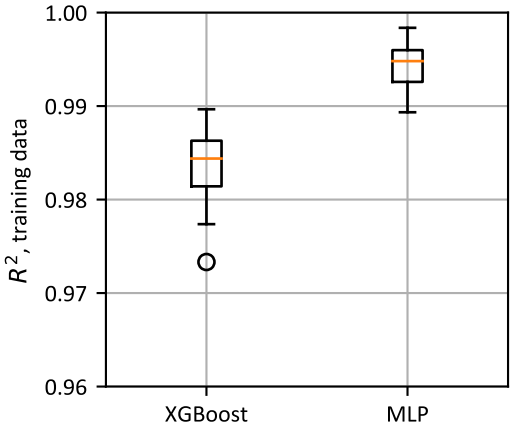

Figure 3.8: Cross-validation accuracy

the tho ML models trained with the combined data. Each box indicates the interquartile range (IQR) with the median value as an orange horizontal line in the center of the box. The maximum and minimum scores, which are defined as the value greater than 1.5 $\times$ IQR above the third quartile and the value less than 1.5 $\times$ IQR below the first quartile, respectively, are represented as horizontal bars outside the box. If outliers exist that exceed the range of the maximum and minimum accuracy, they are presented as circles. The MLP model showed a better cross-validation accuracy than the XGBoost model with a smaller variance of accuracy across the 10-folds. The median accuracies of the two models are 0.985 and 0.995, for the XGBoost and MLP models, respectively, which are equal to or slightly higher than the test set accuracy of the corresponding models. This confirms that the models have no overfitting problems, therefore they are sufficiently robust and have generalization capability to predict the buckling capacity of SHS and RHS columns.

3.6.3 Feature importance

In addition to the well-established predictive performance of the models, feature importance was measured to determine the most important factors as well as the redundant factors for SHS and RHS column capacity estimation. The feature importance method increases model explainability, which discovers meaning between input data and model outputs, and interpretability, which discovers causal relationships between input data and model outputs. Furthermore, the feature importance results can also be benchmarked against the mechanics-based principles [8]. Moreover, this process helps to improve computational efficiency without compromising prediction accuracy by excluding the least important features from model fitting. In this study, the permutation method is used to measure feature importance, which was found to be accurate and fast in identifying important features affecting steel frame behaviors [128].

The permutation approach performs repeated permutations to estimate feature importance. This approach starts with training a model to obtain a baseline model performance. After fitting the model, the samples in a single feature group are randomly shuffled, then the model performance is reevaluated. The importance J is the difference between the model accuracy obtained from the models using the original dataset, which is the baseline performance, and the dataset with permuted feature values of X_i. The importance score can be calculated by Eq. 3.13:

$$\begin{aligned} J(X_i) = &\text{ accuracy for dataset without permutation} \\ &- \text{accuracy for permuted dataset of } X_i \end{aligned} \tag{3.13}$$

If an important feature needed for prediction is absent when those values of the feature are permuted, there will be a large decrease in model accuracy. Likewise, when an unimportant feature is absent during permu-

tation, there will be minimal or no decrease in model accuracy. This study repeated shuffling ten times for a feature X_i and used the average of $J(X_i)$ as the importance of each feature.

Feature rankings were obtained based upon the importance score estimated by the permutation method. The ML models were trained and tested on a feature set that includes the top-i features, where i is the number of important features. Fig. 3.9 provides the R^2 performance curve depending on the number of features in a feature set, where the labels of data points represent the feature ranking results. For example, the performance of the third point from the left represents the R^2 score of the model that considers only the top three ranked features in a dataset. Overall, the model performance converges after a feature set includes the top-ranked six features. This indicates that the features ranked lower than sixth could be removed to improve computational efficiency. According to the curve, the XGBoost and MLP models derived different feature orders but both have the effective length L_c and thickness t as significant parameters. Yield stress F_y is fifth-ranked by both models. The forming process and E are the least significant in predicting the buckling capacity of SHS and RHS columns. This is because only two values for the forming process (hot-rolling and cold-forming) were considered in the data and only a single value of E. Thus these variables provided limited information to incorporate in the model fitting.

3.7 Discussion on the current design rules

This section assesses the proposed ML model by comparing the results to two codified column buckling design codes, the US code, AISC 360 [1], and the European code, Eurocode 3 [4]. The existing design rules apply appropriate design equations based on the slenderness of elements and/or members, steel grade, and formation process. In addition, AISC

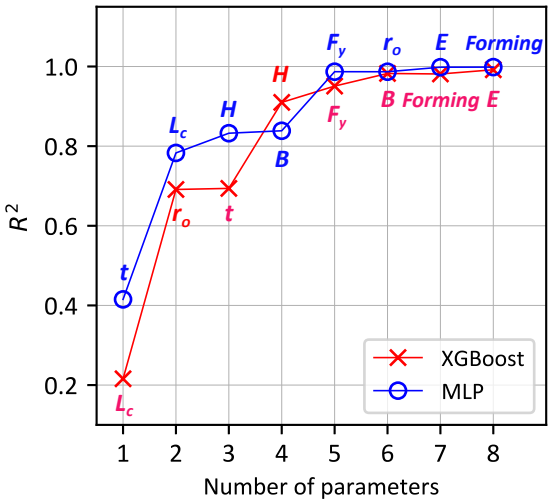

Figure 3.9: Performance curves for different ML models

360 [1] limits the applicability of the design rules to hollow sections with nominal yield strength only up to 485 MPa while EC 3 [4] allows steel grades up to 700 MPa. However, the proposed ML method considers a wide range of yield strengths and geometric properties as well as columns manufactured either by cold-forming or hot-rolling, thereby providing a consistent method for estimating the buckling capacity of various tubular section columns.

Fig. 3.10 compares the prediction-to-test capacity ratios ($N_{u,pred}/N_{u,test}$) derived by the proposed ML model and the current design provisions over the range of the relative slenderness ratio λ_c. In addition, RMSE, introduced in Section 3.6, for the combined data was measured for the range of λ_c with increments of 0.3. The predicted capacity of the existing design rules was estimated by using the equations that were previously introduced in Section 3.3. The MLP model was selected for the ML prediction because it showed better performance compared with the XGBoost model. Fig. 3.10a and b present the comparisons of the data split into two

categories, normal-strength steel and high-strength steel. Both comparisons show that the existing design rules led to a relatively large scatter band over the entire range of λ_c while the ML results derived a better prediction with a narrow scatter band. The AISC and EC design provision produce large errors for a member in the relative slenderness range between 0.6 and 1.5, which represents the inelastic buckling range where the effects of residual stresses and geometric imperfections are significant. The RMSE plot for high-strength steel predictions (Fig. 3.10b) again shows that the ML model produces the best accuracy over the entire range of λ_c. It was observed that the AISC model produces more data with lower values of $(N_{u,pred}/N_{u,test})$ than for normal-strength steel. This is because AISC 360 [1] applies a single buckling curve which does not capture the influence of the yield strength in the estimation [2]. The proposed ML model demonstrates a high accuracy for both normal- and high-strength steel column predictions.

Fig. 3.11 compares the predictions generated by the current design provisions and the proposed ML model by dividing the samples into two groups based on the formation techniques, which are hot-rolled and cold-formed. As shown in Fig. 3.11a for the hot-rolled steel predictions, the ML model presents the best performance by providing a small variance and a low RMSE score, followed by the EC and AISC models. The AISC and EC predictions for hot-rolled steel predominantly appear on the conservative side where $N_{u,pred}/N_{u,test} < 1.0$, and the AISC predictions resulted in a relatively wide scatter band and thereby a larger error (RSME) than for the EC predictions. For the cold-formed steel results (Fig. 3.11b), a large number of the AISC predictions occurred in the unconservative zone, where the capacity ratio is greater than 1.0. The EC data points show an increased level of scatter but are still present on the conservative side where the capacity ratio is less than 1.0. AISC 360 [1] does not reflect the different buckling capacities between formation techniques, whereas Eurocode 3 [4]

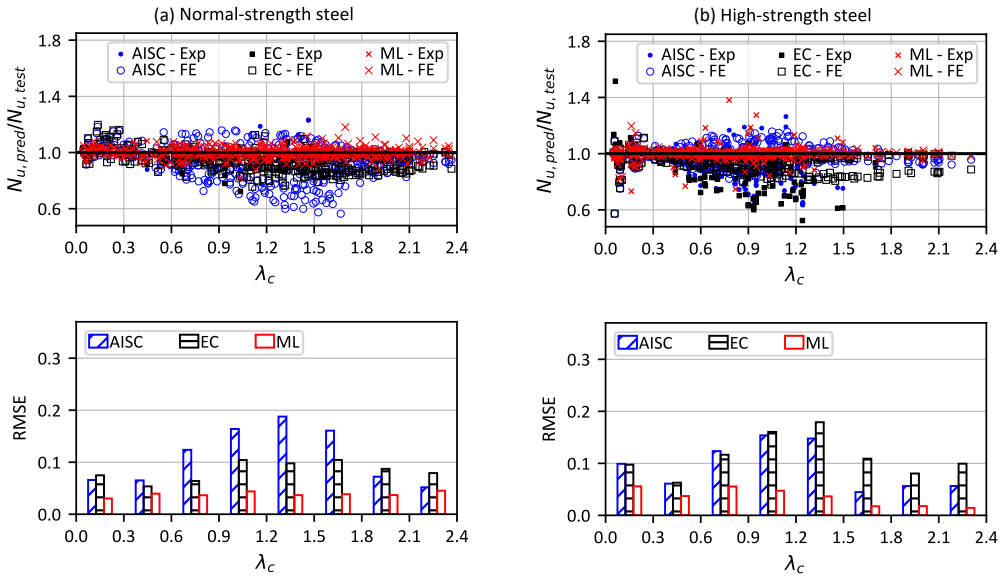

Figure 3.10: Comparisons of predictions by AISC 360 [1], Eurocode 3 [4], and the proposed machine learning model (a) normal-strength steel (b) high-strength steel

applies a different imperfection factor α to estimate the strength depending on the formation process as discussed in Section 3.3. A larger imperfection factor is applied to cold-formed steel than for hot-rolled steel, therefore the EC design provisions shows more conservative predictions for cold-formed steel than for hot-rolled steel. The provided comparisons between the proposed ML model and the current design methods in this section demonstrate the consistency and good performance of the proposed ML model for predicting both hot-rolled and cold-formed column capacities over the range of the relative slenderness ratio λ_c.

3.8 Conclusion

This paper presented data-driven models for buckling capacity prediction of square and rectangular hollow section (SHS and RHS) members under

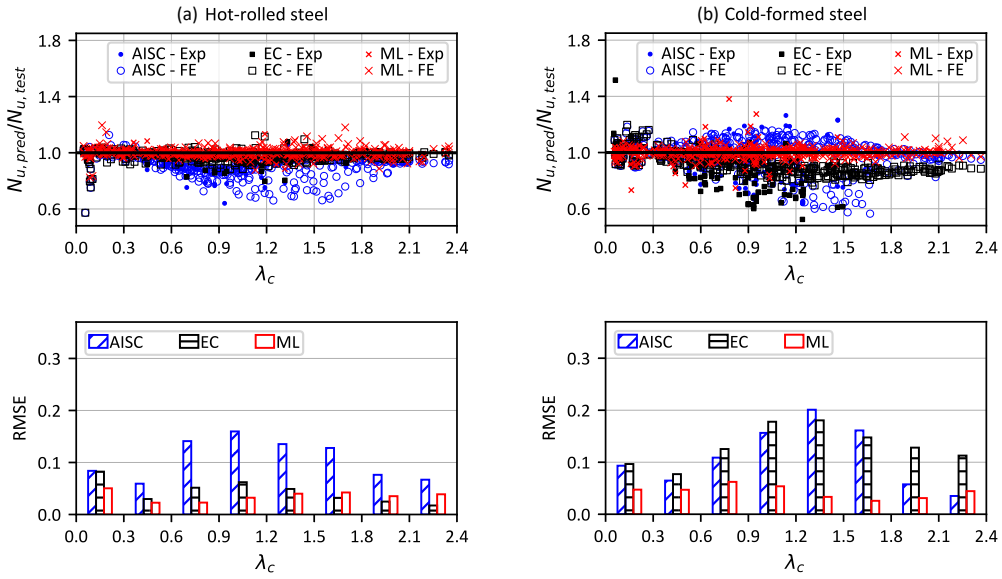

Figure 3.11: Comparisons of predictions by AISC 360 [1], Eurocode 3 [4], and the proposed machine learning model (a) hot-rolled steel (b) cold-formed steel

compression, which are manufactured by cold-forming or hot-rolling and made of high-strength or normal-strength steel. A linear interpolation and two machine learning models including extreme gradient boosting (XGBoost) and multilayer perceptron (MLP) were developed on a database of 695 experimental results and 3,794 finite element (FE) analysis results of SHS and RHS columns. The columns in the database covered a wide range of material and geometric properties such as steel grades, cross-sectional dimensions, and member slenderness. Triangulation was performed to create mesh from the dataset for interpolation model development. The machine learning models were optimized by performing feature scaling, hyperparameter tuning, cross-validation, and feature importance. The three developed data-driven models were evaluated by computation time and accuracy. The best model was further verified by the comparisons with the existing design rules for columns provided in the US code (AISC

360) and the European code (Eurocode 3). The significant findings of this research are summarized in the following:

- The MLP model obtained the best accuracy among the three investigated data-driven dmoels when evaluating the predictive performance using the coefficient of determination R^2. The R^2 score of the test set for the combined data, which includes both experimental and FE samples, was 0.983. The interpolation and XGBoost models also provided good performance with slightly lower R^2 values compared with the MLP model, which was 0.955 and 0.976, respectively.

- The developed data-driven models were separately evaluated based on the data groups: (1) experimental data only, (2) FE data only, and (3) combined data. The performance on the FE data was the highest while the experimental data led to the poorest performance due to the relatively limited sample size of the physical test results in the training set. The lowest accuracy occurred in the interpolation model when it was assessed with the experimental data only, with the R^2 score of 0.892, which demonstrates the necessity of complex method such as machine learning to improve the predictive performance.

- A 10-fold cross-validation was carried out in the training process before finalizing the ML models. The median accuracy of the ten folds was equal to or slightly higher than the accuracy on the test set. The validation results demonstrated that the models have no overfitting problems and have generalization abilities. Therefore, the models have been shown to be sufficiently robust to estimate the buckling capacity of SHS and RHS members under axial compression.

- Feature importance was measured for the input parameters to determine their significance on the buckling capacity prediction by the XGBoost and MLP models. The permutation approach was performed to estimate the feature importance. Although the order of

the important features varied between the models, member length and thickness were shown to be most significant, followed by other cross-sectional geometric parameters and material yield strength. In addition, the ML models were trained on a feature set that includes the top-i features only, where i is the number of important features, and the predictive performance of each model with the feature set was evaluated. The performance converged when the top six highly-ranked features were included in the feature set. This indicated that the least important features could be excluded from the model fitting to improve computational efficiency.

- The developed MLP model, which showed the best performance among the three data-driven models, was further evaluated by comparing to the predictions obtained from the existing design rules for SHS and RHS columns. The ratios of predicted-to-tested capacity derived from the three prediction models, which include the US code (AISC 360), the European code (Eurocode 3), and the proposed MLP model, were compared. The comparisons were separately implemented on (1) normal- and high-strength steel columns and (2) hot-rolled and cold-formed columns. The MLP model demonstrated a consistent performance, which provided the capacity ratio close to 1.0 with a small variance, over the entire range of the member slenderness ratio and across different steel grades and forming techniques, whereas the existing design methods showed inconsistent performance with relatively large root mean squared errors and variance.

The consistency and high performance of the proposed ML model indicates that machine learning based design can be a viable method for the accurate prediction of SHS and RHS column capacity. This could augment or potentially replace design provisions which have limited scope including lack of high strength steel or specifics on manufacturing process.

4 STABILITY ANALYSIS OF ROTARY-STRAIGHTENED W-SHAPE MEMBERS WITH VARIOUS STIFFNESS REDUCTION MODELS

Koh, Hyeyoung, Rosson, Barry T., and Blum, Hannah B. "Stability analysis of rotary straightened W-shape members with various stiffness reduction models." *Journal of Constructional Steel Research* (In preparation).

Abstract

Rotary straightened wide-flange cross-sections have a different residual stress distribution compared to conventional hot-rolled steel members. The assumed residual stress pattern has a strong influence on structural behavior, especially in members subjected to inelastic buckling. Previous research has indicated that the current stiffness reduction factor specified in Chapter C of AISC 360 for stability design does not accurately account for the stiffness reduction of rotary straightened W-shape columns and beam-columns. A stiffness reduction material model for rotary straightened hot-rolled sections was previously developed and validated for a specific set of cross-section sizes and load conditions. This paper presents a parametric study of the current and proposed stiffness reduction models on hot-rolled steel W-shapes to examine the effect of geometric parameters and different residual stress distributions adopted by AISC 360 and Eurocode on member ultimate capacity. Beam finite element models were created and second-order inelastic analyses were conducted. A range of different cross-section geometries typically used for beam-columns was investigated, which includes various flange and web slendernesses and aspect ratios. Columns and beam-columns were investigated with uniax-

ial bending about the major and minor axes with several axial utilization ratios. The effects of the assumed residual stress pattern on the stability limit state are discussed. The results of the parametric study are presented along with comparisons of the stiffness reduction values for hot-rolled steel members, which provide further understanding of the stiffness reduction model's influence on the stability analysis of rotary straightened hot-rolled steel members.

4.1 Introduction

Structural stability is one of the major design requirements. The current codified steel design rules [1], [4], [10] consider reduced stiffness caused by inelasticity, such as partial yielding accentuated by residual stresses and spread of plasticity through the cross-section and along the member, as the main provision for stability design. It is important to accurately evaluate the effect of residual stress in a structural member because it can lead to the onset of yielding at lower load levels, which results in a reduction of member stiffness that affects the overall member strength. The residual stress distribution in a cross section generally depends on material properties, cross-sectional geometry, and formation processes.

In hot-rolled steel wide-flange members, the intersections between the flange and web lose heat more slowly than the flange tips or mid-web, resulting in residual stresses throughout the cross-section. Several residual stress distributions for hot-rolled W-shape sections have been established based on experimental data over the past decades [71], [129]–[132]. Individual design codes assume different residual stress distributions because various manufacturing techniques are employed in different countries [75]. Fig. 2.3 provides typical residual stress patterns for hot-rolled W-sections. Fig. 2.3a is the distribution measured by Galambos and Ketter [71], also called the Lehigh residual stress pattern, which has uniform tensile stress

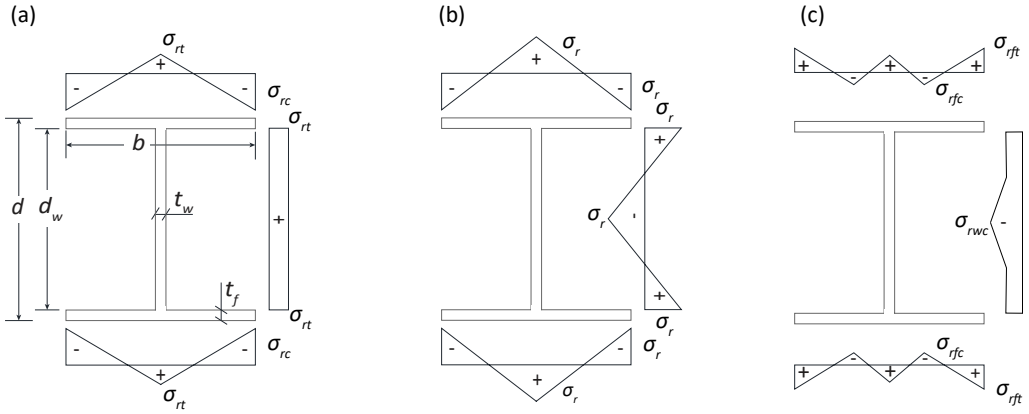

Figure 4.1: Idealized residual stress models (a) Galambos and Ketter [71] (b) ECCS [133] (c) Rotary-straightened hot rolled steel section [3]

in the web and varies linearly across the flanges. The ECCS residual stress profile shown in Fig. 2.3b has linearly varying residual stresses along the flanges and web where the maximum residual stress amplitudes in compression and tension are equal. In addition to the residual stress profiles for conventional hot-rolled W-shapes, Ge and Yura [3] measured residual stresses for rotary-straightened hot-rolled W-shapes, which is shown in Fig. 2.3c. Rotary-straightened cross-sections have a different residual stress pattern compared to those without rotary straightening. The rotarizing process removes or significantly reduces the compressive residual stresses at the flange tips, therefore the resulting rotary-straightened residual stress distribution was shown to have small tensile residual stresses at the flange tips. This affects structural behavior especially in members subjected to inelastic buckling. Since rotary straightening is common practice for steel sections in recent years [3], it is necessary to consider an appropriate residual stress pattern to estimate the stiffness reduction based on the current manufacturing method.

The stability design requirements given in Chapter C of AISC 360-16 [1] account for reduced stiffness by applying a stiffness reduction factor τ in member design equations that determine the required strength of

structural members. This stiffness reduction factor uses a simple inelastic material model that depends only on the utilization ratio of the axial compressive strength of the member and ignores the cross-sectional geometry and bending moment contributions to stiffness reduction. The upcoming version, AISC 360-22 [134], which was previously released for public review, will consider local buckling effects in addition to the axial utilization ratio to estimate τ values. The Lehigh residual stress pattern (Fig. 2.3a) is adopted by the AISC stiffness reduction model. Chapter 6 of Eurocode 3 [4] considers the stiffness reduction by applying an imperfection factor to column strength equations. The imperfection factor is used to implicitly consider the effects of plasticity and geometric imperfections on the structural response. Eurocode 3 [4] adopts the ECCS residual stress profile (Fig. 2.3b).

Various stiffness reduction models for conventional hot-rolled sections, which are not rotary-straightened, have been proposed to account for the spread of plasticity in steel members and frames. Ziemian and McGuire [135] proposed a modified stiffness reduction model based upon the tangent modulus approach by including the effect of the combined axial force and bending moment on members with minor axis bending. Surovek-Maleck and White [136] proposed a method that directly considers residual stresses and initial geometric imperfections within a second-order elastic analysis which eliminates the need for effective length factors. Landesmann and Batista [137] developed stiffness reduction equations building upon the European column buckling curves. Barszcz and Gizejowski [138] proposed separate stiffness reduction expressions for axial and flexural stiffness, which are theoretical functions of member non-dimensional slenderness. Zubydan [139], [140] developed stiffness reduction models that can capture the development of plasticity at the cross-sectional level.

More recently, Kucukler et al. [141] developed stiffness reduction functions that fully capture the influence of the spread of plasticity, residual

stresses, and geometrical imperfections on the column and beam-column capacity, without requiring explicit modeling of geometric imperfections. The model was developed based on the European buckling curves with the ECCS [133] residual stress pattern. The model was validated against nonlinear finite element analyses of members [141] and frames [142] under axial load, bending, and combined axial load and bending. Rosson [143] developed a nonlinear material model for compact wide-flange sections to improve the existing stiffness reduction model by considering both the axial load and bending moment contributions to stiffness reduction. Three-dimensional $m - p - \tau$ surface plots of W-shapes were assessed to determine the perimeter conditions for m, p, and c_r, where m is a normalized moment, p is the axial utilization ratio, and c_r is the ratio of maximum compressive residual stress to yield stress. The model was calibrated on W-shapes with the ECCS residual stress pattern [133] and validated on several cross-sections with small aspect ratios (rectangular sections) with minor or major axis bending. In addition to the stiffness reduction models considering residual stress distributions for conventional hot-rolled W-shapes, Rosson [144] made the necessary adjustments to the previously developed stiffness reduction model [143] to model rotary-straightened hot-rolled steel sections using the residual stress pattern measured by Ge and Yura [3]. The calibrated model for the rotarized W-shapes was validated on limit load analyses of a column and a beam-column subjected to uniaxial bending. Preliminary studies [128] compared the limit loads of rotary-straightened beam-columns to those with the current stiffness reduction model specified in Chapter C of AISC 360 [1], and the results indicated that the current model can result in unconservative W-shape requirements for columns when compared with those obtained using the material model for rotary straightened W-shapes.

The objective of this study is to evaluate the stiffness reduction model for rotary-straightened sections developed by Rosson [144] by comparing

to the existing models in literature [141], [143] and design provisions [1] for conventional hot-rolled sections. This study thus conducted a parametric study of the existing and proposed stiffness reduction models on hot-rolled steel W-shapes. Four different material models were investigated, including the AISC [1] model that incorporates the Lehigh [71] residual stress pattern, the two models [141], [143] based on the ECCS residual stress profile [133], and the model for rotary-straightened sections [144]. The limit load capacity of columns and beam-columns derived by different stiffness reduction models were compared to examine if the current stiffness reduction model in AISC 360 Chapter C [1] is appropriate for rotary-straightened sections. A range of W14 sections was investigated, including both rectangular and square W-shapes, which have various aspect ratios and cross section slenderness ratios. Columns and beam-columns with various member slenderness ratios were analyzed to determine the effect of the stiffness reduction models on the limit loads of structural members. Moreover, the effect of the cross-section dimensional characteristics of W-shapes is examined by estimating correlations between the limit loads and cross-sectional geometric parameters. The significant factors that influence the results of each material model and the effects of the assumed residual stress pattern on the stability limit state are discussed.

In the following sections of this paper, the investigated stiffness reduction models are first described. The finite element (FE) based parametric study is then provided, including the parametric study model inputs, geometric parameters, and FE models of columns and beam-columns. Next, the member limit capacities derived by different stiffness reduction models are compared, and their relationships with geometric parameters are examined.

4.2 The Stiffness Reduction Models

4.2.1 Chapter C of AISC 360

Chapter C of AISC 360-16 [1], which provides the design requirements for the stability of steel structures, determines the required strengths of components with consideration of stiffness reductions due to inelastic behavior resulting from residual stresses and partial yielding of the cross-section. The provisions assume the residual stress distribution measured by Galambos and Ketter [71] (Fig. 2.3a), which has a maximum compressive residual stress σ_{rc} of 30% of the yield stress located at the flange tips and uniform tension σ_{rt} in the web, calculated by $\frac{b \cdot t_f}{b \cdot t_f + t_w \cdot d_w}\sigma_{rc}$, which represents $\frac{A_f}{A_f + A_w}\sigma_{rc}$, where A_f is the flange area, A_w is the web area, and the other geometric parameters are shown in Fig 2.3a. A factor of 0.8 is applied to all components in the structure which contribute to the stability of the structure to reflect the reduced stiffness. Additionally, for components whose flexural stiffnesses affect the stability of the structure, an additional factor τ_b is applied to reflect reduced flexural stiffnesses. When the axial utilization ratio is less than or equal to 0.5, τ_b is taken as 1.0, indicating that there is no reduction in flexural stiffness. Otherwise, the additional factor is determined by Eq. 4.1:

$$\tau_b = 4(\alpha_{AISC}\frac{P_r}{P_{ns}})[1 - (\alpha_{AISC}\frac{P_r}{P_{ns}})] \tag{4.1}$$

where α_{AISC} equals 1.0 for the LRFD method, P_r is a required axial compressive strength, and P_{ns} is the cross-section compressive strength, which equals the yield strength ($P_y = \sigma_y \times A_g$) for nonslender sections. The stiffness reduction relationship is the same regardless of the axis of bending or the presence of bending moment contributing to the loss of flexural stiffness. The stiffness reduction τ for the AISC model is equal to $0.8\tau_b$ in this paper. Fig. 4.2a illustrates the relationship between τ and p of the

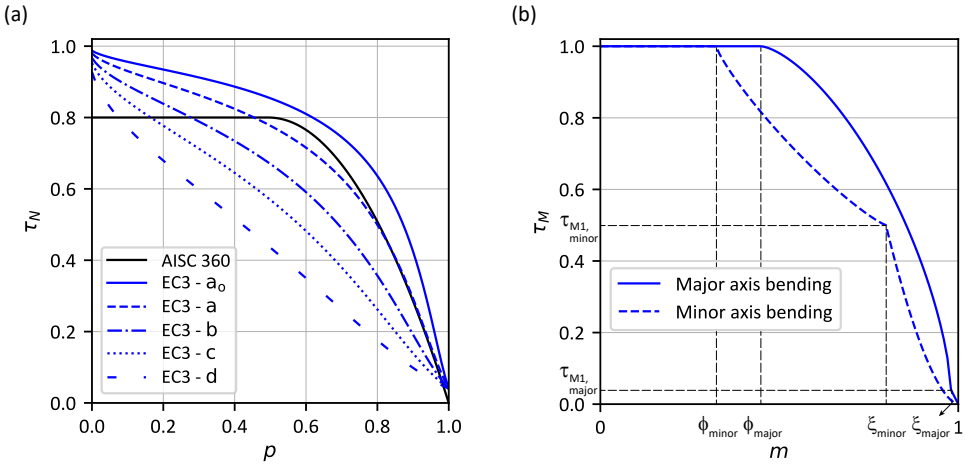

Figure 4.2: The K-ECCS stiffness reduction function due to (a) axial load (b) bending moment

AISC 360 Chapter C model, where p is the applied axial load (P_r) to yield strength ($P_y = P_{ns}$ for nonslender members) ratio , P/P_y. The model will be referred to as "AISC" in this paper.

4.2.2 W-shapes with the ECCS residual stress pattern

Kucukler et al. [141]

Kucukler et al. [141] proposed individual stiffness reduction equations for members under axial compression, bending, or combined axial load and bending. The ECCS [133] residual stress pattern (Fig. 2.3b) was assumed in this stiffness reduction model, which has the maximum tensile and compressive residual stresses σ_r of $0.5\sigma_y$ for W-shapes with $d/b \leqslant 1.2$ or $0.3\sigma_y$ for W-shapes with $d/b > 1.2$, respectively. The model reflects the influence of the spread of plasticity, residual stresses, and geometrical imperfections on the capacity of columns and beam-columns. Explicit modeling of geometric imperfections is not necessary when using their proposed stiffness reduction equations. The stiffness reduction model was

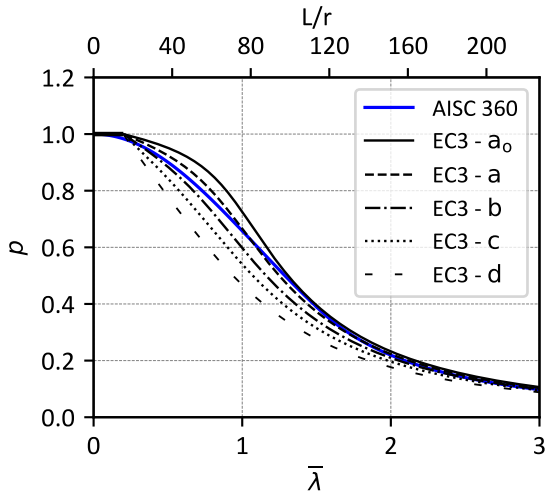

Figure 4.3: Buckling curves provided in the European code EN 1993-1-1 [4] and American code AISC 360 [1]

verified against beam-column results from geometrically and materially nonlinear analyses with imperfections (GMNIA), which directly models residual stresses and geometrical imperfections in a numerical model. The model will be referred to as "K-ECCS" in this paper.

The stiffness reduction factor for axial compressive load τ_N was derived based on the European buckling curves in Fig. 4.3, which presents the relationship of the applied axial load to yield load p and the relative slenderness ratio $\overline{\lambda}$ which can be expressed as $(L_c/\pi r)\sqrt{F_y/E}$, in which L_c is the effective member length determined by $KL = L_c$, where K is the effective length factor, L is member length, and r is the radius of gyration of a cross section about the axis of bending. For stocky members which have relative slenderness ratio $\overline{\lambda}$ less than 0.2, the full resistance of a cross section is used, and the τ_N value for those members equals 0.04. Otherwise, τ_N is calculated by Eq. 4.2:

$$\tau_N = \frac{4\psi^2}{\alpha^2 p\left[1+\sqrt{1-4\psi\frac{p-1}{\alpha^2 p}}\right]^2} \leqslant 1 \tag{4.2}$$

$$\text{where } \psi = 1 + 0.2\alpha p - p$$

where α is the imperfection factor which determines the different shapes of the five buckling curves (Fig. 4.3). The value of α for the buckling curves a_o through d are 0.13, 0.21, 0.34, 0.49, and 0.76, respectively, according to EN 1993-1-1 [4]. In this study, curves a and b are used for rectangular W-shapes ($d/b > 1.2$) with major axis bending and minor axis bending, respectively. Curves b and c are adopted for square W-shapes ($d/b \leqslant 1.2$) with major axis bending and minor axis bending, respectively. The relationship between τ_N and the axial utilization ratio is provided in Fig. 4.2a. Comparing the K-ECCS model with the AISC model, the a_o curve has a larger τ_N value over the range of p. The other curves (a through d) have a lower τ_N value than the AISC curve under higher axial loads.

The stiffness reduction factor for a member under bending, τ_M, was developed based on the moment-curvature relationship of the member. τ_M is obtained by Eqs. 4.3 - 4.5 based on the applied moment ratio m, which is defined as M/M_{px} for major axis bending and M/M_{py} for minor axis bending. Eq. 4.3 is used for W-shapes under low values of bending moment, and Eqs. 4.4 and 4.5 are used for the case of intermediate and high bending moments, respectively:

$$\text{when } m \leqslant \phi \qquad \tau_M = 1.0 \tag{4.3}$$

Table 4.1: Parameters for the K-ECCS model for members in bending

Major axis bending	τ_{M1}	ϕ	ξ	β	δ
$d/b \leqslant 1.2$	0.04	$0.5S_x/Z_x$	0.98	1.5	1.0
$d/b > 1.2$	0.08	$0.7S_x/Z_x$	0.95	1.5	1.0
Minor axis bending	τ_{M1}	ϕ	ξ	β	δ
$d/b \leqslant 1.2$	0.5	$0.5S_y/Z_y$	0.8	0.85	0.6
$d/b > 1.2$	0.6	$0.7S_y/Z_y$	0.75	0.85	0.6

$$\text{when } \phi \leqslant m \leqslant \xi \qquad \tau_M = (1-\tau_{M1})\left[1-\left(\frac{m-\phi}{\xi-\phi}\right)^{\beta}\right]^{1/\beta} + \tau_{M1} \tag{4.4}$$

$$\text{when } \xi \leqslant m \qquad \tau_M = \tau_{M1}\left[1-\left(\frac{m-\xi}{1-\xi}\right)\right]^{1/\delta} \tag{4.5}$$

where the stiffness reduction model parameters, β and δ, the reduced stiffness (y-axis) related parameter τ_{M1}, and the m-range related (x-axis) parameters ϕ and ξ, are provided in Table 4.1 for major and minor axis bending, which were determined by Zubydan [139], [140] to give best fits with fiber model results. S_x and S_y and Z_x and Z_y are the major and minor axis elastic section moduli and plastic section moduli, respectively. Two different sets of parameters are incorporated depending on the depth-to-width ratio, d/b, following the ECCS residual stress pattern [133] which applies different peak residual stresses for square and rectangular W-shapes. The relationship between τ_M and m for a W-shape under pure bending is illustrated in Fig. 4.2b.

The stiffness reduction function for members under combined axial load and bending, τ_{MN}, is derived by using both the stiffness reduction factors for pure axial load τ_N and pure bending τ_M, and is given by Eq. 4.6:

$$\tau_{MN} = \tau_M \tau_N \left\{1-(p)^{\eta}(m)^{\rho}\right\} \tag{4.6}$$

Table 4.2: Parameters for the K-ECCS model for members in combined axial load and bending

Major axis bending	η	ρ
$d/b \leqslant 1.2$	0.5	0.9
$d/b > 1.2$	0.8	1.0
Minor axis bending	η	ρ
$d/b \leqslant 1.2$	0.5	0.5
$d/b > 1.2$	0.5	0.55

where the parameters η and ρ are given in Table 4.2. Two sets of the parameters are provided for each axis of bending according to the cross-sectional depth-to-width ratio d/b. The τ_{MN} expression was validated against results from GMNIA of pinned-pinned beam-columns [141].

Rosson [145]

Rosson [145] developed a stiffness reduction model for compact W-shapes considering the ECCS [133] residual stress pattern (Fig. 2.3b). This model will be referred to as "R-ECCS" in the following sections. As compact doubly-symmetric beam-columns show significantly different behaviors depending on the axis of bending when conducting plastic zone analyses [135], [146], the R-ECCS model is an improvement over the AISC model as it captures the different responses between major and minor axis bending. The stiffness reduction model is developed based on three-dimensional $m - p - \tau$ surface plots generated by a fiber element model for W-shapes, where, as defined previously, m is a moment normalized which is defined as M/M_{px} for major axis bending and M/M_{py} for minor axis bending, p is the applied axial load to yield strength ratio P/P_y, and τ is the stiffness reduction factor. The limit of $\tau = 1.0$ is determined when the m and p conditions generate the sum of three compression stresses equal to the yield stress σ_y, where the compression stresses include the residual compression stress σ_r, the bending moment compression stress σ_m, and

the axial compression stress σ_p. The variable p is positive throughout this paper which requires the same sign for P_y and P, where compression is denoted as positive. The maximum moment at which $\tau = 1.0$, denoted $m(\tau = 1.0)$, for major axis bending is given by Eq. 4.7:

$$m(\tau = 1.0) = \frac{S_x}{Z_x}(1 - c_r - p) \tag{4.7}$$

Eq. 4.7 is independent of the actual shape of the residual stress pattern because it only considers the maximum residual compression stress in the flange. The ratio of maximum compressive residual stress at the flange tips to yield stress, c_r, is 0.5 for square W-shapes with $d/b > 1.2$ or 0.3 for rectangular sections with $d/b \leqslant 1.2$ following the ECCS residual stress pattern [133]. The maximum moment at which $\tau = 1.0$ for minor axis bending is given by Eq. 4.8:

$$m(\tau = 1.0) = \frac{S_y}{Z_y}(1 - c_r - p) \tag{4.8}$$

Similar to Eq. 4.7, the actual residual stress pattern does not affect Eq. 4.8 as it is based on the flange tip compression stress magnitude. Fig. 4.4 illustrates an example of the $\tau = 1.0$ condition for R-ECCS with major or minor axis bending.

To determine the m condition when $\tau = 0$ (denoted $m(\tau = 0)$) for major axis bending, the required equation is dependent on the plastic neutral axis location in a cross-section. The equation is independent of the shape of the residual stress distribution. Eq. 4.9 is used when the plastic neutral axis is outside the flange, which is the case for W-shapes under low axial compression loads, and Eq. 4.10 is used for W-shapes under high values of axial compression, when the plastic neutral axis is inside the flange thickness:

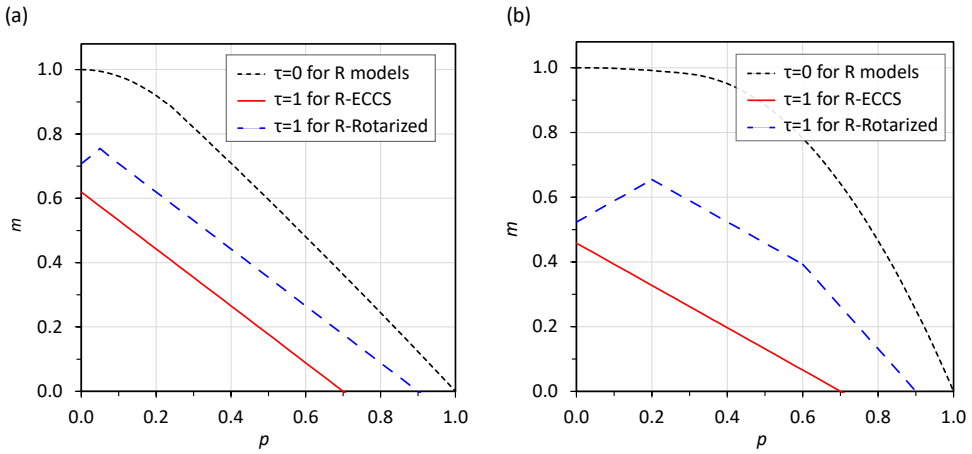

Figure 4.4: $\tau = 1.0$ and $\tau = 0$ perimeter conditions for W14x82 beam-column with (a) major axis bending (b) minor axis bending

$$when\ p < \frac{\lambda}{2+\lambda} \qquad m(\tau = 0) = 1 - \frac{p^2(2+\lambda)^2}{(4\lambda_o + \lambda(4+\lambda)} \tag{4.9}$$

$$when\ p \geqslant \frac{\lambda}{2+\lambda} \qquad m(\tau = 0) = \frac{(2+\lambda_1)^2 - [p(2+\lambda) - \lambda + \lambda_1]^2}{4 + \lambda_1(4+\lambda)} \tag{4.10}$$

where $\lambda = A_w/A_f$ is the ratio of web to flange areas, $\lambda_o = t_w/b_f$ is the ratio of web thickness to flange width, and $\lambda_1 = d_w/t_f$ is the ratio of web depth to flange thickness.

For the minor axis bending condition, Eq. 4.11 is used when the plastic neutral axis is inside the web, which occurs in wide-flange sections under low values of axial compressive load, and Eq. 4.12 is used for the sections with high axial loads, which have the plastic neutral axis outside the web thickness:

$$when\ p < \frac{2\lambda_o + \lambda}{2 + \lambda} \qquad m(\tau = 0) = 1 - \frac{p^2(2+\lambda)^2}{(2 + \lambda\lambda_o)(2 + \lambda_1)} \tag{4.11}$$

$$when\ p \geqslant \frac{2\lambda_o + \lambda}{2 + \lambda} \qquad m(\tau = 0) = \frac{4 - [p(2+\lambda) - \lambda]^2}{2(2 + \lambda\lambda_o)} \tag{4.12}$$

The perimeter condition of uniaxial bending when $\tau = 0$ is illustrated in Fig. 5.2. A $\tau = 0$ indicates that no flexural stiffness remains in the cross-section for the given m and p conditions. Fig. 5.2 graphically illustrates the stiffness reduction regions. The region below the $\tau = 1.0$ line, inside the triangular shape, represents the moment and axial load conditions of no stiffness reduction ($\tau = 1.0$). The stiffness reduction factor τ in the region between $\tau = 1.0$ and $\tau = 0$ curves is provided by Eq. 4.13 and Eq. 4.14:

$$when\ p < 1 - c_r \qquad \tau = 1 - \left[\frac{m - m(\tau = 1.0)}{m(\tau = 0) - m(\tau = 1.0)}\right]^n \tag{4.13}$$

$$when\ p \geqslant 1 - c_r \qquad \tau = \left[\frac{1-p}{c_r}\right]\left[1 - \frac{m}{m(\tau = 0)}\right]^n \tag{4.14}$$

where n is an independent input. This study used n equal to 4 and 2 for major axis bending and minor axis bending, respectively, following Rosson and Ziemian [147], for modeling W-shapes with the ECCS residual stress pattern. The values for $m(\tau = 1.0)$ and $m(\tau = 0)$ depend on the axis of bending under consideration.

4.2.3 Rotary-straightened W-shapes

Rosson [144] developed a stiffness reduction model for rotary-straightened W-shapes based on the residual stress pattern (Fig. 2.3c) examined by Ge and Yura [3]. The model will be referred to as "R-Rotarized" in this paper. In contrast to the ECCS pattern [133], which has the maximum compressive residual stresses (σ_{rfc}) at the flange tips, rotary-straightened sections have the maximum residual tensile stresses (σ_{rft}) at the flange tips. This will result in different initial yield load conditions. The maximum compression residual stresses of rotary-straightened sections occur at the quarter-point of the flanges with a reduced magnitude compared to the sections without the rotary-straightening process. The equations for maximum moment $m(\tau = 1.0)$ in Eq. 4.7 and Eq. 4.8 are modified to consider this different residual stress pattern of rotary-straightened W-shapes. The maximum moment when $\tau = 1.0$, denoted $m(\tau = 1.0)$, prior to initial flange tension yield under low axial compression conditions for major axis bending is given in Eq. 4.15:

$$when\ p \leqslant \frac{c_r^+ - c_r^-}{2} \qquad m(\tau = 1.0) = \frac{S_x}{Z_x}(1 - c_r^+ + p) \qquad (4.15)$$

where c_r^+ is the ratio of maximum tensile residual stress, σ_{rft}, to σ_y and c_r^- is the ratio of maximum compressive residual stress, σ_{rfc}, to σ_y. This study used $c_r^- = 0.1$ and $c_r^+ = 0.2$ based on the values $\sigma_{rfc} = 5$ ksi and $\sigma_{rft} = 10$ ksi estimated by Ge and Yura [3]. Eq. 4.16 is used to calculate the maximum moment prior to flange initial compression yield under medium and high axial compression conditions for major axis bending:

$$when\ \frac{c_r^+ - c_r^-}{2} < p \leqslant 1 - c_r^- \qquad m(\tau = 1.0) = \frac{S_x}{Z_x}(1 - c_r^- - p) \quad (4.16)$$

An example of the maximum m and p conditions without stiffness reduction for rotary-straightened sections with major axis bending is shown as $\tau = 1.0$ of R-Rotarized in Fig. 4.4a. The region below the $\tau = 1.0$ curve indicates that there is no stiffness reduction. The $\tau = 0$ curve is the same for the R-Rotarized and R-ECCS models.

For beam-columns under minor axis bending, the maximum moment prior to initial tension yield under low axial compression conditions is determined by Eq. 4.17, and the maximum moment prior to initial compression yield under moderate or high axial compression conditions is determined using Eq. 4.18 or Eq. 4.19, respectively:

$$when\ p \leqslant c_r^+ \qquad m(\tau = 1.0) = \frac{S_y}{Z_y}(1 - c_r^+ + p) \tag{4.17}$$

$$when\ c_r^+ < p \leqslant 1 - 2c_r^- + c_r^+ \qquad m(\tau = 1.0) = \frac{S_y}{Z_y}(1 + c_r^+ - p) \tag{4.18}$$

$$when\ 1 - 2c_r^- + c_r^+ < p \leqslant 1 - c_r^- \qquad m(\tau = 1.0) - = \frac{2S_y}{Z_y}(1 - c_r^- - p) \tag{4.19}$$

The m and p conditions when $\tau = 1.0$, defined in Eq. 4.17 - 4.19, are illustrated in Fig. 4.4b as $\tau = 1.0$ of R-Rotarized.

Using the calculated $m(\tau = 1.0)$, Eqs. 4.13 - 4.14 are used to determine the stiffness reduction τ, where c_r^- is used for c_r in Eq. 4.14. The n values of 1.5 and 1.2 are used for major axis bending and minor axis bending, respectively, following Rosson [144], for modeling rotary-straightened W-shapes.

4.3 Parametric study model inputs

A finite element (FE) based parametric study of the stiffness reduction models on hot-rolled steel W-shapes is conducted. This section presents the inputs for the parametric study, including stiffness reduction models, load and geometric parameters, and the FE model details.

4.3.1 Stiffness reduction models

The four stiffness reduction models presented in Section 4.2 are considered in the parametric study. Table 5.1 summarizes the referred names of the models, the assumed residual stress patterns to estimate stiffness reduction, and the equations used for deriving the τ value.

Table 4.3: Stiffness reduction models

Name	Stiffness reduction model	Assumed residual stress pattern	Stiffness reduction factor	Equations
AISC	AISC 360 [1]	Lehigh [71]	$0.8\tau_b$	Eq. 4.1
K-ECCS	Kucukler et al. [141]	ECCS [133]	τ_N for columns	Eq. 4.2
			τ_{MN} for beam-columns	Eqs. 4.2 - 4.6
R-ECCS	Rosson [145]	ECCS [133]	τ	Eqs. 4.7 - 4.14
R-Rotarized	Rosson [144]	Ge and Yura [3]	τ	Eqs. 4.13 - 4.19

4.3.2 Load and geometric parameters

A range of compact W14 sections given in the companion manual for AISC 360 [1] were selected with a variety of geometric properties. This study considered the influence of axial utilization ratio, member slenderness, and the relevant cross-sectional geometric ratios which are known to govern the behavior of steel columns and wide-flange cross-sections. The parameters considered in the study are:

1. Axial utilization ratio, p, which can be expressed as P/P_y, where P is the applied axial load and P_y is the yield load.

2. Member slenderness, L/r, where L is the member length and r is r_x or r_y depending on the axis of bending under consideration.

3. Aspect ratio, b/d, which is the ratio of section width to overall section depth. Aspect ratios closer to 1 indicate a square footprint which are more common for columns, while smaller aspect ratios indicate a rectangular footprint which are more common for beams. The b/d effect is reflected in a yield surface equation for doubly symmetrical steel sections [148]. In addition, the ECCS residual stress pattern [133] determines the maximum residual stresses in a cross-section based on d/b, which is the inverse of the aspect ratio b/d.

4. The ratio of flange-to-web-area, A_f/A_w, where A_f is the flange area and A_w is the web area. This ratio significantly affects the distribution of residual stresses [149]. A section with $A_f/A_w = 1.0$ represents a light-weight section, and a section with a large A_f/A_w indicates a heavy-weight section [148]. This ratio is equal to the $\frac{1}{\lambda}$ value presented in Rosson [143].

5. Flange element restraint, b_f/t_w, which reflects how the web restrains the flange element. Consider a constant b_f: a larger b_f/t_w indicates

that the web is less thick and hence provides a reduced edge support to the flange than a thicker web which would produce a smaller b_f/t_w ratio. This is equal to the inverse of λ_o presented in Rosson [143].

6. Web element restraint, d_w/t_f, which reflects how the flange restrains the web element. Consider a constant d_w: a larger d_w/t_f indicates that the flange is less thick and hence provides a reduced edge support to the web than a thicker flange which would produce a smaller d_w/t_f ratio. This is equal to the λ_1 value presented in Rosson [143].

4.3.3 Finite element model

Beam element FE models were created in MASTAN2 [12], and second-order inelastic analyses were conducted. The steel material was defined with a yield stress of 50 ksi and Young's modulus of 29,000 ksi. The FE models are restrained from out-of-plane behavior, and all of the members in the study were fully compact per AISC Section B4 definition. The limit load capacities of steel members were evaluated by using the $0.8\tau_b$ values determined by Eq. 4.1 for the AISC model. The K-ECCS model utilized τ_N derived from Eq. 4.2 for the stiffness reduction factor for columns and τ_{MN} derived from Eqs. 4.2 - 4.6 for the stiffness reduction factor for beam-columns. The R-ECCS model applied τ obtained from Eqs. 4.7-4.14, and the R-Rotarized model applied τ obtained from Eqs. 4.13-4.19.

Columns were investigated with the applied load condition of axial compression only. Fig. 4.5 illustrates a pinned-pinned column that consists of ten line elements. The initial geometric imperfections of L/1000 at mid-height were applied for columns with the AISC, R-ECCS, and R-Rotarized stiffness reduction models. For columns with the K-ECCS model, initial geometric imperfections were not modeled because the K-ECCS model includes the effect of imperfections by applying the imperfection factor α.

Figure 4.5: Column model

An axial load P with a step size of 0.01 was incrementally applied until the column reached the ultimate load.

Beam-columns were investigated with applied axial compression with uniaxial bending about the major or minor axis. Fig. 4.6 illustrates a pinned-pinned beam-column subdivided into twenty line elements. An initial geometric imperfection of a half sine wave with an amplitude of L/1000 at the mid-height of members was modeled for beam-columns with all the stiffness reduction models except the K-ECCS model which implicitly considers the effect of geometric imperfections. Several axial utilization ratios p of 0.3, 0.5, and 0.7 were applied to the beam-columns. The axial load P corresponding to p$\times$50 ksi was first applied in one step and then the horizontal load H was incrementally applied with a step size of 0.01 until the beam-column reached the limit load.

4.4 Results

4.4.1 Columns

Limit load analyses on steel columns were first investigated to observe the effect of the stiffness reduction models on the load capacity between two different cross-sections, W14x48 and W14x550. Member slenderness ratios,

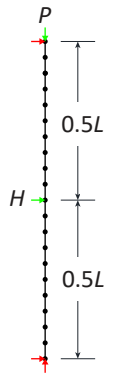

Figure 4.6: Beam-column model

L/r, in the inelastic range including 40, 60, 80, 100, and 120 were explored in the column models, where r is the radius of gyration of a cross-section. Either r_x (major) or r_y (minor) is used depending on the axis of bending to calculate the length of the member. Fig. 4.7 shows the column strength results of the W14x48 and W14x550 members bending about either the major or minor axis. One square and one rectangular W-shape each were selected to examine if the various stiffness reduction models had different results depending on the cross-section geometry as the selected sections have substantially different cross-sectional properties. The differences between the stiffness reduction models are most significant in the range of $40 \leqslant L/r \leqslant 80$ and then decrease for $L/r \geqslant 100$. The W14x550 column with $L/r = 60$ shows the largest percent differences between the models, which are 14.6% and 17.2% for major and minor axis bending, respectively. The results demonstrate the known effect that residual stresses affect the limit load of columns in the inelastic buckling range more than in the elastic buckling range [75], [147]. The significant observations regarding the comparisons between the four stiffness reduction models as illustrated in Fig. 4.7 are provided as follows:

AISC: Comparing the results of major and minor axis bending, it is observed that the AISC column strengths are unaffected by the axis

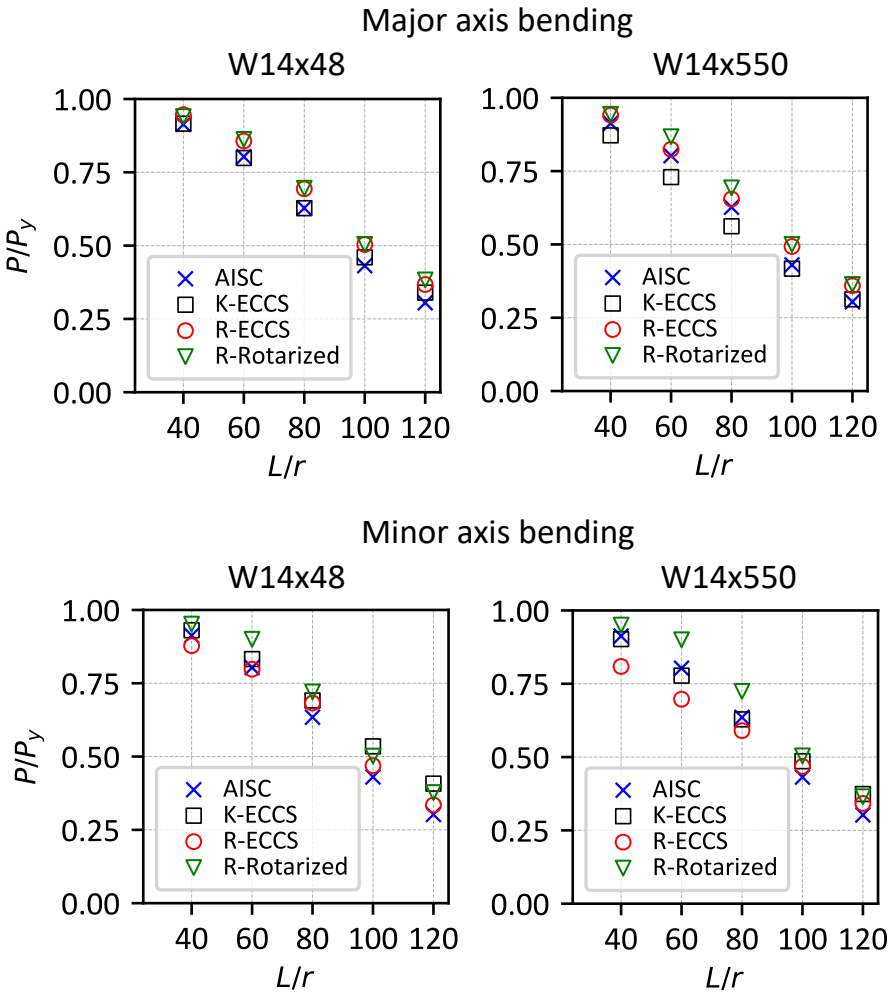

Figure 4.7: Column strength results of W14x48 and W14x550

of bending since the AISC model used the same equation to estimate τ for both bending axis cases. Moreover, since the AISC model does not consider cross-sectional geometry to estimate τ, negligible differences between W14x48, a rectangular W-shape ($b/d < 0.83$), and W14x550, a square W-shape ($b/d \geqslant 0.83$), were observed.

K-ECCS: Comparing the results of W14x48 and W14x550 with either of major or minor axis bending, the W14x550 column shows a smaller capacity than the W14x48 column. This is because the K-ECCS model applies conservative buckling curves (Fig. 4.3) to square W-shapes relative to rectangular W-shapes to reflect different residual stress magnitudes of the ECCS sections depending on the aspect ratio.

R-ECCS and R-Rotarized: As shown in the major axis bending results, in the full range of L/r, the R-ECCS and R-Rotarized models show higher strength values compared to the AISC and K-ECCS models. The $\tau = 1.0$ region (Fig. 5.2a) in the R-ECCS and R-Rotarized models led to a larger ultimate capacity compared with the other models. R-ECCS and R-Rotarized show almost equal results for W14x48, but capacity differences are observed in the W14x550 results because W14x550 incorporates a larger residual stress magnitude of $0.5\sigma_y$, which differs to a large extent from the maximum residual stress for rotary-straightened sections, $0.2\sigma_y$, as previously discussed in Section 4.1 for Fig. 2.3. Moreover, according to the minor axis bending results, the R-Rotarized columns show a significant difference from the other columns due to a large $\tau = 1.0$ plateau of the R-Rotarized model for minor axis bending (Fig. 5.2b).

4.4.2 Beam-column

This section investigates beam-columns under combined axial compression and uniaxial bending with a range of different cross-section geometries including aspect ratio, flange-to-web area ratio, and flange and web element restraints. Eight W14 shapes were evaluated to determine if the W-shapes

Table 4.4: Selected W-shapes and cross-sectional properties

Section	b/d	A_f/A_w $(1/\lambda)$	$b_f/2t_f$	d_w/t_w	b_f/t_w $(1/\lambda_o)$	d_w/t_f (λ_1)
W14x48	0.58	1.11	6.75	33.60	23.62	21.19
W14x61	0.72	1.34	7.75	30.40	26.67	19.55
W14X82	0.71	1.36	5.92	22.40	19.80	14.73
W14x109	1.02	1.90	8.49	21.70	27.81	14.63
W14x159	1.04	1.97	6.5	15.3	20.94	10.61
W14x211	1.01	2.00	5.1	11.6	16.12	8.06
W14x283	0.96	2.06	3.89	8.84	12.48	6.07
W14x550	0.85	2.09	2.25	4.79	7.23	3.29

Note: Sections with $b/d < 0.83$ are classified as rectangular W-shapes, and sections with $b/d \geqslant 0.83$ are classified as square W-shapes per the ECCS [133] residual stress pattern

commonly used in structural design show similar behaviors among the various stiffness reduction models. The cross-sectional geometric parameters of the selected W-shapes are listed in Table 4.4. Member slenderness ratios L/r that range between 40 to 120 with increments of 20 were examined. The limit load was normalized to $M/M_p = (HL/4)/(F_y Z)$, where Z is plastic section modulus; either Z_x or Z_y depending on the axis of bending, major or minor, respectively.

Major axis bending

The capacities of beam-columns with major axis bending estimated by the four stiffness reduction models are compared in Fig. 4.8 through scatter plots of the normalized capacity versus the width-to-depth ratio b/d. Slenderness ratios of 40 and 60 were selected because they are in the inelastic buckling range where significant yielding of a cross-section can occur at failure and where residual stresses are most influential on member capacity as discussed in Section 4.4.1. As expected, the $L/r = 60$ columns have lower normalized capacities than the $L/r = 40$ columns as they are more slender. The significant observations regarding the comparisons between the four models as illustrated in Fig. 4.8 are provided with regards to

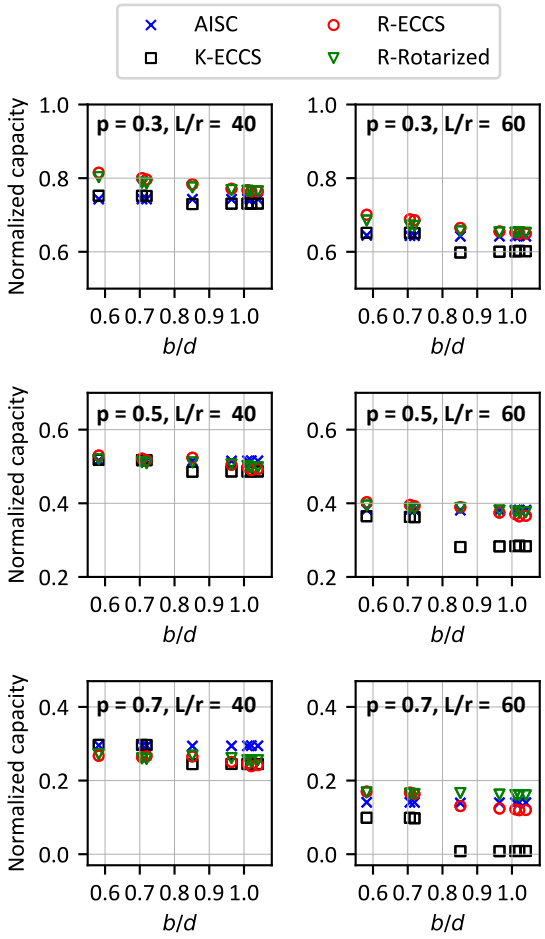

Figure 4.8: Scatter plots of the normalized capacity of L/r =40 and 60 beam-columns with major axis bending with p = 0.3, 0.5, and 0.7

aspect ratio (b/d), axial load (p), and member slenderness (L/r).

AISC: The AISC model resulted in a consistent normalized capacity over the range of b/d because it ignores the effect of cross-sectional geometries on stiffness reduction. With regards to axial load p, AISC applies the same value of the stiffness reduction factor τ_b when p = 0.3 and p = 0.5 and a larger reduction when p = 0.7 as shown in Fig. 4.9. The AISC model shows no significant differences between the two L/r values.

K-ECCS: For each p and L/r scenario, the K-ECCS model showed differences between rectangular ($b/d < 0.83$) and square ($b/d \geqslant 0.83$) W-shapes. This is because a different residual stress magnitude is assumed depending on the aspect ratio and thus the model adopts a different buckling curve to estimate the stiffness reduction factor, which is curve *a* (Fig. 4.3) for rectangular W-shapes and curve *b* for square sections. Square sections, which contain larger residual stresses compared with rectangular sections, adopt a more conservative buckling curve. The differences between rectangular and square aspect ratios become more pronounced with higher values of axial load and member slenderness. Although the sameτ values were used for both slenderness ratios, the $L/r = 60$ members with higher p are more subjected to inelastic behavior due to partial yielding. Furthermore, the stiffness reduction for square aspect ratios is larger than for rectangular aspect ratios, as shown in Fig. 4.9, and therefore the square W-shapes with high p can carry minimal bending prior to failure.

R-ECCS and R-Rotarized: The R- models directly consider the influence of geometric parameters therefore their capacities varied over the range of aspect ratios. The R-ECCS and R-Rotarized results are closely aligned under the low and medium axial loads of $p = 0.3$ and $p = 0.5$ while they show the greatest differences under high axial load, $p = 0.7$. At $p = 0.7$, as the moments over the length begin to increase as a lateral load H is applied, the initial stiffness reduction for the R-ECCS members is more pronounced and has more of an effect on the limit load than the R-Rotarized members, thus the R-ECCS members have a lower normalized capacity. At $p = 0.3$ and 0.5, the differences in the initial stiffness reduction are less pronounced, and the capacity results are more closely aligned.

In summary, the largest difference in the results between the four models is for square aspect ratios with medium and high applied axial loads for $L/r = 60$ columns, especially when comparing K-ECCS to the

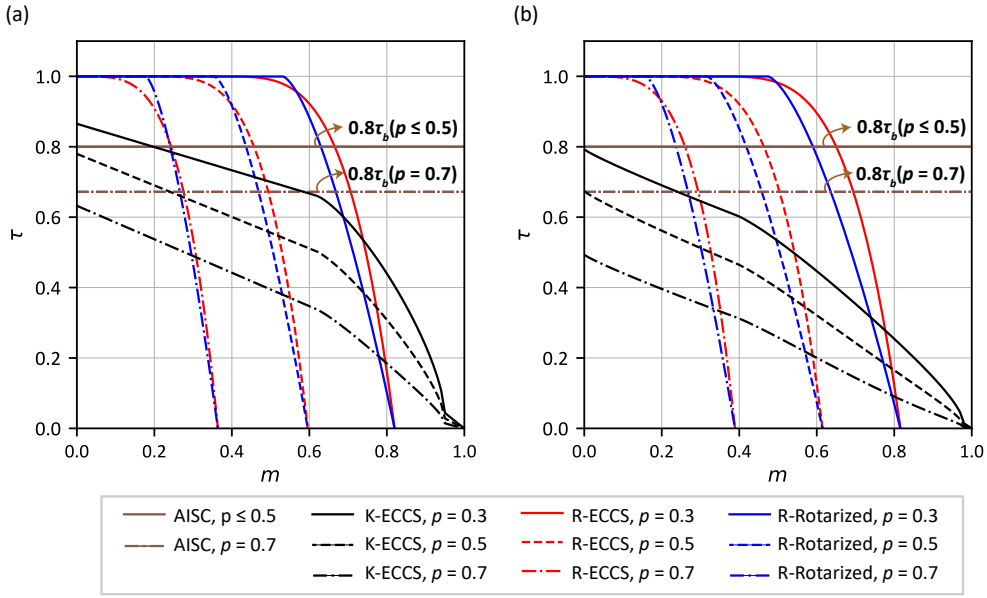

Figure 4.9: τ - m relationships when p $= 0.3$, p $= 0.5$, and p $= 0.7$ for (a) a narrow section (W14x82) (b) a wide section (W14x550) with major axis bending

other three models.

Minor axis bending

Fig. 4.10 shows the scatter plots of the L/r $= 40$ and 60 beam-columns subjected to minor axis bending under various axial utilization ratios. As expected, the L/r $= 60$ columns have lower normalized capacities than the L/r $= 40$ columns as they are more slender. The significant observations regarding the comparisons between the four models as illustrated in Fig. 4.10 are provided with regards to aspect ratio (b/d), axial load (p), and member slenderness (L/r).

AISC: Similar to major axis bending, the AISC model shows constant capacities across aspect ratios because it does not consider the effect of cross-sectional geometries to estimate the stiffness reduction factor τ. As a consequence, the AISC model shows an overprediction relative to the other models in some conditions, such as for square aspect ratio shapes

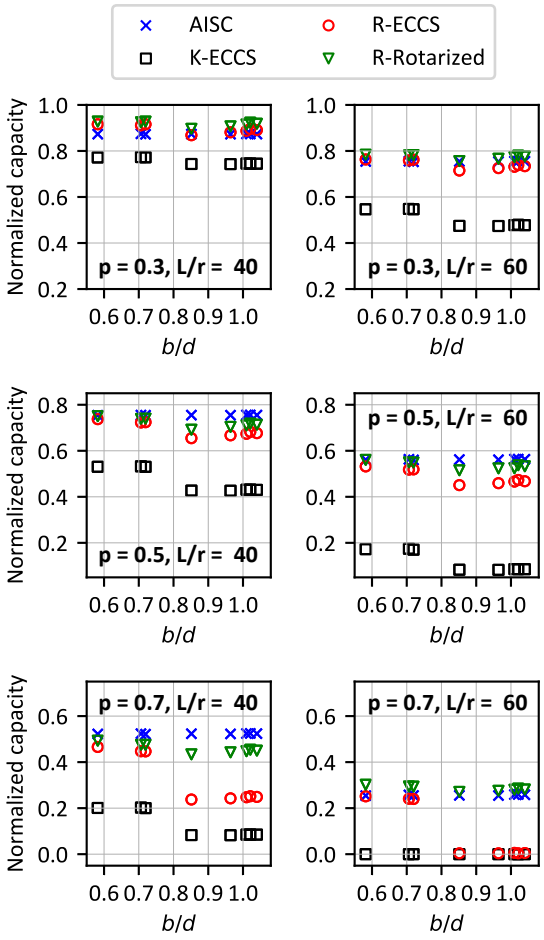

Figure 4.10: Scatter plots of the capacity of L/r =40 and 60 beam-columns with minor axis bending with varying p

with low and high axial load for $L/r = 40$. The AISC model for minor axis bending does not consider reduced flexural stiffness until $p = 0.5$ nor bending moment contribution to stiffness reduction.

K-ECCS: The K-ECCS model shows a difference between square and rectangular aspect ratios since the ECCS residual stress pattern [133] assumes different residual stress magnitudes depending on the aspect ratio, $0.5F_y$ for $b/d \geqslant 0.83$ and $0.3F_y$ for $b/d < 0.83$. The K-ECCS model applies curves b and c (Fig. 4.3) for rectangular sections and square sections, respectively, which are more conservative than the curves used for major axis bending. Comparing the τ-m relationships between rectangular and square sections with minor axis bending (Fig. 4.11), the square section with K-ECCS has lower τ curves than the rectangular section under the same p and m conditions. Therefore, in some cases where K-ECCS members are under high p and high L/r such as the $L/r = 60$ members with the $p = 0.7$ condition, the K-ECCS sections have significant stiffness reduction and therefore resist much lower lateral loads compared with the other three models.

R-ECCS and R-Rotarized: The capacity difference between the R-ECCS and R-Rotarized models is larger compared to major axis bending due to the significantly different shape of the plateau when $\tau = 1.0$ for minor axis bending. As previously discussed in Section 4.3.1, R-ECCS applies one linear function for the maximum moment when $\tau = 1.0$, but R-Rotarized involves three different $m(\tau = 1.0)$ equations depending on the p magnitudes. Moreover, with large residual stresses for square R-ECCS sections under $p = 0.7$, the whole length of the column experiences stiffness reduction merely due to the application of p, then when a lateral load is applied there is minimal capacity left. With low or medium axial loads, such as $p = 0.3$ and 0.5, however, yielding only begins when a lateral load is applied.

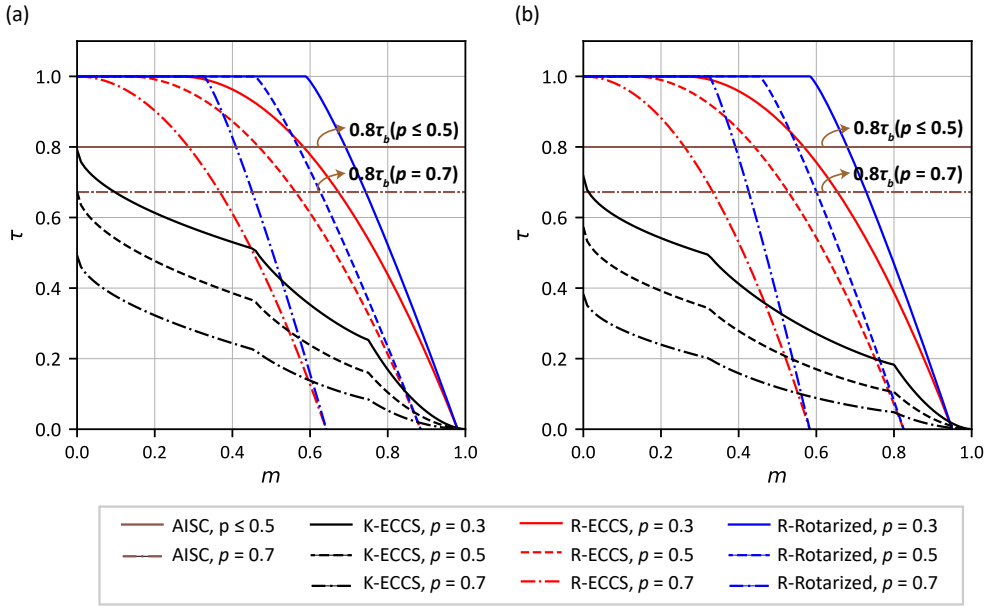

Figure 4.11: τ - m relationships when $p = 0.3$, $p = 0.5$, and $p = 0.7$ for (a) a narrow section (W14x82) (b) a wide section (W14x550) with minor axis bending

4.4.3 Correlations between the geometric parameters and capacity

In addition to the comparisons of the limit load from W14 beam-columns resulting from the various stiffness reduction models, which was reflected as the normalized moment $M/M_p = (HL/4)/(F_y Z)$, correlation relationships between the geometric parameters and the normalized moment capacity were explored for the expanded range of member slenderness to examine the effect of residual stresses and stiffness reduction in more slender members. The Pearson's correlation coefficient ρ given in Eq. 4.20 was utilized to measure a linear correlation:

$$\rho = \frac{cov(X, Y)}{\sigma_X \sigma_Y} \tag{4.20}$$

where cov is the covariance, σ_X is the standard deviation of a variable X, which is the normalized limit load obtained from FE analyses, and σ_Y

is the standard deviation of a variable Y, which is a geometric parameter in this study, such as b/d, A_f/A_w, b_f/t_w, and d_w/t_f. This study assumed the correlation was strong when the correlation absolute value was greater than 0.9.

Fig. 4.12 and Fig. 4.13 summarize the correlation coefficients of the W14 beam-column capacities having L/r ranging from 40 to 120 in increments of 20 and p of 0.3, 0.5, and 0.7. Each heat map represents the correlation results of the stiffness reduction models. The blue-colored cells indicate a positive correlation between the normalized moment capacity and the parameters, while the red-colored cells indicate a negative correlation. The investigated parameters were described in Section 4.3.2. When members are relatively slender, $L/r \geqslant 80$, in some cases the beam-columns reached the limit load prior to the full application of p. This situation was more prevalent with the AISC and K-ECCS models than the R-ECCS and R-Rotarized models. This is because for members that can carry only small m, such as slender members, the AISC and K-ECCS models apply τ values less than 1.0 even when $m = 0$ whereas the R- models have the $\tau = 1.0$ plateau, as shown in Fig. 4.9. The correlation coefficients were not evaluated in those cases. Particularly, K-ECCS with minor axis bending often showed this situation because the model uses buckling curves b and c (Fig. 4.3), which are more conservative than buckling curves a and b used for major axis bending.

Major axis bending

The significant observations regarding the comparisons between the four stiffness reduction models as illustrated in Fig. 4.12 are provided as follows:

AISC: Most parameters in the AISC model are shown to have at least a moderate correlation with the capacity, $\rho > 0.5$. A strong correlation, $\rho > 0.9$, occurred only in a few parameters, such as A_f/A_W and d_w/t_f, under some p or L/r conditions. A consistent normalized capacity was

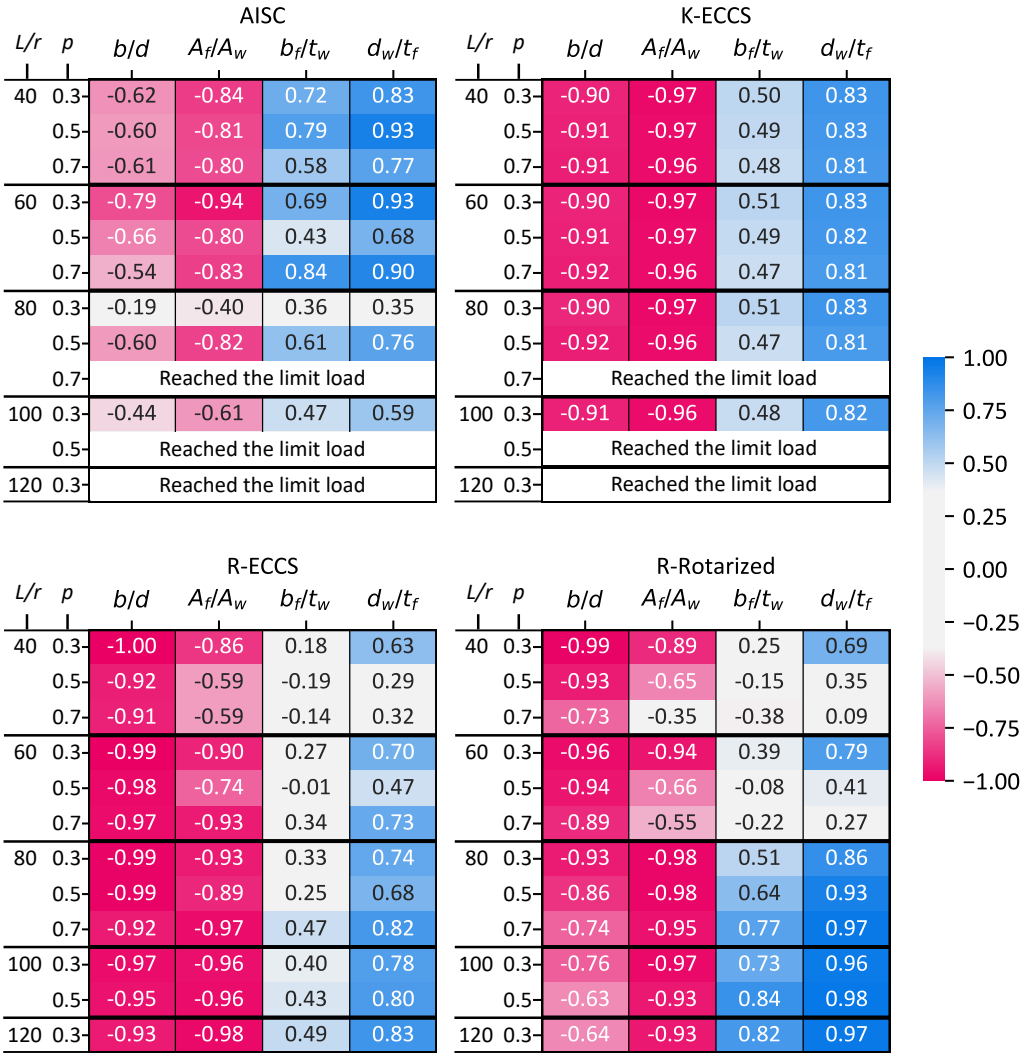

Figure 4.12: Correlation values of the W14 beam-columns with major axis bending. Blue = positive correlation, Red = negative correlation.

AISC

L/r	p	b/d	A_f/A_w	b_f/t_w	d_w/t_f
40	0.3	0.19	0.06	-0.04	-0.14
	0.5	0.70	0.51	0.02	-0.36
	0.7	0.65	0.52	-0.09	-0.41
60	0.3	0.43	0.22	0.05	-0.18
	0.5	0.58	0.36	0.04	-0.26
	0.7	0.66	0.36	0.24	-0.16
80	0.3	0.49	0.15	0.37	0.04
	0.5	0.50	0.20	0.26	-0.05
	0.7	Reached the limit load			
100	0.3	0.46	0.13	0.35	0.04
	0.5	Reached the limit load			
120	0.3	Reached the limit load			

K-ECCS

L/r	p	b/d	A_f/A_w	b_f/t_w	d_w/t_f
40	0.3	-0.89	-0.96	0.50	0.82
	0.5	-0.90	-0.96	0.49	0.82
	0.7	-0.91	-0.96	0.48	0.81
60	0.3	-0.90	-0.97	0.50	0.83
	0.5	-0.91	-0.96	0.48	0.81
	0.7	Reached the limit load			
80	0.3	-0.90	-0.97	0.49	0.82
	0.5	Reached the limit load			
	0.7	Reached the limit load			
100	0.3	Reached the limit load			
	0.5	Reached the limit load			
120	0.3	Reached the limit load			

R-ECCS

L/r	p	b/d	A_f/A_w	b_f/t_w	d_w/t_f
40	0.3	-0.67	-0.95	0.80	0.96
	0.5	-0.83	-1.00	0.66	0.93
	0.7	-0.91	-0.98	0.50	0.84
60	0.3	-0.73	-0.97	0.75	0.95
	0.5	-0.86	-1.00	0.63	0.91
	0.7	-0.92	-0.97	0.47	0.81
80	0.3	-0.80	-0.98	0.68	0.92
	0.5	-0.87	-0.99	0.59	0.89
	0.7	-0.93	-0.97	0.46	0.81
100	0.3	-0.80	-0.97	0.64	0.88
	0.5	-0.87	-0.99	0.59	0.89
120	0.3	-0.64	-0.94	0.75	0.91

R-Rotarized

L/r	p	b/d	A_f/A_w	b_f/t_w	d_w/t_f
40	0.3	-0.42	-0.82	0.93	0.94
	0.5	-0.75	-0.98	0.75	0.96
	0.7	-0.81	-0.99	0.67	0.94
60	0.3	-0.38	-0.80	0.92	0.92
	0.5	-0.74	-0.97	0.76	0.96
	0.7	-0.75	-0.98	0.75	0.96
80	0.3	-0.32	-0.75	0.94	0.89
	0.5	-0.62	-0.92	0.81	0.95
	0.7	-0.39	-0.71	0.70	0.76
100	0.3	-0.01	-0.49	0.89	0.69
	0.5	-0.17	-0.57	0.70	0.63
120	0.3	-0.24	-0.66	0.90	0.83

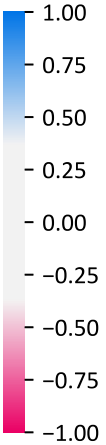

Figure 4.13: Correlation values of the W14 beam-columns with minor axis bending. Blue = positive correlation, Red = negative correlation.

obtained by the AISC model (Fig. 4.8) because it ignored the effect of cross-sectional geometry. The AISC normalized capacity showed a difference of less than 0.005 over the range of parameters while for comparison the other models had a difference greater than 0.1, which indicates a negligible change in the AISC results. This resulted in relatively weak correlation coefficients compared with the other stiffness reduction models, and it is difficult to justify that the magnitude of the geometric parameters is sensitive to the AISC model.

K-ECCS: The parameters have relatively equivalent correlation values over the p and L/r values compared with the other models. This is because each group of rectangular and square sections showed a consistent capacity as previously shown in Fig 4.8. The K-ECCS model shows b/d as a significant factor because the ECCS residual stress pattern adopts different residual stress magnitudes depending on the aspect ratio. Moreover, the ratio of flange-to-web-area A_f/A_w shows a strong negative correlation. As shown in Fig. 4.14, the capacity of the K-ECCS members with large A_f/A_w, which were classified as square sections in Table 4.4, is lower than those with small A_f/A_w. Square sections following the ECCS residual stress pattern adopt a more conservative factor to estimate τ than rectangular sections, leading to a negative correlation between the capacity and A_f/A_w.

R-ECCS and R-Rotarized: For R-ECCS and R-Rotarized models, which directly reflect the effect of cross-sectional geometric parameters in estimating τ, b/d has a higher correlation under lower axial loads. As shown in Fig. 4.9, the $p = 0.3$ condition has small or no stiffness reduction over a wide range of m from 0 to 0.6. Without the stiffness reduction, the cross-section can support more load before failure, which could result in parts of the cross-section reaching the yield strength. Under major axis bending, the flanges resist the applied bending, and as such the aspect ratio, b/d, influences the strength under low p. A_f/A_w has a significant correlation

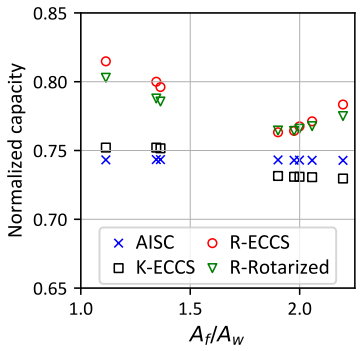

Figure 4.14: Scatter plot of the capacity of $L/r = 40$ beam-columns with major axis bending and $p = 0.3$

with the R- models capacities. As shown in Fig. 4.14, the capacity of both R- models shows a non-linear relationship with A_f/A_w under the $p = 0.3$ condition. Similar relationships were observed in the $p = 0.5$ and $p = 0.7$ conditions. Members with a large A_f/A_w are square sections and have a positive correlation with the capacity as a larger A_f/A_w leads to an increase of the area distributed far away from the centroid axis resulting in a higher I_x value, where I_x is moment of inertia about major axis bending. However, members with a small A_f/A_w, which correspond to rectangular sections in this study, resulted in a higher capacity than those with a large A_f/A_w due to smaller maximum residual stresses of rectangular sections for the R-ECCS model. As for the R-Rotarized model, the residual stress pattern for rotary-straightened members was measured for a square section [3]. Thus, residual stresses for rotary-straightened rectangular sections may need to be measured to examine the effects of the aspect ratio as well as A_f/A_w.

Web restraint (d_w/t_f), one of the model inputs of the R- models, has a significant correlation as L/r increases for both R-ECCS and R-Rotarized because a larger d_w results in a larger cross-section moment of inertia, which affects the Euler's buckling load that likely controls at high slenderness. For

$L/r \geqslant 80$, R-Rotarized is more affected by the R- model input parameters (b_f/t_w and d_w/t_f) than R-ECCS when $L/r \geqslant 80$. As rotary-straightened W-sections have a small magnitude of maximum compressive residual stress (c_r^-), it has a longer $\tau = 1.0$ plateau than hot-rolled W-shapes in all of the p conditions (Fig. 4.9a). Therefore, the R-Rotarized members have higher τ values than the R-ECCS members at the initiation of stiffness reduction near $\tau = 1.0$. This reduces the effect of residual stresses and as a result the slender members are more sensitive to the geometric parameters as they carry less applied moment than stocky members.

Minor axis bending

From Fig. 4.13 for the correlation results of minor axis bending, A_f/A_w is shown to have a strong negative correlation for R-ECCS, K-ECCS, and R-Rotarized in the range of $L/r < 100$. The correlation coefficients are slightly higher compared with the correlation coefficients for major axis bending results. This reflects that W-shapes with minor axis bending are more sensitive to the distribution of areas (A_f/A_w), which has previously been referred to as weight [148], [150], compared to major axis bending. Moreover, as a large A_f/A_w leads to a low bending moment capacity due to an increased area distributed far away from the centroidal axis [148], A_f/A_w has a negative correlation with the capacity. The significant observations regarding the comparisons between the four models as illustrated in Fig. 4.13 are provided as follows:

AISC: The AISC model shows weak correlations between the normalized capacity and all of the parameters. The model derived a consistent capacity over the range of p and L/r as previously shown in Fig. 4.10 due to the simple τ equation that neglects the effect of geometry and bending moment. Therefore, AISC has weak correlations across the parameters.

K-ECCS: The aspect ratio b/d is shown to be significant since the ECCS residual stress pattern determines the maximum residual stresses accord-

ing to b/d. Compared with the other models, the parameters have similar correlation values across the L/r and p values because the rectangular and square sections, respectively, had a consistent capacity as shown in Fig 4.10.

R-ECCS and R-Rotarized: The R-ECCS model has b/d as a significant parameter while the R-Rotarized does not since the ECCS [133] residual stress distribution determines residual stress magnitudes based on the aspect ratio. Flange element restraint b_f/t_w has a high impact on the member capacity under the low axial load condition but the impact reduces under higher axial loads. For W-shapes with minor axis bending, initial yielding occurs at the flange tips [141]. This indicates that the effect of flange element characteristics is more influential in low axial load conditions. The web and flange restraints (b_f/t_w and d_w/t_f), which are the modeling parameters of the R- models, have a larger correlation in the R-Rotarized model than in the ECCS model. This is because rotary-straightened sections have small residual stresses at the flange tips, which allows the member to support more load before failure under low axial loads.

4.5 Discussion

Stability analysis of steel structures must account for the effect of residual stresses in members as it affects the overall strength by initializing yielding at lower load levels. For hot-rolled W-shapes, two representative residual stress distributions (Fig. 2.3a and b) have been adopted by AISC 360 [1] and Eurocode 3 [4], respectively. Recently, residual stresses of rotary-straightened W-shapes (Fig. 2.3c) were measured. This section discusses member capacity comparisons using the results provided in Section 4.4. The discussion focuses on the predictions for rotary-straightened sections, which is a prevalent manufacturing practice currently but is not explicitly

considered in the current steel design provisions [1], [4].

As discussed in Section 4.4.1, columns with different residual stress patterns, reflected by the various τ models, had an impact on the capacity. The difference in model outputs was more significant for square cross sections than for rectangular cross sections because the ECCS residual stress pattern [133] reflects the larger maximum compressive residual stresses of square sections. The AISC model showed minimal capacity differences between the axis of bending or cross-section dimensions because the model ignores their contributions in estimating the stiffness reduction factor. The capacities between the stiffness reduction models showed the most significant differences on square columns bending about the minor axis, which indicates the material models that are used to account for the residual stresses on the cross-section have a large influence on the predicted capacities.

According to the beam-column capacity comparisons, as discussed in Section 4.4.2, the application of the residual stress patterns for hot-rolled W-sections was not appropriate for analyzing rotary-straightened beam-columns in several cases. For instance, under higher axial loads, the AISC beam-columns resulted in unconservative predictions relative to the model results representing rotary-straightened members, which may lead to unsafe designs for rotary-straightened beam-columns designed per the AISC provisions. Moreover, the ECCS beam-column predictions showed a high level of conservatism with increasing axial loads relative to the rotary-straightened members (R-Rotarized), which may generate an inefficient and thus costly design. This was more significant in minor axis bending than in major axis bending. To improve the accuracy and efficiency of the analysis of rotary-straightened members as well as hot-rolled members in general, it is recommended to implement an appropriate residual stress distribution to estimate the stiffness reduction.

The lack of correlation between the parameters and the AISC beam-

column capacity was observed in Section 4.4.3. This was due to the simplified equation for the stiffness reduction factor provided by AISC 360 [1]. The other models that incorporated residual stress patterns of ECCS or rotary-straightened W-shapes had different influential factors depending on the values of axial utilization ratio and member slenderness ratio. The modeling parameters of the R- models such as web and flange restraints had a higher correlation in the R-Rotarized model than in the R-ECCS model since rotary-straightened W-shapes have smaller residual stress magnitudes compared with conventional hot-rolled W-shapes with the ECCS residual stress pattern.

This study analyzed the limit load and moment capacity of W-shape members under pure compression and combined compression and bending. The effect of assumed residual stress patterns on the capacity of hot-rolled and rotary-straightened members was examined. Building upon this paper, future research may include frame analyses to investigate the effect of the stiffness reduction models on system behaviors and thus provide more robust guidance for analyzing the stiffness reduction of rotary-straightened sections. The bending axis conditions should be considered in the frame analysis not only because normalized capacity varied depending on the axis of bending but also because the significant parameters for each stiffness reduction model indicated by the correlations between the normalized load and the cross-sectional geometries changed depending on the bending axis.

4.6 Conclusions

A beam element-based parametric study of multiple stiffness reduction models for hot-rolled wide-flange sections was conducted to explore the effect of assumed residual stress distributions on the limit capacity of structural members. Four different stiffness reduction models were investigated:

(1) the current model specified in Chapter C of AISC 360 [1], two models for hot-rolled W-shapes with the ECCS [133] residual stress pattern, which were developed based on (2) the European buckling curves and (3) the relationship of bending moment - axial load - stiffness reduction in a cross-section, and (4) a model for rotary-straightened W-shapes with the residual stress pattern provided by Ge and Yura [3]. Various compact W14 shapes including both square and rectangular cross-sections were employed to examine the effect of multiple cross-sectional parameters on the limit load of columns and beam-columns with a range of slenderness ratios and axial utilization ratios. Columns subjected to axial compression and beam-columns with combined compression and uniaxial bending were analyzed about the major or minor axis of bending.

For columns, it was shown that overall the AISC or ECCS model resulted in lower strength values than the rotary-straightened model. A large capacity difference between the stiffness reduction models occurred in the inelastic buckling range. This difference was larger for columns bending about their minor axis than their major axis. Moreover, square aspect ratio cross sections had a more significant difference between the stiffness reduction models than rectangular aspect sections. The AISC model was found to be uninfluenced by the axis of bending and cross-sectional geometry.

The rotary-straightened model for beam-columns predicts a lower capacity under high axial loads and a higher capacity under low axial loads relative to the AISC model, in particular when the member has a lower slenderness ratio. This indicates that the AISC model results in unconservative load predictions for rotary-straightened beam-columns under high axial loads. The overpredictions by the AISC model also occurred in intermediate axial load levels for beam-columns with minor axis bending. The ECCS models showed conservative predictions compared with the rotary-straightened model for square W-shapes over the range of axial loads, and this was more significant in minor axis bending than major axis

bending. The correlation between the geometric parameters and the capacity of rotary-straightened sections showed a different correlation pattern compared to those for conventional hot-rolled sections due to different residual stress patterns between rotary-straightened and conventional hot-rolled steel sections. Moreover, the lack of correlation between the beam-column capacity and the geometric parameters for the AISC model indicated that the AISC model was not sensitive to the magnitude of geometric parameters for either major nor minor axis bending. The results of this study indicate that updated stiffness reduction models which reflect the true residual stress distribution in rotary straightened sections are required for accurate analysis.

5 EXPLORING MACHINE LEARNING FOR THE STABILITY ANALYSIS OF ROTARY-STRAIGHTENED STEEL MEMBERS WITH MULTIPLE STIFFNESS REDUCTION MODELS

Koh, Hyeyoung, Rosson, Barry T., and Blum, Hannah B. "Exploring machine learning for the stability analysis of rotary-straightened steel members with multiple stiffness reduction models." *Proceedings of the International Colloquium on Stability and Ductility of Steel Structures*, Aveiro, Portugal, September 14-16, 2022.

Abstract

Rotary straightened structural steel cross-sections have a different residual stress pattern compared to those without rotary straightening, which affects structural behavior, especially in members subjected to inelastic buckling. A stiffness reduction material model for rotary-straightened hot rolled sections was previously developed and validated for a specific set of cross-section sizes and load conditions. Previous research has indicated that the current stiffness reduction model specified in Chapter C of AISC 360 for stability design does not accurately capture the stiffness reduction of rotary straightened W-shapes. Particularly, the current stiffness reduction model does not always derive conservative capacity compared with the model for rotary straightened sections. This paper explores machine learning for predicting the beam-column capacity considering different stiffness reduction models and estimating their limit load capacity. Two extreme gradient boosting models were developed for beam-columns under major or minor axis bending. The dataset contained 1,296 finite element simulations for beam-columns with a range of different cross-section ge-

ometries. Excellent prediction accuracy of the developed machine learning models showed the potential of using machine learning for the stability analysis of rotary-straightened members.

5.1 Introduction

Wide flange hot-rolled sections are extensively used in the steel construction industry. Member stability is one of the major design requirements, and Chapter C of AISC 360 [1] applies an inelastic stiffness reduction factor τ to reflect reduced stiffness caused by partial yielding accentuated by residual stresses and spread of plasticity through the cross-section and along the member. It is important to accurately evaluate the effect of residual stress in a structural member because it can lead to the onset of yielding at lower load levels, which results in a reduction of member stiffness thereby affecting the overall member strength. Several residual stress distributions have been established based on experimental data, and different design codes use different assumed residual stress distributions. For example, AISC 360 [1] adopts the Lehigh residual stress pattern which has uniform tensile stress in the web and varies linearly across the flanges (Fig. 2.3a). Eurocode 3 [4] employs the pattern that has linearly varying residual stresses along the flanges and web where the maximum residual stress amplitudes in compression and tension are equal (Fig. 5.1b). The manufacturing process of hot-rolled steel members affects residual stress distributions in a cross-section, and hot-rolled sections with the rotary-straightening process have significantly different residual stress pattern from those without rotary straightening. In general, the straightening process removes or greatly reduces the compressive residual stresses at the flange tips, and the pattern measured by Ge and Yura [3] showed that the sections have alleviated or even eliminated residual stresses at the flange tips (Fig. 5.1c). Since rotary straightening is common practice for

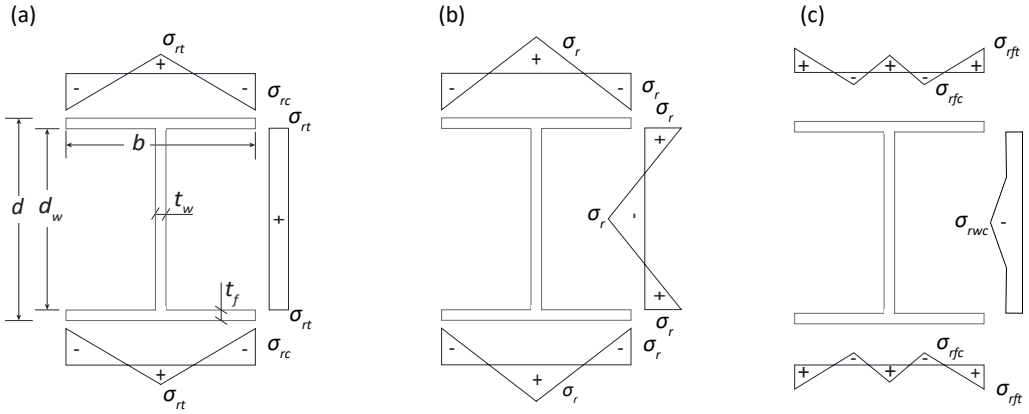

Figure 5.1: Idealized residual stress models (a) Lehigh ([71]) (b) ECCS ([133]) (c) Rotary-straightened hot rolled steel section (Ge and Yura [3])

steel sections in recent years (Ge and Yura [3]), it is necessary to estimate the stiffness reduction based on the current manufacturing method.

Koh et al. [128] conducted a parametric study to assess the current and proposed stiffness reduction models on hot-rolled W-shape members. The stiffness reduction model provided in AISC 360 [1] only considers the axial utilization ratio to estimate the stiffness reduction factor τ. Rosson [143] and Rosson [144] developed two inelastic material models to improve the stiffness reduction prediction by including the effect of bending moment contribution on stiffness reduction. The material models consider the residual stress patterns of ECCS [133] and rotary straightened sections (Ge and Yura [3]), respectively. Finite element limit load analyses on columns and beam-columns were conducted using the different stiffness reduction models. Member slenderness ratios L/r particularly subjected to inelastic buckling were investigated. Based on the beam-column analysis results, it was observed that in some cases the AISC model led to a larger capacity than the other models proposed by Rosson [144] which considered the ECCS residual stress pattern and the rotary-straightened residual stress pattern. The AISC overpredictions may reflect that the AISC stiffness reduction models are not appropriate for rotary straightened W-shapes.

Finite element (FE) analysis has been used to predict the capacity of hot-rolled members and frames with a consideration of different residual stress patterns (Rosson [143], Rosson and Ziemian [147], Rosson [144], Koh et al. [128]), However, if simulations are carried out to predict the capacity of complex structural systems, FE analyses demand advanced software and considerable computational resources, which may be a challenge to implement. Machine learning (ML) techniques have been implemented to predict steel structural responses such as the buckling load of columns [31], [86], [89], ultimate strength of welded tubular joints [88], steel panels [32] and beam-columns [90], [91], and the elastic distortional buckling stress of cold-formed steel members with various cross-sections [87], [94].

This paper explores the applicability of a ML approach for the stability design of steel members. The ML approach could provide accurate predictions comparable with FE analysis with a low computational cost. In this work, ML models are developed to predict the limit load of beam-columns with different stiffness reduction models. Moreover, the predicted capacities were compared to examine if the existing stiffness reduction model is appropriate for rotary-straightened sections. In this paper, the background of three stiffness reduction models is discussed. Second, a database is established, which contains 1,295 FE analysis results of beam-columns considering different residual stress patterns. Third, a procedure to develop machine learning regression models customized for the task of this study is provided. Lastly, the two ML models for beam-columns under major or minor axis bending are evaluated by comparing the capacity obtained from the FE analysis and the predicted capacity from the ML models. High accuracy of the developed ML model showed its potential to estimate the stability analysis of beam-columns when considering different residual stress patterns.

Table 5.1: Stiffness reduction models

Name	Stiffness reduction model	Assumed residual stress pattern	Equations
AISC	AISC 360 [1]	Lehigh [71]	Eq. 5.1
R-ECCS	Rosson [145]	ECCS ([133]	Eqs. 5.2 - 5.9
R-Rotarized	Rosson [144]	Ge and Yura [3]	Eqs. 5.8 - 5.11

5.2 Stiffness reduction models

To estimate the effect of different residual stress patterns on the beam-column capacity, this study considered three stiffness reduction models which incorporates different residual stress patterns (Fig. 5.1) to estimate the stiffness reduction factor τ. The limit load capacities of steel members were evaluated by using the stiffness reduction factor τ values determined according to the stiffness reduction models. The three stiffness reduction models presented in this section are considered in limit load analyses and are shown in Table 5.1.

5.2.1 Chapter C of AISC 360

Chapter C of AISC 360 [1], which provides the design requirements for stability of steel structures, determines the required strengths of components with consideration of stiffness reductions due to the inelastic behavior such as the effect of residual stresses and partial yielding of the cross-section. The residual stress distribution (Galambos and Ketter [71], Fig. 5.1a), which has a 30% of the yield stress as the maximum compressive residual stress σ_{rc} at the flange tips and uniform tension σ_{rt} in the web, is assumed. σ_{rt} is estimated by $\frac{bt_f}{bt_f+t_w d_w}\sigma_{rc}$, which represents $\frac{A_f}{A_f+A_w}\sigma_{rc}$. A factor of 0.8 is applied to all components in the structure to reflect the reduced stiffness. Additionally, for components whose flexural stiffnesses affect the stability of the structure, an additional factor τ_b is applied to reflect reduced flexural stiffnesses. When the axial utilization ratio is less than

or equal to 0.5, τ_b is taken as 1.0, indicating that there is no reduction in flexural stiffness. Otherwise, the additional factor is determined by Eq. 5.1:

$$\tau_b = 4(\alpha\frac{P_r}{P_{ns}})[1 - (\alpha\frac{P_r}{P_{ns}})] \tag{5.1}$$

where α equals 1.0 for the LRFD method and 1.6 for the ASD method, P_r is a required axial compressive strength. P_{ns} is the cross-section compressive strength, which equals the yield strength ($\sigma_y \times A_g$) for compact sections. The stiffness reduction relationship is the same regardless of the axis of bending or the presence of bending moment contributing to the loss of flexural stiffness..

5.2.2 W-shapes with the ECCS residual stress pattern

Rosson [145] developed a stiffness reduction model for compact W-shapes with an ECCS [133] residual stress pattern (Fig. 5.1b), which can consider major axis or minor axis bending. This model will be referred to as "R-ECCS" in the results. As compact doubly-symmetric beam-columns show significantly different behaviors depending on the axis of bending when conducting plastic zone analyses (Attalla et al. [146], Ziemian and McGuire [135]), the developed model can improve the AISC model by capturing the different responses between major and minor axis bending. The stiffness reduction model is developed based on three-dimensional $m - p - \tau$ surface plots generated by a fiber element model for W-shapes, where m is a moment normalized by plastic moment which is defined as M/M_{px} for major axis bending and M/M_{py} for minor axis bending, p is the applied axial load to yield strength ratio P/P_y, and τ is the stiffness reduction factor. The limit of $\tau = 1.0$ is determined when the m and p conditions generate the sum of three compression stresses equal to the yield stress σ_y, where the compression stresses include the residual compression stress σ_r, the bending moment compression stress σ_m, and the

axial compression stress σ_p. The variable p is positive throughout this paper which requires the same sign for P_y and P, where compression is denoted as positive. The maximum moment at which $\tau = 1.0$, denoted $m(\tau = 1.0)$, for major axis bending is given in Eq. 5.2:

$$m(\tau = 1.0) = \frac{S_x}{Z_x}(1 - c_r - p) \tag{5.2}$$

where S_x is major axis elastic section modulus and Z_x is major axis plastic section modulus. Eq. 5.2 is independent of the actual shape of the residual stress pattern because it only considers the maximum residual compression stress in the flange. The ratio of maximum compressive residual stress at the flange tips to yield stress, c_r, is 0.3 in this study. The maximum moment at which $\tau = 1.0$ for minor axis bending is given in Eq. 5.3:

$$m(\tau = 1.0) = \frac{S_y}{Z_y}(1 - c_r - p) \tag{5.3}$$

where S_y is minor axis elastic section modulus and Z_y is minor axis plastic section modulus. Similar to Eq. 5.2, the actual residual stress pattern does not affect Eq. 5.3 as it is based on the flange tip compression stress magnitude. Fig. 5.2 illustrates an example of the $\tau = 1.0$ condition for R-ECCS with major or minor axis bending.

To determine the m condition when $\tau = 0$ (denoted $m(\tau = 0)$) for major axis bending, the required equation is dependent on the plastic neutral axis location in a cross-section. The equation is independent of the shape of the residual stress distribution. Eq. 5.4 is used when the plastic neutral axis is outside the flange, which is the case for W-shapes under low axial compression loads. Eq. 5.5 is used for W-shapes under high values of axial compression, when the plastic neutral axis is inside the flange thickness:

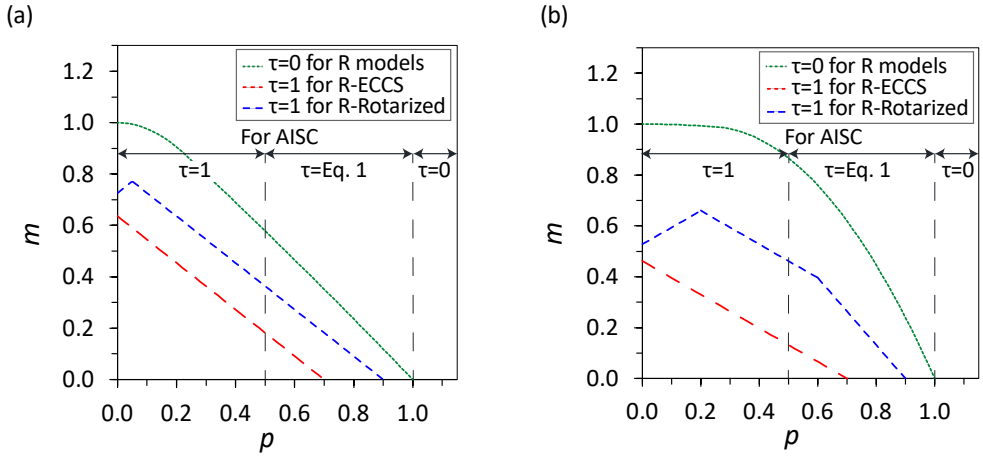

Figure 5.2: $\tau = 1.0$ and $\tau = 0$ perimeter conditions for W12x65 beam-column with (a) major axis bending (b) minor axis bending [128]

$$when\ p < \frac{\lambda}{2+\lambda} \qquad m(\tau = 0) = 1 - \frac{p^2(2+\lambda)^2}{(4\lambda_o + \lambda(4+\lambda)} \tag{5.4}$$

$$when\ p \geqslant \frac{\lambda}{2+\lambda} \qquad m(\tau = 0) = \frac{(2+\lambda_1)^2 - [p(2+\lambda) - \lambda + \lambda_1]^2}{4 + \lambda_1(4+\lambda)} \tag{5.5}$$

where $\lambda = A_w/A_f$ is the ratio of web to flange areas, $\lambda_o = t_w/b_f$ is the ratio of web thickness to flange width, and $\lambda_1 = d_w/t_f$ is the ratio of web depth to flange thickness.

For the minor axis bending condition, Eq. 5.6 is used when the plastic neutral axis is inside the web, which occurs in wide-flange sections under low values of axial load. Eq. 5.7 is used for the sections with high axial loads, which have the plastic neutral axis outside the web thickness:

$$when\ p < \frac{2\lambda_o + \lambda}{2+\lambda} \qquad m(\tau = 0) = 1 - \frac{p^2(2+\lambda)^2}{(2+\lambda\lambda_o)(2+\lambda_1)} \tag{5.6}$$

$$when\ p \geqslant \frac{2\lambda_o + \lambda}{2 + \lambda} \qquad m(\tau = 0) = \frac{4 - [p(2 + \lambda) - \lambda]^2}{2(2 + \lambda\lambda_o)} \tag{5.7}$$

The perimeter condition of uniaxial bending when $\tau = 0$ is illustrated in Fig. 5.2 in addition to the perimeter condition of $\tau = 1$. A τ of 0 indicates that no flexural stiffness remains in the cross-section for the m and p conditions given in Eqs. 5.6 through 5.9. The region below the $\tau = 1.0$ line, inside the triangular region, represents the moment and axial load conditions of no stiffness reduction ($\tau = 1.0$). The stiffness reduction factor τ in the region between $\tau = 1.0$ and $\tau = 0$ curves is provided in Eq. 5.8 and Eq. 5.9. The values for $m(\tau = 1.0)$ and $m(\tau = 0)$ are determined depending on the axis of bending used to estimate τ:

$$when\ p < 1 - c_r \qquad \tau = 1 - \left[\frac{m - m(\tau = 1.0)}{m(\tau = 0) - m(\tau = 1.0)}\right]^n \tag{5.8}$$

$$when\ p \geqslant 1 - c_r \qquad \tau = \left[\frac{1 - p}{c_r}\right]\left[1 - \frac{m}{m(\tau = 0)}\right]^n \tag{5.9}$$

where n is an independent input. This study used n equal to 4 and 2 for major axis bending and minor axis bending, respectively, following Rosson and Ziemian [147], for modeling W-shapes with the ECCS residual stress pattern.

5.2.3 Rotary-straightened W-shapes

Rosson [144] developed a stiffness reduction model for rotary-straightened W-shapes based on the residual stress pattern (Fig. 5.1c) examined by Ge and Yura [3]. In contrast to the ECCS pattern, which has the maximum

compressive residual stresses (σ_{rfc}) at the flange tips, rotary-straightened sections have the maximum residual tensile stresses (σ_{rft}) at the flange tips. This will result in different initial yield load conditions. The maximum compression residual stresses of rotary-straightened sections occur at the quarter-point of the flanges with a reduced magnitude compared to the sections without the rotary-straightening process. The equations for maximum moment $m(\tau = 1.0)$ in Eq. 5.2 and Eq. 5.3 are modified to consider this different residual stress pattern of rotary-straightened W-shapes. The maximum moment when $\tau = 1.0$, denoted $m(\tau = 1.0)$, prior to flange initial tension yield under low axial compression conditions for major axis bending is given in Eq. 5.10:

$$when\ p \leqslant \frac{c_r^+ - c_r^-}{2} \qquad m(\tau = 1.0) = \frac{S_x}{Z_x}(1 - c_r^+ + p) \qquad (5.10)$$

where c_r^+ is the ratio of maximum tensile residual stress σ_{rft} to σ_y and c_r^- is the ratio of maximum compressive residual stress σ_{rfc} to σ_y. This study used $c_r^- = 0.1$ and $c_r^+ = 0.2$ based on the values $\sigma_{rfc} = 5ksi$ (34 MPa) and $\sigma_{rft} = 10$ ksi (69 MPa) estimated by Ge and Yura [3]. Eq. 5.11 is used for the maximum moment prior to flange initial compression yield under medium and high axial compression conditions for major axis bending.

$$when\ \frac{c_r^+ - c_r^-}{2} < p \leqslant 1 - c_r^- \qquad m(\tau = 1.0) = \frac{S_x}{Z_x}(1 - c_r^- - p) \quad (5.11)$$

An example of the maximum m and p conditions without stiffness reduction for rotary-straightened sections with major axis bending is shown as $\tau = 1.0$ of R-Rotarized in Fig. 5.2a. The region below the $\tau = 1.0$ curve indicates that there is no stiffness reduction while the solid curve represents the $\tau = 0$ condition.

For beam-columns under minor axis bending, the maximum moment

prior to initial tension yield under low axial compression conditions is determined by Eq. 5.12. The maximum moment prior to initial compression yield under moderate or high axial compression conditions is determined using Eq. 5.13 or Eq. 5.14, respectively. The m and p conditions when $\tau = 1$, defined in Eq. 5.12 - 5.14, are illustrated in Fig. 5.2b as $\tau = 1.0$ of R-Rotarized.

$$when\ p \leqslant c_r^+ \qquad m(\tau = 1.0) = \frac{S_y}{Z_y}(1 - c_r^+ + p) \tag{5.12}$$

$$when\ c_r^+ < p \leqslant 1 - 2c_r^- + c_r^+ \qquad m(\tau = 1.0) = \frac{S_y}{Z_y}(1 + c_r^+ - p) \tag{5.13}$$

$$when\ 1 - 2c_r^- + c_r^+ < p \leqslant 1 - c_r^- \qquad m(\tau = 1.0) - = \frac{2S_y}{Z_y}(1 - c_r^- - p) \tag{5.14}$$

Using the calculated $m(\tau = 1.0)$, Eqs. 5.8 - 5.9 are used to determine the stiffness reduction τ, where c_r^- is used for c_r in Eq. 5.9. The n values of 1.5 and 1.2 are used for major axis bending and minor axis bending, respectively, following Rosson [144], for modeling rotary-straightened W-shapes.

5.3 Data collection

This study established a database of limit load capacity of wide-flange beam-columns by conducting finite element (FE) analysis. Beam element FE models were created in MASTAN2 [12], and second-order inelastic analyses were conducted. Fig. 5.3 illustrates the FE model for beam-column used in this study. The FE models are restrained from out-of-plane behav-

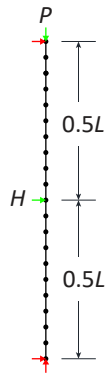

Figure 5.3: Beam-column model

ior. The steel material was defined with a yield stress F_y of 50 ksi (345 MPa) and Young's modulus of 29,000 ksi (200 GPa). Beam-columns were modeled with the member slenderness ratios L/r ranging from 40 to 120 with increments of 20, where L is the member length and r is radius of gyration; r_x or r_y is selected depending on the axis of bending. Member length L was changed to reach a target slenderness ratio. The members were subdivided into twenty elements. An initial geometric imperfection of a half sine wave with a magnitude of $L/1000$ was modeled at the mid-height of members. All of the members in the study were fully compact per AISC Section B4 definition [1]. This study selected the cross-sections that are commonly used in structural design, which ranges from W10 (10 inch, 254 mm nominal depth) to W14 (14 inch, 356 mm nominal depth). Table 5.2 lists the W shapes used in the FE model with their corresponding geometric ratios. The beam-columns were analyzed with combined axial compression and uniaxial bending about the major or minor axis of a member. Axial utilization ratios p including 0.3 (low), 0.5 (intermediate), and 0.7 (high) were considered, where p is the applied axial load to yield strength ratio P/P_y. The axial load P corresponding to $p \times F_y \times A_g$ was first applied to the FE model and then the horizontal load H was incrementally applied until the member reached the limit load.

Table 5.2: Selected W-shapes and cross-sectional properties

Section	b/d	A_f/A_w $(1/\lambda)$	$b_f/2t_f$	d_w/t_w	b_f/t_w $(1/\lambda_0)$	d_w/t_f (λ_1)
W14x48	0.58	1.11	6.75	33.60	23.62	21.19
W14x61	0.72	1.34	7.75	30.40	26.67	19.55
W14X82	0.71	1.36	5.92	22.40	19.80	14.73
W14x109	1.02	1.90	8.49	21.70	27.81	14.63
W14x283	0.96	2.06	3.89	8.84	12.48	6.07
W14x550	0.85	2.09	2.25	4.79	7.23	3.29
W14x605	0.83	2.20	2.09	4.39	6.69	3.02
W14x873	0.80	2.21	1.71	2.89	4.77	2.28
W12x50	0.66	2.56	6.30	26.80	21.84	17.06
W12x72	0.98	3.41	9.00	22.60	27.91	16.36
W12x96	0.96	3.66	6.80	17.70	22.18	12.11
W12x152	0.91	3.69	4.50	11.20	14.37	7.80
W12x230	0.85	3.78	3.10	7.56	10.00	5.29
W12x336	0.80	4.10	2.30	5.47	7.53	3.68
W10x45	0.79	1.60	6.47	22.50	22.91	14.29
W10x60	0.99	1.85	7.41	18.70	24.05	13.00
W10x88	0.95	1.91	5.18	13.00	17.02	8.91
W10x112	0.91	1.93	4.20	10.40	13.77	7.12

The FE simulation results of the beam-columns with the selected W shapes were assembled into a database. Twenty different cross-sections including eight W14 (14 inch, 356 mm nominal depth), six W12 (12 inch, 305 mm nominal depth), and four W10 (10 inch, 254 mm nominal depth) sections were considered with five member slenderness ratios and three axial load ratios. This study selected more W14 sections than the others because they have a wide range of geometric properties according to the standardized sections provided in AISC 360 [1]. In addition, the τ factors derived by the three stiffness reduction models were applied to the same beam-column model, therefore three different responses were obtained on each identical model. The dataset consisted of 1,296 samples for beam-columns under major or minor axis bending, i.e., each axis of bending included 648 samples.

Nine input variables were considered, including the stiffness reduction model, axial utilization ratio p, and seven geometric ratios, which

are known to govern the behavior of W-shapes. To estimate the effect of the stiffness reduction model, the dataset included the stiffness reduction model in the input parameter group. The geometric ratios included member slenderness, L/r; aspect ratio, b/d, which is the ratio of section width to total section depth; the ratio of flange-to-web-area, A_f/A_w, where A_f is the flange area and A_w is the web area; web element slenderness, d_w/t_w; flange element slenderness, $b_f/2t_f$; flange element restraint, b_f/t_w; and web element restraint, d_w/t_f. Table 5.2 provides the geometric ratios of each W-shape considered in this study and Table 5.3 provides the range of input variables. Variables p and L/r were relatively discrete (3 values for p and 5 values for L/r) compared to the other geometric parameters, therefore there is a limited range of data to analyze the variables for ML model development. More data points with various p and L/r values will be needed in future work.

The normalized limit load capacity derived from FE simulations was utilized for an output variable. The limit load capacity was normalized to $H/(F_y Z)$, where Z is plastic section modulus; either Z_x or Z_y depending on the axis of bending, major or minor, respectively. The highest normalized capacity was 1.63, and it occurred in a $L/r = 40$ member with a low axial load subjected to minor axis bending. In some cases, especially when a member has a large slenderness ratio such as 100 or 120, the beam-columns reached the limit load prior to the full application of p, in which the capacity was observed as 0. This situation more frequently occurred in the AISC model than in the other models. Therefore, the output variable ranged from 0 to 1.63.

Fig. 5.4 illustrates the distributions of four geometric parameters relevant to web and flange properties (d_w/t_w, d_w/t_f, $b_f/2t_f$, and b_f/t_w) among nine input features. In addition, the scatter plots for pairwise correlations between the variables show that the geometric ratio parameters have a strong positive correlation, $\rho > 0.99$, when they have the same

Table 5.3: Range of input and output variables

Parameter	Range
Axial utilization ratio, p	0.3, 0.5, 0.7
Member slenderness, L/r	40, 60, 80, 100, 120
Aspect ratio, b/d	0.58 - 1.02
The ratio of flange-to-web-area, A_f/A_w	1.11 - 4.1
Flange element slenderness, $b_f/2t_f$	1.71 - 9.0
Web element slenderness, d_w/t_w $(1/\lambda)$	2.89 - 33.6
Flange element restraint, b_f/t_w $(1/\lambda_0)$	4.77 - 27.91
Web element restraint, d_w/t_f (λ_1)	2.28 - 21.19
Stiffness reduction model	AISC, R-ECCS, R-Rotarized
Limit load capacity	0 - 1.63

numerator (e.g., d_w/t_w and d_w/t_f). This indicates that t_f and t_w of wide flange sections provided in the 15th edition Steel Construction Manual for AISC 360 [1] have a near-perfect correlation. For the other relationships, the parameters have correlation coefficients between 0.90 and 0.94, with a linear relationship until approximately the midpoint range of the parameters. The other input variables including p, L/r, b/d, A_f/A_w, and stiffness reduction model, showed weak correlations with other variables and thus not shown in Fig. 5.4.

5.4 Machine learning model development

Two separate ML models were developed to predict the limit load capacity of beam-columns under major or minor axis bending. This study used extreme gradient boosting (XGBoost [11]), one of the decision tree-based models. A decision tree algorithm builds regression models in the form of a tree-like structure. A decision tree algorithm starts from the root of the tree that contains the whole training set. The root node is further split into sets of decision nodes in which observations are conditionally based. A final prediction is determined by a series of decision rules for how to split the subsets from a root node to a terminal node which is not divided into further nodes. An XGBoost regressor builds a model

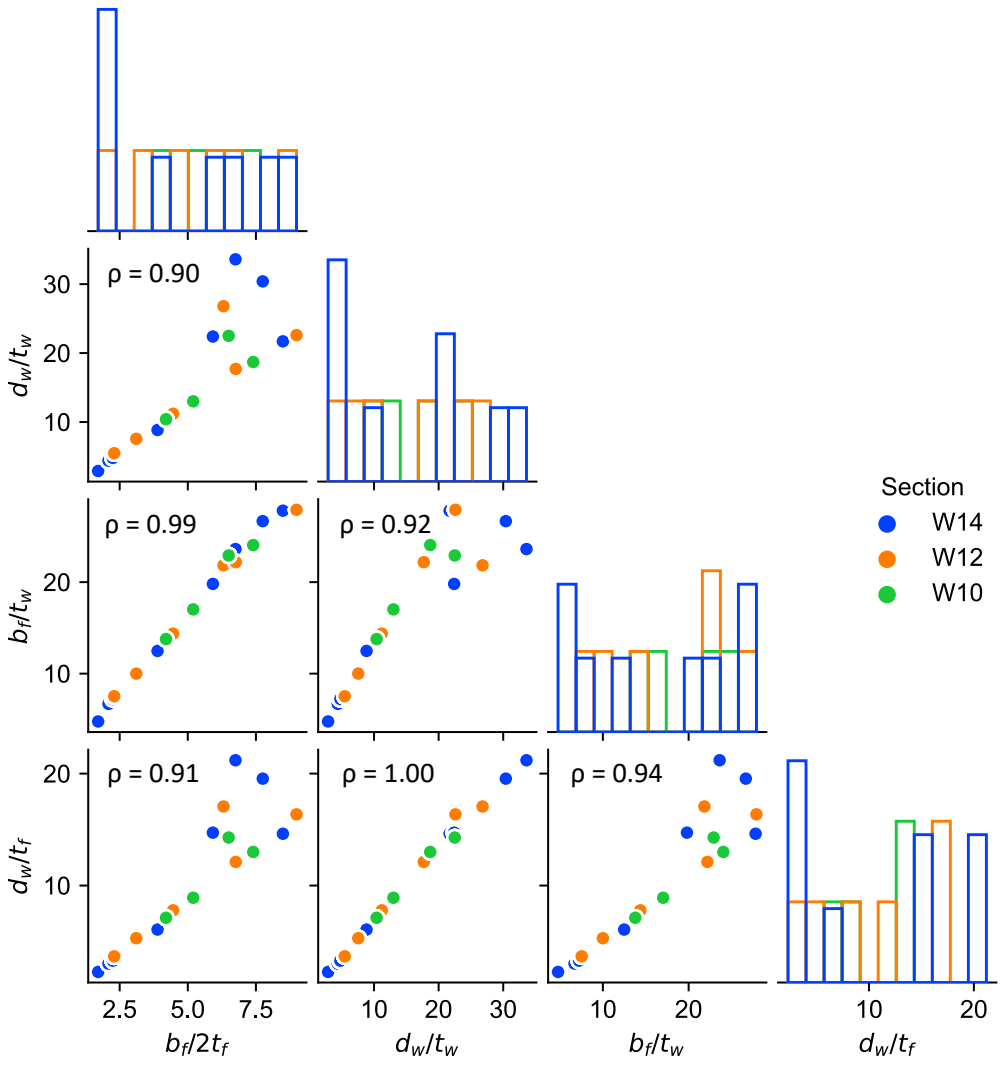

Figure 5.4: Statistical distribution of the geometrical parameters related to flange and web properties and their relationships

consisting of multiple decision trees and implements a gradient boost training approach that improves a single weaker model by combining it with other existing weaker trees to develop a strong prediction model. Thereby, XGBoost offers more accurate and faster predictions than tree algorithms without boosting. XGBoost has been used to predict strength of steel and reinforced concrete structural members and systems ([35], [36], [40], [86])

In this study, the XGBoost algorithm was implemented in Python 3 using the open-source library $scikit-learn$ (Pedregosa et al. [114]). The XGBoost models were trained on 70% of the data and tested on the remaining 30% of the data. The training and test sets were randomly split. A Grid Search Cross-Validation technique was used to find the best hyperparameter of the XGBoost regressor. It runs through all the different parameters that are fed into the parameter grid and produces the best combination of parameters, based on a scoring metric such as a coefficient of determination. Five cross-validations were employed for each selected set of hyperparameters. The parameters required by the XGBoost algorithm are determined by the hyperparameter tuning: the sub-sample ratio of features when constructing each tree was set to 0.6, the maximum depth of a tree was set to 4, the minimum sum of instance weight was set to 5, the learning rate was set to 0.3, and gamma was set to 0. Additionally, this study limited overfitting by conducting early stopping when there was no improvement observed during ML model training. Overfitting refers to a modeling error that occurs when a model is too exactly fit to a training set, thus the model may not perform well with the new data (test data). Early stopping works by monitoring the model performance on a test set and stopping the training procedure once the performance on the test set has not improved after a fixed number of training iterations.

5.5 Machine learning results

After training the ML model, the test set were used to assess the model performance. The predictive performance was evaluated by estimating the evaluation metrics including coefficient of determination (R^2) and root mean square error (RMSE). The R^2 value represents how well the proposed function can predict the experimental data. The RMSE score quantifies how spread out the prediction errors are, i.e., how concentrated the data is around the line of best fit. The equations of the metrics are:

$$R^2 = 1 - \frac{\sum_1^m (y_i - y_{pi})^2}{\sum_1^m \left(y_i - \frac{1}{m}\sum_1^m y_i\right)^2} \tag{5.15}$$

$$\text{RMSE} = \sqrt{\frac{1}{m}\sum_{m=1}^{m} (y_i - y_{pi})^2} \tag{5.16}$$

where m is the total number of test data, y_i is the test value, which is the limit load derived from the FE analysis in this study, y_{pi} = the predicted capacity by machine learning models.

When dividing the data into training and test sets, random shuffling of data is necessary to reduce bias in prediction. To reproduce the training and test sets the same every time it is run, $random\_state$ is used. If $random\_state$ is not used for splitting data, a different set of training and test sets will be derived every time the split is created. This study applied different random states on the same ML model to examine if consistent performance is obtained regardless of random splitting of data. Fig. 5.5 shows the RMSE and R^2 values obtained from different $random\_state$ numbers. As discussed in Section 5.3, input variables p and L/r are discrete and the sample size of the dataset is not large enough to obtain reliable results from training. Thus, the model performance is inconsistent as the training and testing sets have different assigned data points according to different random splits, For example, the RMSE value measured based on

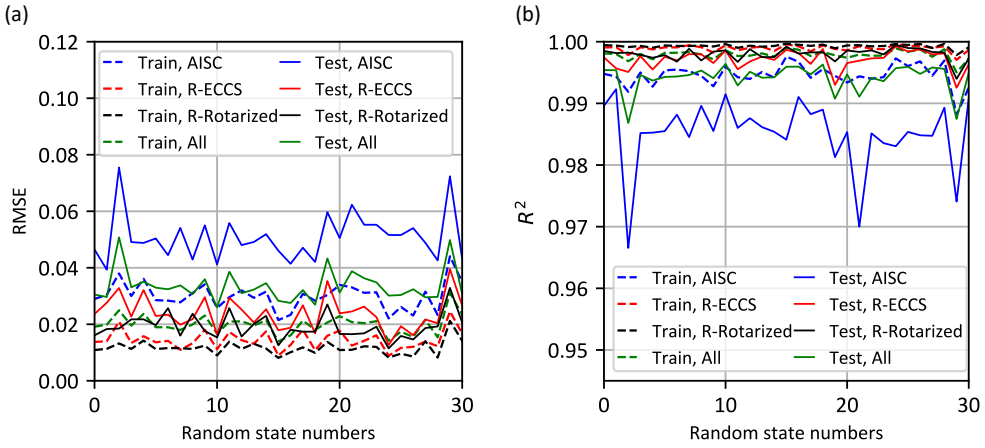

Figure 5.5: Predictive performance depending on different random state (a) RMSE (b) R^2

the entire test set fluctuates within the range of 0.028 and 0.05 even though the performance was assessed on XGBoost with the same hyperparameters. To examine the performance of each stiffness reduction model, samples were divided into the three stiffness reduction models, and then the both metrics were calculated. R-ECCS and R-Rotarized showed similar RMSE and R^2 values over the range of random states. The AISC model showed the lowest performance among the stiffness reduction models. This might be because AISC had relatively consistent capacities between different W-sections (Koh et al. [128]). The AISC model does not account for the cross-section geometry and bending moment contributions to stiffness reduction, which resulted in reduced variation in capacity compared with the other two stiffness reduction models.

Fig. 5.6 presents comparisons of the limit load capacity predicted by the developed XGBoost algorithms and the actual capacity derived by FE analyses. The random splits that showed the best and worst performances observed in Fig. 5.5 are presented. The coefficient of determination is provided for the performance of each stiffness reduction model. Comparing the ML model performance using the best (Fig. 5.6a) and the worst

(Fig. 5.6b) splits for major axis bending, AISC showed a difference of 0.022 in R^2 scores while the other stiffness reduction models had negligible differences (less than 0.004). For minor axis bending, the performance of the ML model with the best random split (Fig. 5.6c) is similar to the major axis bending result (Fig. 5.6a), but the worst case (Fig. 5.6d) showed less accurate performance compared with major axis bending (Fig. 5.6b). When using the best case of a random split (Fig. 5.6a and c), all of the stiffness reduction models showed that most data points are distributed close to the 1:1 line, where the predicted capacity and the tested value are equal, with the R^2 scores greater than 0.989. This demonstrates that the developed XGBoost model can predict the limit load for beam-columns with varying residual stress patterns.

In addition to the performance indicators including R^2 and RMSE, which evaluate the performance of the entire stiffness reduction model, the mean value is calculated to compare the beam-column capacity derived by different stiffness reduction models under specific axial utilization ratios and member slendernesses. Table 5.4 and 5.5 summarize the mean capacity of beam-column with major axis bending and minor axis bending, respectively. The actual and predicted capacities were categorized by L/r and p amplitudes. The predicted results and FE results showed similar relationships between the three different stiffness reduction models. According to the FE analyses, there were some cases where the AISC model showed over-predictions compared with the R- models. For example, as shown in the actual capacity for major axis bending in Table 5.4, when $L/r = 40$, the AISC model led to lower capacity compared with the other models under low axial load, $p = 0.3$. However, as p increased, AISC had a higher capacity than the other models. Moreover, when $L/r = 80$ or 100, the higher capacity predictions of AISC compared to the R- models occurred in the low p condition. For minor axis bending, as given in Table 5.5, AISC had a higher capacity for $L/r = 40$ members under $p =$

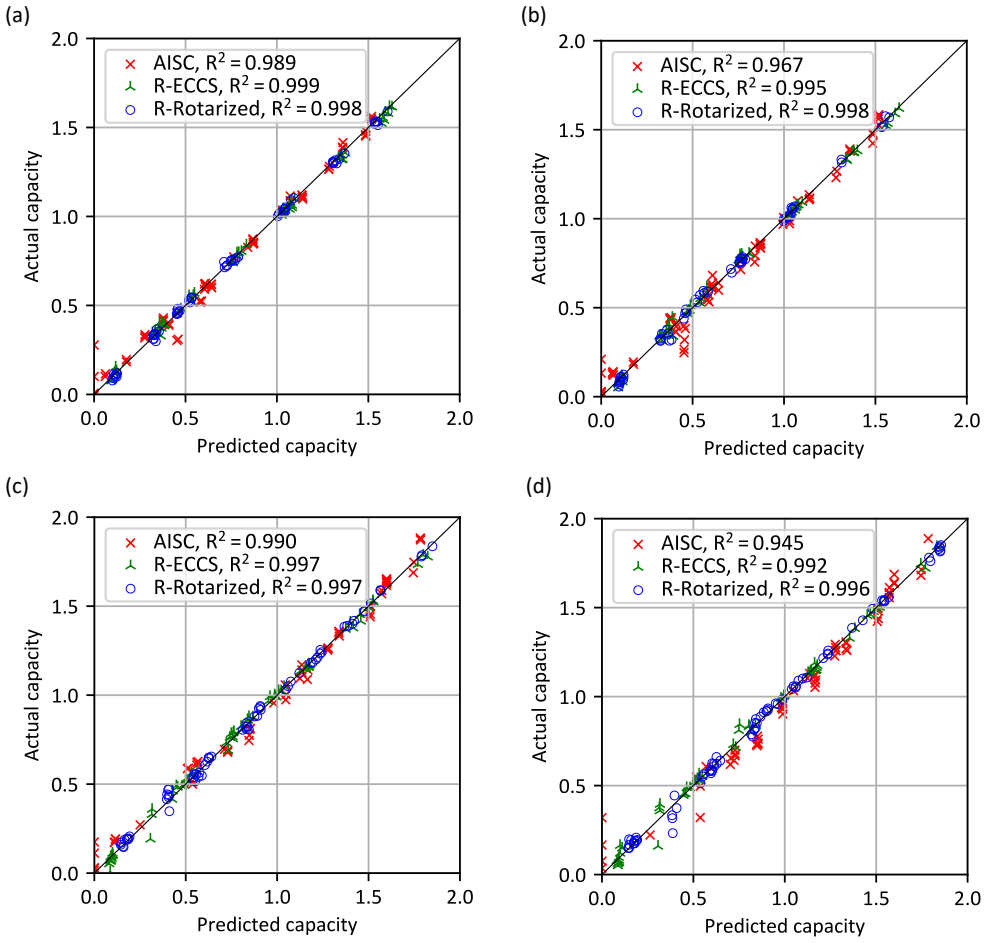

Figure 5.6: Comparisons between predicted and actual capacities (a) best random split for major axis bending (b) worst random split for major axis bending (c) best random split for minor axis bending (b) worst random split for minor axis bending

Table 5.4: Mean capacity of beam-columns under major axis bending

		Actual capacity			Predicted capacity		
L/r	p	AISC	R-ECCS	R-Rotarized	AISC	R-ECCS	R-Rotarized
40	0.3	1.51	1.58	1.56	1.54	1.56	1.55
	0.5	1.06	1.04	1.01	1.07	1.03	1.01
	0.7	0.63	0.53	0.54	0.57	0.55	0.56
60	0.3	1.32	1.35	1.33	1.33	1.34	1.32
	0.5	0.84	0.79	0.80	0.83	0.80	0.77
	0.7	0.34	0.34	0.33	0.35	0.34	0.33
80	0.3	1.12	1.09	1.05	1.09	1.10	1.05
	0.5	0.45	0.48	0.47	0.47	0.49	0.47
	0.7	0.02	0.10	0.10	0.06	0.08	0.09
100	0.3	0.84	0.77	0.73	0.81	0.79	0.73
	0.5	0.04	0.12	0.11	0.08	0.13	0.10
120	0.3	0.45	0.37	0.37	0.39	0.39	0.39

0.5 and 0.7 compared with the other models, with a larger gap than for major axis bending results. As shown in Fig. 5.7 and previously discussed in Section 5.2, AISC applies the same value of the stiffness reduction factor when $p = 0.3$ and $p = 0.5$. However, ECCS and R-Rotarized models consider the bending moment contribution to estimate the stiffness reduction (τ) where τ rapidly decreases as p and m increase. Furthermore, the R-Rotarized stiffness reduction model is based on measured residual stress distributions for rotary straightened members (Ge and Yura [3], therefore the R-Rotarized model is considered the most accurate tau model for rotary straightened members between the three modeling options. In cases where the AISC capacity prediction is higher than the R-Rotarized prediction, the AISC provisions may be considered unconservative.

To further examine the prediction of each stiffness reduction model, Fig. 5.8 is provided, which compares individual data points for members with L/r =40 and 60. The predictions were derived from the ML model with the best performing random split. Each plot includes the three axial load cases of $p = 0.3$, 0.5, and 0.7. The results of R-ECCS had negligible

Table 5.5: Mean capacity of beam-columns under minor axis bending

		Actual capacity			Predicted capacity		
L/r	p	AISC	R-ECCS	R-Rotarized	AISC	R-ECCS	R-Rotarized
40	0.3	1.76	1.8	1.83	1.8	1.78	1.82
	0.5	1.54	1.41	1.45	1.52	1.4	1.45
	0.7	1.11	0.86	0.91	1.07	0.87	0.92
60	0.3	1.55	1.51	1.55	1.54	1.48	1.55
	0.5	1.23	0.98	1.08	1.22	0.98	1.08
	0.7	0.62	0.45	0.56	0.64	0.46	0.56
80	0.3	1.31	1.16	1.22	1.29	1.15	1.22
	0.5	0.66	0.53	0.63	0.69	0.57	0.64
	0.7	0.04	0.08	0.18	0.06	0.06	0.18
100	0.3	0.99	0.74	0.83	0.94	0.79	0.82
	0.5	0.06	0.1	0.15	0.11	0.07	0.14
120	0.3	0.53	0.32	0.4	0.48	0.33	0.42

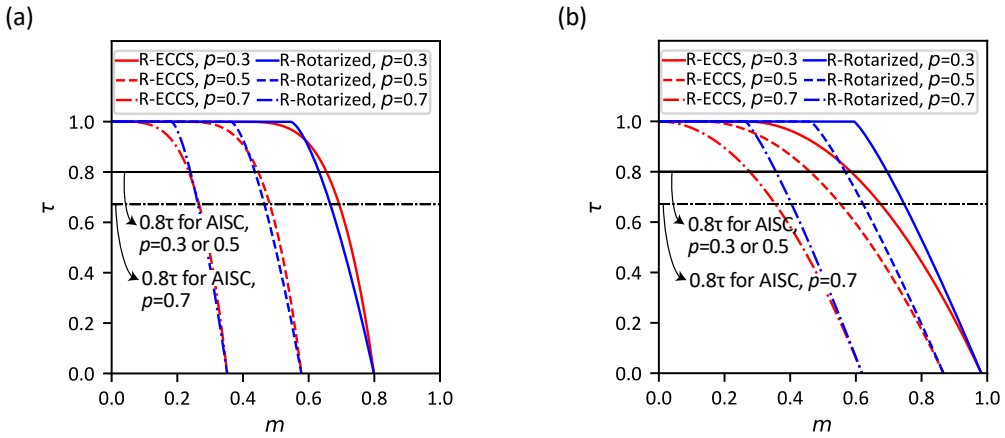

Figure 5.7: τ - m relationships when p $= 0.3$, p $= 0.5$, and p $= 0.7$ with major axis bending (Koh et al. [128])

differences from the R-Rotarized results (Fig. 5.6), therefore R-ECCS is omitted from the figure. Since the test set is randomly selected from the dataset, samples for AISC and R-Rotarized were not obtained from the same members.

As shown in Fig. 5.8, comparisons between predicted and actual capacities of R-Rotarized show close alignment over the investigated axial loads. However, the AISC model had some errors between the predicted and actual capacities despite its high predictive performance, which was $R^2 \approx 0.99$ (Fig. 5.6a and c). When comparing the AISC model predicted and actual data points, there is overall a larger discrepancy for minor axis bending results than for major axis bending results. This indicates that the developed ML model could be used to determine the capacity of beam-columns subjected to major axis bending, but future model development is needed for accurate prediction for minor axis bending. Increasing the sample size will help to improve the predictive performance and generalize the ML model applicability.

Overall for minor axis bending (Fig. 5.8b and d), both predicted and actual capacities for the R-Rotarized model were lower than the predicted and actual capacities for the AISC model. As the R-Rotarized model reflects the actual residual stress present in rotary straightened members, the AISC stiffness reduction model may be overestimating the capacities of rotary straightened members subjected to minor axis bending. The difference in capacities for the AISC model and the R-Rotarized model are reduced for beam-columns subjected to major axis bending.

5.6 Conclusions

Extreme gradient boosting models were developed to predict the limit load capacity of beam-columns considering three different stiffness reduction models, including the current stiffness reduction (τ) model specified in

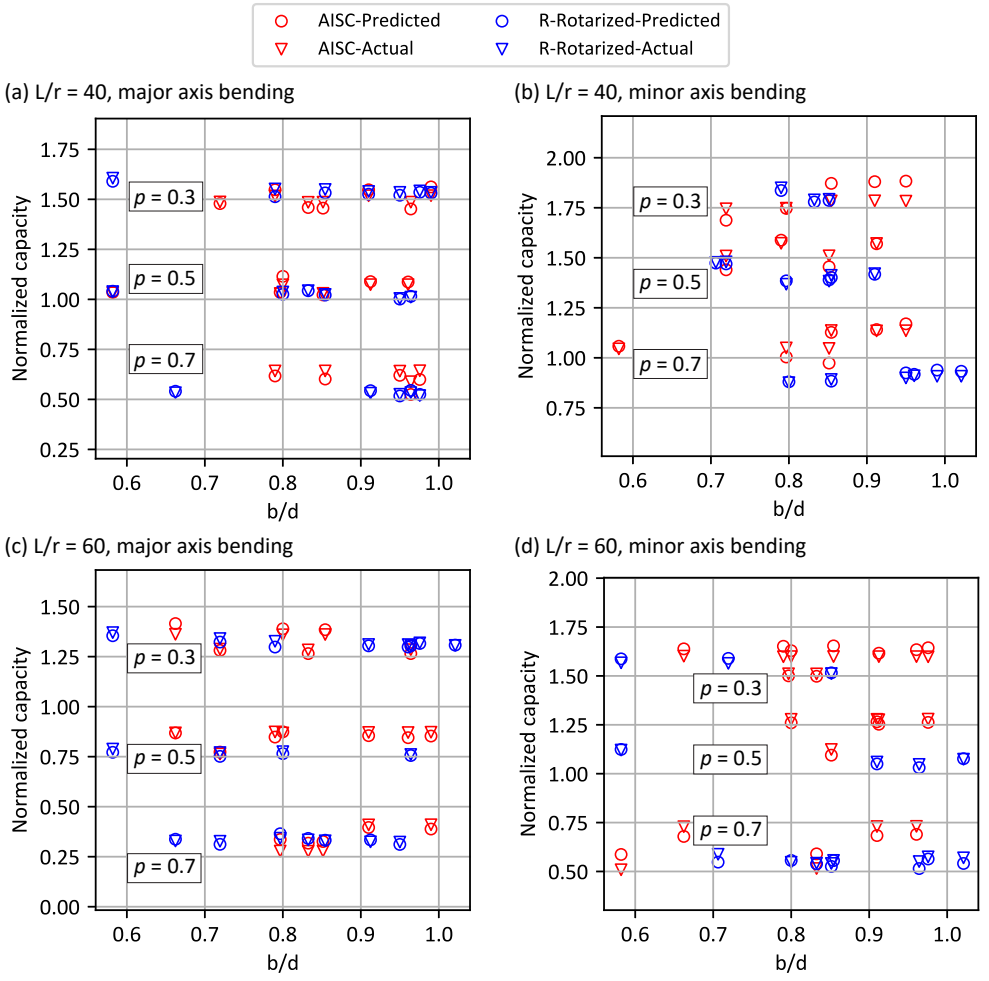

Figure 5.8: Comparison of the FE results and ML predictions for the AISC and R-Rotarized models

AISC 360 [1], a model for hot-rolled wide-flange sections with the ECCS [133] residual stress distribution, and a model for rotary-straightened hot-rolled W-shapes with the residual stress distribution measured by Ge and Yura [3]. The database for machine learning model development was established based on beam finite element (FE) analysis results. A range of compact W shapes was investigated, from W10 (10 inch, 254 mm nominal depth) to W14 (14 inch, 356 mm nominal depth), which are commonly used in structural steel construction. The beam-column FE models were investigated with uniaxial bending about the major and minor axes with multiple axial utilization ratios. Input variables included the stiffness reduction model, member slenderness, axial load ratio, and cross-sectional geometric parameters. The limit load capacity derived from the FE analysis was considered an output variable.

Due to the relatively small dataset and discrete variables such as member slenderness and axial utilization ratio, machine learning model performance was inconsistent depending on how the data was randomly split into training and test sets. The performance evaluated by R^2 scores ranged between 0.987 (worst) and 0.996 (best). The overall predictive performance can be improved by increasing the sample size in future work. The performance of the three individual stiffness reduction models was not identical. AISC showed the lowest accuracy with the R^2 score of 0.989 while the rotary-straightened model achieved 0.998 for the best performing random split. Although the AISC accuracy was high, overall there were larger predictive errors for members subjected to minor axis bending. The proposed machine learning model considering rotary-straightened members showed good predictive performance over the investigated member slendernesses and axial load ratios for both major and minor axes. This demonstrated the potential of using machine learning for the stability analysis of rotary-straightened members. In general, the AISC stiffness reduction model capacity results were higher than the capacity results

of the rotary-straightened stiffness reduction model, which indicates that the appropriate residual stress and stiffness reduction model should be considered for accurate analysis of rotary-straightened members.

6 CALIBRATION AND VALIDATION OF THE HOLE-DRILLING METHOD TO DETERMINE RESIDUAL STRESSES IN ADVANCED HIGH-STRENGTH COLD-FORMED STEEL MEMBERS

Koh, Hyeyoung and Blum, Hannah B. (2022). "Calibration and validation of the hole-drilling method to determine residual stresses in advanced high-strength cold-formed steel members." *Proceedings of the Cold-Formed Steel Research Consortium Colloquium*, Oct 17-19, 2022.

Abstract

Advanced high-strength steel (AHSS) has a unique microstructure which enables unprecedented combinations of strength and ductility. Quantification of residual stresses in AHSS sections is important to translate this newer material to the construction industry. Residual stresses are induced as a result of the cold-forming process where the distribution and magnitude of residual stresses affect the strength and stability behavior of structural members. One method to measure residual stresses is the hole-drilling method, which is a semi-destructive method where the change of strain is measured locally before and after a small hole is drilled. ASTM E837 recommends equations to calculate residual stress using calibration constants, which are derived from the assumption that the material is linear elastic over the range of residual stress magnitudes. However, AHSS materials have a significantly rounded stress-strain curve compared to conventional steel. Moreover, for a thin workpiece, through-hole drilling can be used to measure residual stresses, which assumes uniform membrane stresses through the thickness of a specimen without flexural residual stresses. Currently there is a lack of existing studies to

confirm if the suggested calibration constants are appropriate for AHSS members.

A series of hole-drilling measurements to determine residual stresses in press-braked AHSS lipped angle members was conducted according to ASTM E837. A lipped angle was formed from a sheet of 1.8-mm thick dual-phase steel with a nominal yield stress of 580 MPa and a nominal ultimate strength of 980 MPa. Outer surface strains near the cross-section corners and on the flat regions along the sheet longitudinal and transverse directions were measured by electrical strain gauge rosettes. The distribution of residual stresses obtained from the hole-drilling method was compared with the residual stress measured by the sectioning method of identical AHSS angles. Recommendations for the use of the hole-drilling method and appropriate calibration constants to determine residual stress measurements in AHSS members is presented.

6.1 Introduction

Recently, advanced high-strength steel (AHSS) has been developed, which enables lightweight design with improved ductility at a sufficiently high strength level. AHSS has been adopted by the automotive industry. In order to bring AHSS to the steel construction industry, it is necessary to quantify material properties including residual stresses and cross-sectional behaviors. It is important to accurately evaluate the effect of residual stress in a structural member because it can lead to the onset of yielding at lower load levels, which results in a reduction of member stiffness thereby affecting the overall member strength. The residual stress distribution in a cross section generally depends on material properties, cross-sectional geometry, and formation processes. Residual stresses in cold-formed steel (CFS) sections are mainly induced by the cold-bending effect during the manufacturing process. Experimental studies have quantified the residual stress

of conventional CFS members [151]–[154], whereas the investigations of residual stresses in high-strength CFS members are limited.

Residual stress measurement techniques can be categorized as either destructive or non-destructive. Non-destructive methods include X-rays, synchrotron and neutron diffraction, and magnetic and ultrasonic methods. These methods are advantageous in techniques with being non-destructive but they are limited to a small number of facilities. Destructive methods, also called relaxation methods, involve measuring deformations caused by the release of residual stresses upon removal of stressed material. Sectioning is a principal destructive method that has been widely adopted to measure residual stresses in structural CFS members [123], [152], [155], [156]. The hole-drilling method, also called a semi-destructive method, assesses residual stresses by removing localized stress and measuring relieved strains in the adjacent material around a drilled hole. Stresses before and after drilling a hole are compared to determine stress relaxation due to the hole drilling. Hole-drilling is more simple and less destructive than sectioning. As a drilled hole is sufficiently small compared with the specimen size, its presence does not noticeably damage specimen performance. Previous research compared residual stress distributions of cold-formed and hot-rolled steel members by using various residual stress measurement techniques including sectioning, hole-drilling, and X-ray diffraction [157]–[159]. It was reported that the different techniques showed good agreement in residual stress measurement results but the hole-drilling method showed larger residual stress fluctuations in a cross section compared with the other techniques.

ASTM E837 (2020) provides the standard for the hole-drilling method used for residual stress measurements. The standard assumes a material has a linear stress-strain curve, and the practical limit of residual stresses for using hole-drilling is 50% of the material yield stress. The hole-drilling method drills a small hole in a specimen to measure the change of strain

where localized deformations have been created around the hole. Therefore, this method results in a stress concentration around the drilled hole, whereby the local stresses may reach yield resulting in plastic relaxed strain around the hole. This indicates that the elastic assumption for residual stress measurements may cause overestimation if the plasticity of a material is ignored particularly for large residual stresses, which are near-yield stresses [161], [162]. To correct this error, the plastic behavior of material should be considered in estimating residual stresses when using the hole-drilling method [161], [162].

The hole-drilling method incorporates two calibration coefficients into the equations to calculate residual stresses. The coefficients represent the relieved strains due to unit stresses within the hole depth. Appropriate calibration constants should be used because they affect the accuracy of the method. Finite element approaches have been adopted for calibration of the coefficients with the benefits of simplifying the complexity and difficulty of calibrating them [160], [163]–[165]. Recently, experimental calibrations have been conducted to determine the coefficients for structural steel considering the effect of the material plasticity [158], [166] because the given calibration constants by the standard were derived based on the assumption of the elasticity of materials. As AHSS has shown a rounded stress-strain curve, this study conducts calibration experiments to determine the coefficients of the material and thus improve the accuracy of the hole-drilling method.

The objectives of this paper are (1) to estimate the calibration constants for the AHSS material to accurately measure residual stresses by the hole-drilling method and (2) to quantify residual stress distributions of lipped angle CFS members manufactured from AHSS sheet with a thickness of 1.8 mm. Detailed procedures for performing the hole-drilling method are provided, including specimen preparation, strain gauge rosette installation, experimental calibration, test setup for hole-drilling, and residual stress

measurement. As for the calibration experiment, this study accounts for plastic strain of the material by calibrating coefficients at four different levels, which are 33.3%, 50%, 66.7%, and 100% of the material yield stress. The residual stress distribution estimated by the hole-drilling method is provided and compared with residual stresses of the identical cross section measured by the sectioning method. Finally, recommendations for the use of appropriate calibration constants and performing the hole-drilling method to determine residual stresses in AHSS members are presented.

6.2 Experimental Program

6.2.1 Material Properties

The test specimen was fabricated from dual phase (DP) steel sheets with a nominal yield stress of 580 MPa and nominal ultimate strength of 980 MPa. Figure 6.1 illustrates the stress-strain curve of the material used in this study, which shows a rounded stress-strain curve with significant strain hardening. This is significantly different from that of structural carbon steel which has a clear linear elastic region, yield plateau, and minor strain hardening. This study considered the 0.2% offset yield stress as material yield stress due to the lack of a precisely defined yield point. The material yield stress in longitudinal and transverse directions was taken as 629.2 MPa and 640.5MPa, respectively. Young's moduli for longitudinal and transverse directions were 193.3 GPa and 205.9 GPa, respectively.

6.2.2 Specimen fabrication and preparation

A press-braked lipped angle member with a length of 533.4 mm was cut into seven equal pieces of 76.2 mm as shown in Figure 6.2a. A vertical band saw designed for steel cutting was utilized to cut the member. Four cross sections labeled #2, #3, #5, and #6 were tested for residual stress

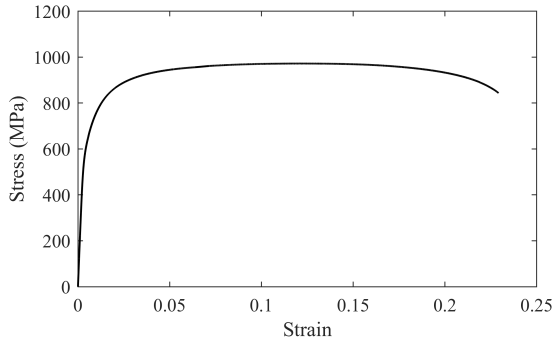

Figure 6.1: Longitudinal stress-strain curve

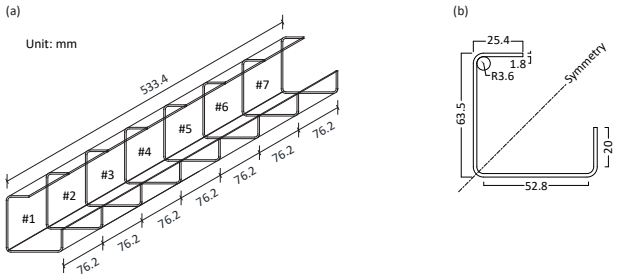

Figure 6.2: (a) Lipped angle member (b) Cross-section geometry (Unit: mm)

measurements by hole-drilling. Figure 6.2b provides the dimensions of the cross section, which is 63.5 mm (width) $\times$ 63.5 mm (height) $\times$ 1.8 mm (thickness) with the radii of curvature at the inner corner of 3.6 mm.

The hole-drilling method uses strain gauge rosettes to evaluate residual stresses by measuring near-surface stresses of a material. Figure 6.3 illustrates the schematic diagram of the strain gauge rosette employed in this study. An appropriate strain gauge rosette was selected based on the dimension of the cross section following ASTM E837 [160]. The strain gauge rosette contains three radial strain gauges (grids) in a format of 0° - 90° - 225° to measure three in-plane relieved strain components, which are used to estimate three residual stress components including normal stresses in x and y directions and shear stress. Gauge grids 1 and 3 are

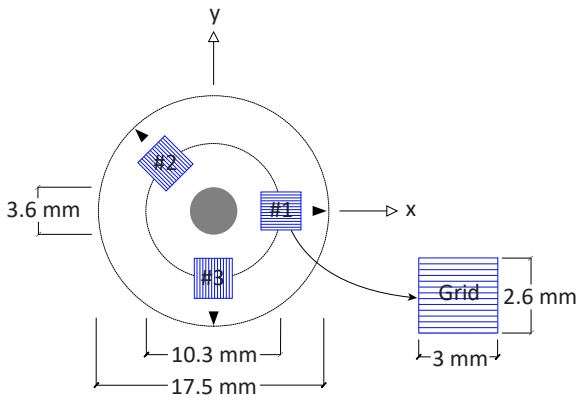

Figure 6.3: Schematic diagram of strain gauge rosette

oriented in x and y directions, respectively. The standardized strain gauge rosettes FRS-3-11 manufactured by Tokyo Measuring Instruments Lab were used, with a gauge circle diameter of 10.3 mm, a backing diameter of 17.5 mm, and a grid of 2.6 mm $\times$ 3 mm.

Eight strain gauge rosettes were installed on the outer surface of the cross section as shown in Figure 6.4a. Each angle leg contained three desired hole positions, and each lip had a single hole position. The drilled hole diameter of 3.6 mm was designed to be twice the thickness [167]. Grid 1 of the strain gauge rosette was aligned to the longitudinal direction, which corresponds to the x-axis in Figure 6.3. The hole-drilling method only permits strain gauge rosette installation on flat regions because drilling a flat-bottomed hole into a curved surface causes difficulty in selecting the hole datum depth. Thereby, the corner regions were not tested but rather the flat regions adjacent to the corners. The distance between adjacent holes was set to 31 mm, which satisfies the limit of the safe distance between adjacent holes [167] of 2.4 times the gauge diameter (10.3 mm), which is 24.7 mm for this study. It was confirmed that the hole positions are far enough from each other as well as the edge of the cross section that the holes do not influence the stress equilibrium of each other [160], [168]. The preparation procedure of the specimen for

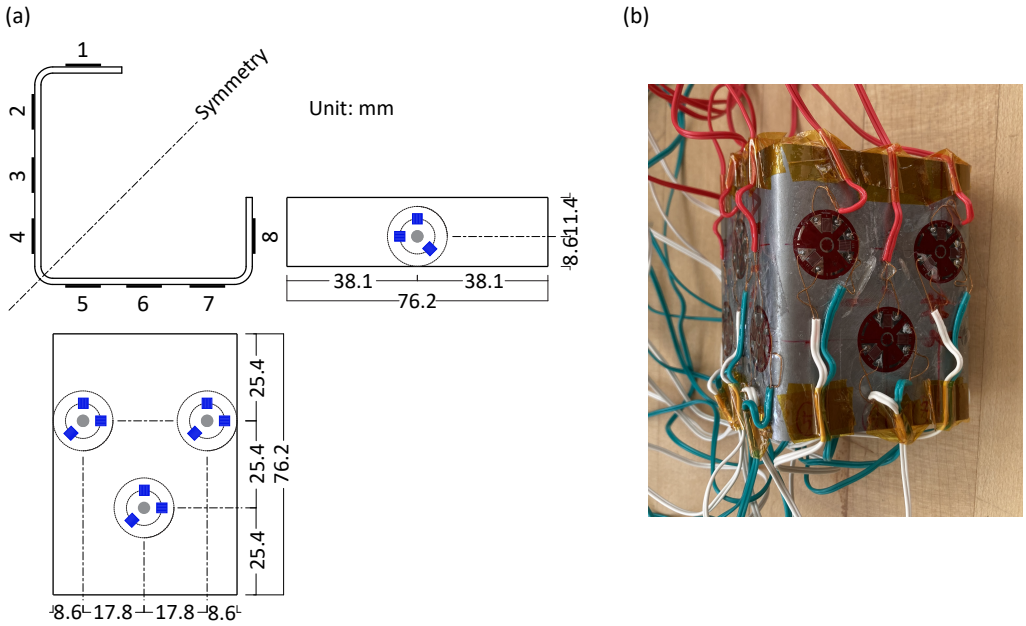

Figure 6.4: (a) Distribution of gauge rosettes (b) Prepared specimen (Unit: mm)

residual stress measurements is as follows: Desired locations for holes were marked on the outer surface of the specimen. Surfaces around the desired hole positions were polished and degreased by acetone solvent. Finally, the strain gauge rosettes were attached by glue to the outer surface by aligning the center of the strain gauge rosettes and the desired hole positions.

6.2.3 Hole-drilling test

As recommended by ASTM E837 [160], through-thickness measurements were adopted in lieu of blind-hole drilling because the specimen is classified as a thin workpiece. Thus through-holes were drilled at the geometric center of strain gauge rosettes. Strains before and after drilling a through-hole were recorded by the gauge rosettes, including the three in-plane stress components with 0°, 90°, and 225° in the xy-plane. The measured strain components were then substituted into Equations 6.1 and 6.2 to

calculate the released residual stresses by hole-drilling.

$$\sigma_x = -E\frac{B(\epsilon_x + \epsilon_y) + A(\epsilon_x - \epsilon_y)}{4AB} \tag{6.1}$$

$$\sigma_y = -E\frac{B(\epsilon_x + \epsilon_y) - A(\epsilon_x - \epsilon_y)}{4AB} \tag{6.2}$$

where σ_x is the longitudinal residual stress, σ_y is the transverse residual stress, E is the material Young's modulus, and A and B are the calibration constants

The authors developed the hole-drilling workstation as shown in Figure 6.5a by following the concept of a typical hole-drilling apparatus [160], [167]. The workstation consists of aluminum body frames, an electric hand drill accompanying with a 3.6 mm diameter Titanium-Nitride coated cobalt steel drill bit, and a vertical adjustment to lower the drill. The speed of the drill was 25,000 rpm, which satisfies the minimum speed of 20,000 rpm [160]. The hand drill was fixed to the frame by connecting clamp halves and welded angles with bolts. The lipped angles were placed on a support beneath the dill and aligned to coincide the centers of strain gauge rosettes with the drill bit. Multiple clamps were used to fix both the specimen and the specimen support to the workstation.

6.2.4 Experimental Calibration

ASTM E837 [160] provides tables for the calibration coefficients A and B given by hole depths, hole diameters, and types of rosettes. These constants were induced by numerical analyses with the elastic assumption of materials. However, the hole-drilling method can produce plastic strain due to the stress concentration around a drilled hole. If the materials behave nonlinearly even under low strains, the residual stress would be overestimated [162]. Since AHSS showed the rounded stress-strain curve as shown in Figure 6.1, the effect of the presence of inelastic behavior in this

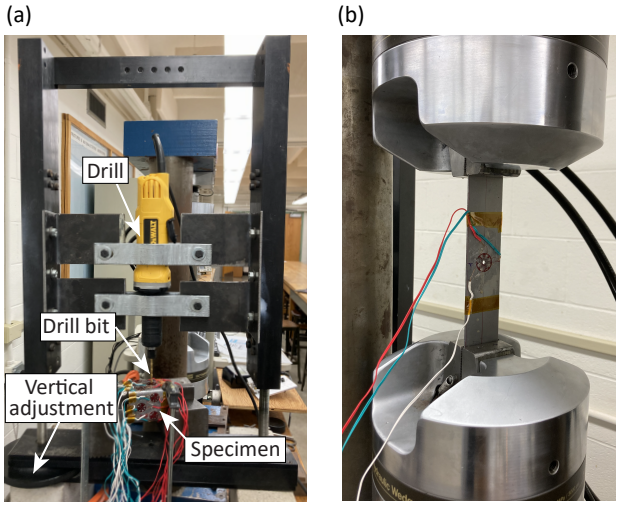

Figure 6.5: (a) Hole-drilling workstation developed by the authors (b) Tensile test for the calibration experiment

material should be calibrated. This study thus performed experimental calibration to determine the calibration constants A and B of the AHSS material.

The calibration experiment procedure is as follows: (1) A calibration specimen (Figure 6.6) is first mounted on a tensile machine. (2) Before hole-drilling, a small uniaxial tensile calibration load, P_c, is applied to develop the desired uniform calibration stress σ_c which is much less than the material yield stress. The values of measured strain due to the applied load at Grid 1, $\epsilon_1^{'}$, and Grid 3, $\epsilon_3^{'}$, are recorded. (3) The tensile loading is released and the calibration specimen is removed from the tensile machine. (4) A through-hole is drilled at the center of the strain gauge rosette. (5) The calibration specimen is again mounted to the tensile machine. (6) The same calibration loading P_c is re-applied. (7) Finally, the corresponding Grid 1 and Grid 3 strains, $\epsilon_1^{''}$ and $\epsilon_3^{''}$, are recorded. The calibration constants under the strains corresponding to the desired stress load σ_c can be calculated by Equations 6.3 and 6.4:

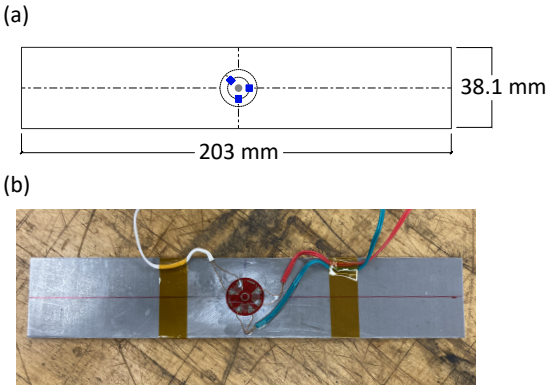

Figure 6.6: (a) Calibration sheet (b) Prepared calibration sheet

$$A = \frac{E(\epsilon_1 + \epsilon_3)}{2\sigma} \tag{6.3}$$

$$B = \frac{E(\epsilon_1 - \epsilon_3)}{2\sigma} \tag{6.4}$$

where $\epsilon_1 = \epsilon_1'' - \epsilon_1'$, $\epsilon_3 = \epsilon_3'' - \epsilon_1'$, and σ is the corresponding tensile stress applied to the calibration sheet.

The experimental calibration was carried out on a calibration sheet cut out from the same DP steel sheet as used for the lipped angle. As shown in Figure 6.6, the calibration sheet was designed to take 38.1 mm (height) $\times$ 203 mm (length), which is deeper than ten times the hole diameter, 36 mm, and longer than five times the width, 185 mm, as recommended to minimize edge and end effects [168]. A single strain gauge rosette was attached at the center of the calibration sheet. The strain gauge rosette was oriented to align Grid 1 to longitudinal (parallel) to the tensile loading direction and Grid 3 to the transverse direction. Figure 6.5b shows the calibration sheet mounted after drilling a hole.

The hole-drilling method assumes material linearity to calculate residual stresses. Literature [161], [169] and the standard [160] provide the applicable limits of the method in terms of the percentage of yield stress, which vary between 50% and 65% of yield stress. To estimate the calibra-

tion constants in the inelastic range in addition to the elastic range, this study calibrated the constants at four different levels of residual stresses including 33.3%, 50%, 66.7%, and 100% of yield stress, which can be considered the calibration loading P_c in Equations 6.3 and 6.4. Four calibration sheets were prepared per calibration test, and two sets of calibration test were performed. Four sets of longitudinal and transverse relived strains before and after hole-drilling were obtained from each calibration test. The strain sets (ϵ_1 and ϵ_3) were substituted into Equations 6.3 and 6.4 to determine the calibration constants at the corresponding level of residual stress.

Table 6.1: Calibration constants

Calibration stress		Range of application		Calibration constants					
				Test 1		Test 2		Average	
P_c (MPa)	% of σ_y	σ_r (MPa)	% of σ_y	A	B	A	B	A	B
210	33.3	σ_r <315	0 - 50	-0.1120	-0.4025	—	—	-0.1120	-0.4025
315	50	315 <σ_r <367.5	50 - 58.4	—	—	-0.1208	-0.4391	-0.1208	-0.4391
420	66.7	367.5 <σ_r <525	58.4 - 83.4	-0.1384	-0.4541	-0.1494	-0.4494	-0.1439	-0.4518
630	100	525<σ_r < 630	83.4 - 100	—	—	-0.1583	-0.4892	-0.1583	-0.4892

6.3 Experimental Results

6.3.1 Calibration experiment

To ensure the accuracy of residual stress measurements of hole drilling, a direct experimental calibration was carried out to determine the calibration constants A and B of the AHSS material. Table 6.1 summarizes the calibration experiment results including the four different levels of applied calibration stresses, applicable ranges, and the corresponding constants A and B calculated by Equations 6.3 and 6.4, in which σ_r is residual stress and σ_y is the 0.2% offset yield stress. In some cases, sparks appeared around holes during drilling because of invisible gaps between the specimen and the fixity. Moreover, due to the lack of a depth gauge in the hole-drilling workstation, drilling did not go through the entire thickness in some cases therefore blind holes were attained. For the cases where sparks or blind holes were observed, it was not possible to accurately measure appropriate residual strain values, and thus they are presented as blanks (—) in Table 6.1.

The averaged values from the two calibration test sets were considered the calibration constants in this study. The elastic range, 0% - 50% of the yield stress, showed the smallest absolute values among the four ranges. The constants have the largest absolute values in the range of 83.4% and 100% of the yield stress. This indicates that if the elastic calibration constants are employed in Equations 6.1 and 6.2 to estimate residual stresses higher than 50% of the yield stress, the residual stresses would be overpredicted.

In addition to the measured calibration constants, ASTM E837 [160] provide the calibration constant values derived from numerical analyses, which can be used to estimate residual stresses less than 50% of the material yield stress. Appropriate constants should be selected based on the rosette types, hole depths, and hole diameters. The corresponding A and B

values for the hole of a 3.6 mm diameter and 1.8 mm depth, which were used in this study, are -0.1231 and -0.3855, respectively. Comparing the standard constants and the directly measured constants for the elastic range given in Table 6.1, A and B have percentage differences of 9.4% and 4.3%, respectively. As this study provided the calibration constants for the full range of yield stress, they can be used for future studies for residual stress measurements of the same AHSS material.

6.3.2 Residual stress measurements

Tables 6.2 and 6.3 summarize the measured residual stress values in longitudinal and transverse directions for four angle sections including #2, #3, #5, and #6 and their averaged values. The averaged residual stresses were divided by the 0.2% offset yield stress of 629.2 MPa to present them in terms of % of the material yield stress. Released longitudinal and transverse strains at each hole position were recorded at least thirty seconds after drilling a hole, in order to give time to the region around the hole to cooling after drilling to prevent any influence of thermal strains. Equations 6.1 and 6.2 were used to estimate the residual stresses. Since all of the calculated residual stresses were less than 10% of the material yield stress, the calibration constants A and B for the 0% - 50% range given in Table 6.1 were utilized, which were -0.1120 and -0.4025, respectively. Similar to the calibration experiment, technical issues such as sparks and blind holes occurred during the residual stress measurement test. The hole positions that had those issues are shown as blanks (—) in Tables 6.2 and 6.3.

As summarized in Table 6.2, longitudinal residual stresses were positive which indicates tensile residual stresses. The near-corner regions in the legs (Hole positions 2,4,5, and 7 in Figure 6.4) showed larger residual stresses than flat regions (Hole positions 3 and 6). Hole position 7 contained the largest longitudinal residual stress in the cross section with the value of 8.0% of the yield stress. The lips (Hole positions 1 and 8)

Table 6.2: Measured longitudinal residual stresses (Unit: MPa)

Hole position	Section #2	#3	#5	#6	Avg	% of yield
1	9.3	26.9	31.8	11.5	19.9	3.2%
2	—	37.6	—	34.1	35.8	5.7%
3	35.6	—	27.2	29.8	30.9	4.9%
4	29.3	—	34.6	—	31.9	5.1%
5	33.0	—	—	40.0	36.5	5.8%
6	37.2	—	30.7	29.9	32.6	5.2%
7	—	—	56.3	44.4	50.3	8.0%
8	16.0	—	—	22.0	19.0	3.0%

Table 6.3: Measured transverse residual stresses (Unit: MPa)

Hole position	Section #2	#3	#5	#6	Avg	% of yield
1	-8.5	0.8	5.5	-5.9	-2.0	-0.3%
2	—	5.0	—	-5.6	-0.3	0.0%
3	3.8	—	-7.9	2.6	-0.5	-0.1%
4	3.0	—	10.7	—	6.8	1.1%
5	4.4	—	—	7.4	5.9	0.9%
6	5.1	—	-3.3	-8.7	-2.3	-0.4%
7	—	—	17.6	-1.0	8.3	1.3%
8	-4.6	—	—	-13.0	-8.8	-1.4%

measured 3.2% and 3.0% of the yield stress, which were lower residual stresses compared with the legs. The hole position of 8 showed the smallest residual stress with the value of 3.0% of the yield stress.

According to Table 6.3, transverse residual stress components showed both positive and negative values across the cross section. However, the magnitudes were significantly small, which showed the percentages of yield stress less than 1.5% over the eight hole positions. This indicates that transverse residual stresses in the AHSS lipped angle cold-formed members would not be expected to have a significant influence on structural behavior.

6.4 Discussion

Residual stress measurements on the identical cross sections were performed with the sectioning method by the author's research team. Sectioning measured the sections labeled #1 and #4 in Figure 6.2a. Figure 6.7 compares the longitudinal residual stress distributions estimated by the hole-drilling and sectioning methods. The hole-drilling results included the averaged residual stresses from the four cross sections (#2, #3, #5, and #6), and the sectioning results used the averaged values from the two cross sections (#1 and #4). Hole-drilling and sectioning measured residual stresses at different positions in the cross section because the hole-drilling method recommends installing strain gauge rosettes on flat regions rather than curved surfaces. The hole-drilling method used eight strain gauge rosettes on the outer surface of the flat regions only, whereas the sectioning test attached nine linear strain gauges on both flat and corner regions on both outer and inner surfaces as indicated in Figure 6.7. As through-hole measurements assume uniform stresses through the thickness of the workpiece [160] and the strain gauge rosettes were attached to the outer surface, the outer surface components of the sectioning results were compared with the hole-drilling residual stresses.

Comparing the outer surface residual stress distribution (red) of sectioning and the hole-drilling results (black) shown in Figure 6.7, the hole-drilling method measured larger residual stresses in the legs than the sectioning method. Wang et al. [158] also observed larger residual stresses by the hole-drilling method compared with the sectioning method. As the hole-drilling method incorporates the effect of stress concentration around the drilled hole, it could lead to increased measured residual stresses. Both methods showed larger residual stresses in the near-corner regions compared with the flat regions. The vertical leg (Hole positions 2 - 4) showed a good agreement between the two methods with minimal differences while the horizontal leg (Hole positions 5 - 7) showed relatively large

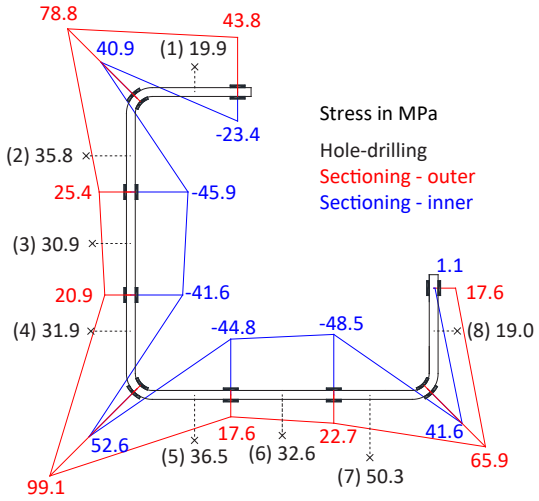

Figure 6.7: Longitudinal residual stress distributions measured by hole-drilling and sectioning reported in [170]

differences. As for the residual stresses at the lips (Hole positions 1 and 8), the hole-drilling results showed similar values between the two measuring positions, which are 19.9 MPa and 19.0 MPa, respectively, whereas the outer surface components of sectioning showed a large percentage difference of 59.8% between the two positions at the lip edges. This led to a good agreement between the two methods for hole position 8 and a significant difference for hole position 1. It should be noted that the tested cross sections are symmetric about the diagonal. The comparisons demonstrated that the hole-drilling method obtained comparable results against the sectioning method for measuring residual stresses of the AHSS lipped angles.

6.5 Conclusions

The residual stress measurements of lipped angles press-braked from 3.6 mm-thick advanced high-strength steel (AHSS) sheets by the hole-drilling method were presented in this paper. The standard for hole-

drilling, ASTM E837 [160], limits its applicability to residual stresses up to 50% of the yield stress because they assume a linear elastic material to calculate residual stresses. To reflect the rounded stress-strain curve of AHSS and hence improve the accuracy of the hole-drilling method for this new material, experimental calibration was conducted to determine the hole-drilling calibration coefficients for AHSS.

The calibration coefficients were determined for four different levels of residual stresses to consider the plasticity of the material. The elastic range, 0% - 50 % of the material yield stress, showed smaller calibration coefficients than the ranges greater than 50% of yield stress. This indicates that if the effect of plasticity is ignored for estimating residual stresses higher than 50% of the yield stress, the residual stresses can be overestimated. The calibration constants provided in this paper could be used to measure residual stresses of different types of members fabricated from the same AHSS material.

Positive longitudinal residual stresses were observed over the entire cross section. The longitudinal residual stresses ranged between 3.0% and 8.0% of yield stress. In the legs, the hole positions near corners showed larger residual stresses than the holes on flat regions. The near-corner region in the leg showed the largest residual stress in the cross section while the lip showed the smallest residual stress. Transverse residual stresses values were negligible over the cross section, which ranged between -1.4% and 0.9% of the yield stress. The residual stress distribution derived by the hole-drilling method was compared with the distribution measured by the sectioning method. The presented residual stress distributions showed similar results, such as large residual stresses in the corner regions and small residual stresses in the flat regions including both the legs and lips. The comparisons demonstrated that the hole-drilling results are comparable with the sectioning results.

7 A REVIEW OF CURRENT PRACTICE FOR TESTING BY ANALYSIS OF COLD-FORMED STEEL STRUCTURES

Koh, Hyeyoung and Blum, Hannah B. (2022). "A review of current practice for testing by analysis of cold-formed steel structures." *Structures*, 245: 871-880. https://doi.org/10.1016/j.istruc.2022.01.017

Abstract

New product development is crucial to advance innovation in the cold-formed steel structural industry. Design of cold-formed steel structures usually requires physical testing, but it may be challenging to control the complexity and uncertainty inherent in physical experiments. The physical testing of new components and assemblies is often a cost barrier that prevents implementation and delays new product development. Testing by analysis has recently been recognized as a desirable area to pursue by the cold-formed steel structural industry due to the benefit of providing an efficient test environment. Not only does testing by analysis limit the high expense of physical experiments needed to quantify the behavior and safety of new members, connections, and structures, but it also reduces the time from product inception to development. Two considerations are necessary to ensure accurate results from testing by analysis. First, it requires a rational engineering analysis to calculate the capacities and deformations of the member or system, and the requirements to produce accurate analyses must be explicitly stated. Second, it is necessary to understand if the software used is capable of correctly modeling the behavior of thin-walled and nonsymmetric structural members and systems. Although the computational capability for structural design has been developed in recent years, there lacks a standardized approach to testing by analysis, especially for cold-formed steel design. This review aims to evaluate exist-

ing design standards that include the numerical test-based design for both cold-formed steel and other structural engineering industries. Recommendations for the use of testing by analysis based on the design standards and recent research related to numerical modeling are presented. The results of this study will assist with accurate and efficient design using testing by analysis.

7.1 Introduction

Virtual testing, also called testing by analysis is beneficial in the initial design phase of new products. Finite element (FE) analysis can be used to virtually test multiple designs before moving to the fabrication or physical experiment. It is important to determine the capacities of new shapes being developed, but also to understand how the various elements in the cross section move and interact. A new product is often designed for a specific use or span, but it is necessary to understand how the new product will behave in other less common loading and structural scenarios. Virtual testing can be a good alternative to physical testing since it allows researchers and engineers to reduce the expense and time in performing physical experiments. In order to perform virtual testing, a rational engineering judgment is required to determine the capacities of the structures. Although the use of testing by analysis has been increasing and computational capability for modeling has been developed in recent years, most structural design standards do not have detailed requirements for design by analysis.

This paper reviews the cold-formed steel design standards including Chapter C and K of AISI S100-16 [5] which provide requirements for the design for stability and test-based design, Chapter 5 and 9 of Eurocode 3 (EN 1993-1-3) [171] to cover provisions for structural analysis and design by testing, and Appendix B of the Australia / New Zealand standard

AS/NZS 4600 [6] that contains provisions for the structural analysis. The discussed structural steel standards for hot-rolled members include Chapter C and Appendix 1 of AISC 360-16 [1] that contain requirements for the design for stability and structural analysis by advanced methods, Chapter 5 of Eurocode 3 (EN 1993-1-1) [4] to describe modeling for structural analysis, Chapter 4 and Appendix D of Australia / New Zealand standard AS/NZS 4100 [10] which provide the requirements for the methods of structural analysis and advanced analysis, and Chapter 8 and Annex O of the Canadian standard CSA S16 [7] to cover structural analysis including advanced analysis. The discussed structural concrete standard includes Chapter 6 of ACI 318 [172]. Furthermore, EN 1993-1-3 states "*For a approach with FE-methods (or others) see EN 1993-1-5, Annex C*", therefore Eurocode 3 Part 1-5: Plated Structural Elements [173] is included. Plated structural elements can be applicable to cold-formed steel members in addition to hot-rolled steel members such as plate girders or slender I-beams. It was explored if timber design standards including AITC [174], ANSI/AWC [175], and ANSI/TPI [176] have design by analysis rules, but no specific requirements for virtual testing were found.

The aim of this study is to provide an overview of virtual testing or testing by analysis in existing cold-formed steel design standards, structural steel and concrete design standards, and recent research in order to determine which test-based design procedures should be implemented when performing virtual testing. Recommendations for virtual testing based on current design standards and research are presented, with the categories of material, modeling of cross section, element type and size, geometric imperfection and residual stress, second-order effects, connections, the effect of holes, uncertainty, benchmark test, dimension, superposition principle, and documentation of results. In addition to the recommendations, recent papers that performed FE modeling of cold-formed steel (CFS) members are introduced as good examples of virtual testing.

7.2 Recommendations

In this section, the recommendations for testing by analysis that can be implemented for the design of cold-formed steel (CFS) members and systems are provided based on the requirements and suggestions provided in existing design standards in addition to research that provides further information and supports the recommendations. The recommendations are categorized according to the factors to consider when performing testing by analysis.

7.2.1 Material

Numerical modeling requires a correct representation of the material stress-strain relationship in order to obtain an accurate prediction of structural responses by considering the material stiffness and effects due to yielding and plasticity. The standards for CFS design, EN 1993-1-3 [171] and AS/NZS 4600 [6], allow the use of nonlinear material stress-strain relationships for advanced analysis. Annex C.6 of EN 1993-1-5 [173] specifies that material properties should be taken as characteristic values and four types of material behavior may be used as illustrated in Fig. 7.1: elastic-plastic without strain hardening, elastic-plastic with a nominal plateau slope, elastic-plastic with linear strain hardening, and true stress-strain curve modified from the test results. True stress and strain are approximated by $\sigma_{true} = \sigma(1 + \epsilon)$ and $\epsilon_{true} = \ln(1 + \epsilon)$, respectively, where σ is stress and ϵ is strain. In addition to these material behaviors, recognized material models for CFS can be adopted according to AS/NZS 4600 and AS 4084 [6], [177].

Gardner and Yun (2018) [178] developed an accurate stress-strain model of CFS described by the two-stage Ramberg-Osgood model [179]. Predictive expressions to model the stress-strain curve were developed based on 700 experimental stress-strain curves, covering a wide range of

steel grades, thicknesses, and cross section types. The material behavior of CFS can be achieved provided that the values of the key model parameters are given, such as the factors related to first and second strain hardening, ultimate strain, ultimate tensile strength, and yield strength at the cross section corners. The 0.2% proof stress measured from experimental stress-strain responses is taken as the material yield strength. The accuracy of the proposed model and predictive parameters is demonstrated even if only the value of the yield strength is known. As such, this model can be considered appropriate for use in design by advanced computational analysis.

The corner regions of CFS cross-sections contain a significantly higher yield strength than the flat regions due to large plastic deformations resulting from the cold bending process. Rossi et al. [180] proposed a power law model for predicting the strength enhancement in the corner regions, which determines the enhanced yield strength by the model parameters calibrated through the 0.2% proof stress and ultimate tensile stress. Gardner and Yun [178] compared the existing three models [5], [180], [181] for predicting strength enhancements, and the Rossi et al. [180] model showed the highest accuracy with the simplified expression.

For the material modeling of CFS utilized in design by analysis, it is recommended to consider the nonlinear stress-strain relationships to capture the inelastic behavior of structural components or structures. The authors recommend using the Ramberg-Osgood model proposed by Gardner and Yun [178], which is a straight-forward approach to accurately model cold-formed steel materials, and using the Rossi et al. model [180] for modeling the corner regions of cold-formed steel sections.

7.2.2 Modeling of cross section

The cross section properties must be correctly accounted for as they affect the analysis of structural members and systems, especially for nonsym-

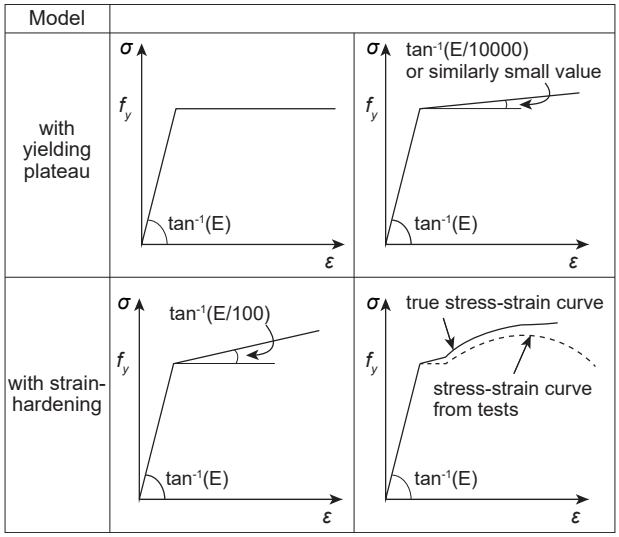

Figure 7.1: Modeling of material behavior from EN 1993-1-5 [173]

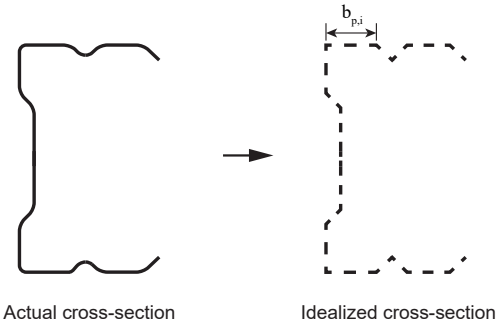

Figure 7.2: Approximate allowance for rounded corners from EN 1993-1-3 [171]

metric cross sections. Section 5.1 of EN 1993-1-3 [171] has provisions for considering the effect of rounded corners when determining section properties. If the internal radius $r \leqslant 5t$ and $r \leqslant 0.1b_p$, the rounded corners may be neglected and instead the cross section can be assumed to consist of sharp corners as shown in Fig. 7.2, where b_p is the notional flat widths measured from the midpoints of the adjacent corner elements, and t is the thickness of the element. When computing cross section stiffness properties, the effect of rounded corners should always be considered.

Liu et al. [182] investigated an improvement on an existing beam-

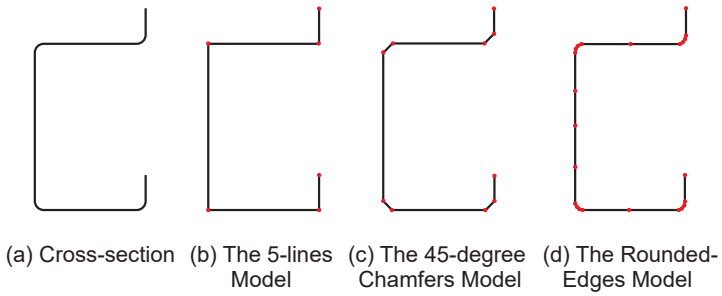

Figure 7.3: Three cross section models from Liu et al. [182]

column line element formulations for accurately simulating the axial buckling behavior of arbitrarily-shaped open-sections. One of the asymmetric sections studied was a lipped-C shape consisting of one lip that is turned outward and one inward (Fig. 7.3a). To study the effects of the rounded corners on the section properties, three different modeling methods to consider the corners were created as shown in Fig. 7.3b-d. The three cross section models are established based on line-elements with (1) neglecting the rounded corners, thereby 90-degree at the corners, (2) considering the rounded corners as 45-degree line-elements, and (3) full consideration of the rounded corners with three elements in a corner. The module MSA_Sect within MASTAN2 [183] was used to compute the section properties. The section properties generated by CUFSM [184] using the rounded-edges model were employed as the benchmark solution. As shown in Table 7.1 which displays the results from Liu et al.'s study, the cross section properties from the rounded edges model were almost identical to the cross section properties determined from the rounded corner model in CUFSM [184], which is the expected results. The important comparison is between the sharp corner model and the 45-degree corner chamfer model. The sharp corner model resulted in several cross section properties with greater than 5% percent error compared to the benchmark properties, whereas the 45-degree chamfers model had less than 4% percent difference for all section properties.

Table 7.1: Section properties of asymmetric cross section from Liu et al. [182]

	Percent difference (%) with the benchmark solution		
Parameters	5-lines	45-degree chamfers	rounded-edges
A	3.04	-1.01	0.00
I_y	5.84	-2.23	0.00
I_z	3.55	-1.42	0.00
J	2.95	-1.27	0.00
C_w (I_w)	8.05	-3.67	-0.15
y_c	-6.01	3.08	0.00
z_c	0.65	-0.48	0.00

Note: A is the cross-section area, I_y and I_z are the second moment of areas about the principal axes, J is the uniform torsional rigidity, C_w (I_w) the uniform torsion warping constant, y_c and z_c are the coordinates of shear center

Section 5.2 of EN 1993-1-3 [171] specifies the range of element width-to-thickness ratios that can be used without additional requirements for structural analysis. These limits represent the ranges that have sufficient experience and verification by testing. Cross sections outside the range of the width-to-thickness ratios may be used when their resistance at ultimate limit states and behavior at serviceability limit states are verified by physical testing and/or by analysis (calculations) with an appropriate number of tests, however, the appropriate number is not stated in the standard.

For the modeling of cross section components, EN 1993-1-3 [171] suggests to follow Annex C of EN 1993-1-5 [173] or to use approximate modeling of junctions and contribution of stiffeners where the restraining effect of the adjacent plates is simulated by elastic springs at intermediate stiffeners and edge stiffeners; i.e., the rotational and translational springs are used to simulate the stiffening effect of adjacent plates or stiffeners. However, there is no guidance on how to determine the numerical value of the springs. For modeling corners, it is recommended considering the effects of rounded corners to determine accurate cross section properties. This can be done using CUFSM [184] for the greatest accuracy, or with 45-

Table 7.2: Assumptions for FE methods from EN 1993-1-5 [173]

Material behavior	Geometric behavior	Imperfections	Example of use
Linear	Nonlinear	No	Critical plate buckling load
Linear	Nonlinear	Yes	Elastic plate buckling resistance
Nonlinear	Nonlinear	Yes	Elastic-plastic resistance in ultimate limit state

degree corner chamfers for a minor reduction in accuracy. The boundary conditions for supports, interfaces, and applied loads should be modeled so that obtained results are conservative [173].

7.2.3 Element type and size

The choice of finite element (FE) type (e.g. shell or solid) and the size of mesh determine the accuracy of the analysis results. Chapter 6 of ACI 318 [172] requires the use of an element type that obtains the response required for the task and the mesh size capable of determining the full structural response in detail. Section 3 of AS 4084 [177] suggests to use shell finite elements or finite strips for the modeling of storage racks. According to Annex C.1 of EN 1993-1-5 [173], as shown in Table 7.2, the choice of FE analysis types depends on the assumptions of linearity or nonlinearity of material and geometric behaviors, and the presence of imperfections. Validation sensitivity checks with successive refinement may be performed.

Shell elements should be utilized when the width-to-thickness ratio of elements is greater than 1.7 and solid elements should have the width-to-thickness ratio smaller than 4.0 [185]. Shell elements may be predominantly used for CFS structures because standard CFS cross sections, such as Cees and Zeds available by Lysaght [186] for commercial use as purlins and girts in Australia, have a width-to-thickness ratios around 38.6. In addition, structural studs used for C-shaped framing members provided

by ClarkDietrich [187] have an average width-to-thickness ratios of 36.8.

Previous research investigations performed FE analysis with convergence studies on CFS members using a four-node shell element (S4R). Theofanou et al. [188] modeled stainless steel oval hollow sections with thicknesses between 1.9 mm and 3.2 mm using the S4R element, and the ratio of the mesh size to the element thickness varied from 4 to 10.3. As the thickness of the cross section increased, the mesh size decreased. Natario et al. [189] developed FE models for a 4.73 mm thick plain channel section with the mesh size-to-thickness ratio of 1.8 for the flange and 3.2 for the web. Keerthan and Mahendran [190] utilized the element size of 5 mm $\times$ 5 mm for 1.5 mm or 1.9 mm thick lipped channel beams with web openings. Pham [191] used a mesh size of 5 mm for 2 mm thick channel sections. Buchanan et al. [192] employed FE analysis of 1.34 mm thick circular hollow sections. A size of t $\times$ t shell element was adopted which led to 1.0 as the mesh size-to-thickness ratio. Pham et al. [193] modeled a shear test of lipped channel beams that have thicknesses varying 1.2 mm to 3.0 mm with a mesh size of 5 mm. Different mesh sizes were used in the test set-up: 5 mm for the angle straps and 10 mm for other parts of the test set-up such as the stocky column, loading plates, and thick plates.

Based on the studies covered in this section, the mesh (four-node shell element) size-to-thickness ratio varied from 1.0 to 10.3 with a mean value of 4.4. The value of 4.4 can be used as the approximate mesh size-to-thickness ratio. Appropriate element sizes would be different based on the geometric properties such as cross section type and thickness. The authors recommend performing validation sensitivity checks to determine the mesh size that obtains accurate results or use the mesh size based on the approximate mesh size-to-thickness ratio for all elements in the cross-section.

7.2.4 Geometric imperfection

As the pattern and magnitude of geometric imperfections have a significant effect on the structural behavior, correct modeling of the geometric imperfections is necessary to accurately predict the response of the structure. Section 5 of EN 1993 [4], [171] provides guidance of modeling geometric imperfections such as global imperfections for frames and bracing systems and local imperfections for individual components. Appendix B4 of AS/NZS 4600 [6] and Section 3 of AS 4084 [177] suggest considering the effects of geometric imperfections including frame (out-of-plumbness), member (out-of-straightness), and cross-section (distortional) imperfections. Chapter C of AISI [5] recommends considering the effect of initial imperfections for system stability design.

Frame imperfection

EN 1993-1-1 [4] permits the use of global imperfections derived from the elastic buckling mode where the shapes of the most critical buckling mode should be adopted. An equivalent imperfection of $\phi = \phi_0 \alpha_h \alpha_m$ can be directly modeled as the initial sway imperfections, where $\phi_0 = 1/200$, $\alpha_h = 2/\sqrt{h}$ is the reduction factor for the structure height h, $\alpha_m = \sqrt{0.5(1 + 1/m)}$ is the reduction factor for the number of columns in a story m. AS/NZS 4600 [6] and AS 4084 [177] adopt an out-of-plumbness ratio of 1/500 as the magnitude of frame imperfections in advanced analysis. Otherwise, the effects of frame imperfections can be considered by applying notional horizontal forces for regular single or multi-story framing structures [4], [6]. Section C1.1 of AISI S100 [5] states that the effect of global geometric imperfections shall be considered in the elastic design by using notional loads or directly using initial imperfections. When a structure supports gravity loads predominantly through columns, walls, or frames, the direct modeling of initial imperfections is permissible in the analysis for gravity-only load combinations, but not for load combinations

including applied lateral loads.

Member imperfection

According to EN 1993-1-3 [171], design values of member imperfections related to flexural buckling and torsional flexural buckling should be adopted from Table 7.3 with values based on analysis methods including elastic or plastic analysis and five buckling curves illustrated in Fig. 7.4. Fig. 7.4 plots the reduction factor χ for buckling resistance versus the non-dimensional slenderness λ, which is calculated as $\sqrt{(Af_y)/N_{cr}}$, where A is the cross-sectional area, f_y is material yield strength, and N_{cr} is the elastic critical force; the effective area A_{eff} is used in place of A when the cross section experiences local buckling. The selection of the appropriate buckling curve is based on the type of cross section, axis of buckling, and yield strength used. For example, back-to-back lipped (or plain) channel sections for buckling about the strong axis or the weak axis require buckling curves a and b, respectively. Closed built-up cross sections require buckling curve b when using nominal yield strength or buckling curve c when the average yield strength is utilized. Lipped C and Z sections require buckling curve b, and any other cross sections require buckling curve c. Member imperfections related to lateral-torsional buckling require an imperfection magnitude of 1/600 for elastic analysis and 1/500 for plastic analysis. AS/NZS 4600 [6] and AISI S100 [5] apply the maximum value of 1/1000 of the member length for member imperfections, which is smaller than 1/250 that EN 1993-1-3 [171] employs for elastic analysis of lipped C and Z sections. Table 7.4 and Fig. 7.5a provide the equivalent geometric bow imperfections from EN 1993-1-5 [173].

Cross-section imperfections: local and distortional

Section 5.5 of EN 1993-1-3 [171] suggests to follow EN 1993-1-5 [173] to consider the effects of the local and distortional imperfections. Annex

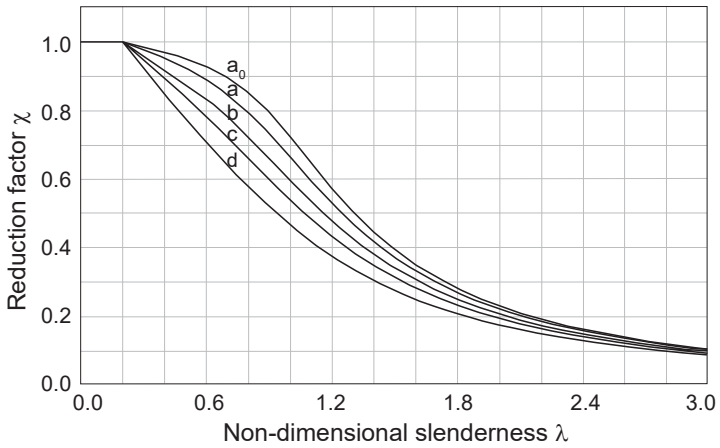

Figure 7.4: Buckling curves from EN 1993-1-1 [4]

Table 7.3: Design value of initial local bow imperfection e_0/L for members from EN 1993-1-1 [4]

Buckling curve	Elastic analysis (e_0/L)	Plastic analysis (e_0/L)
a_0	1/350	1/300
a	1/300	1/250
b	1/250	1/200
c	1/200	1/150
d	1/150	1/100

Note: e_0 is an initial bow imperfections; Buckling curves are illustrated in Fig. 7.4

C.5 of EN 1993-1-5 [173] provides equivalent geometric imperfections which may be used if there is an absence of a more refined analysis for the imperfections. Geometric imperfections may be based on the shape of the critical plate buckling modes. For cross-section imperfections, 80% of the geometric fabrication tolerances is recommended. The direction of the imperfection should be chosen which results in the lowest capacity. The equivalent geometric imperfections may be applied to the model with the values in Table 7.4 and Fig. 7.5b. When combining imperfections, a leading imperfection should be selected and the accompanying imperfections may have reduced values of 70%. Any type of imperfections can be the leading imperfections or the accompanying imperfections.

Table 7.4: Equivalent geometric imperfections from EN 1993-1-5 [173]

Type of imperfection	Component	Shape	Magnitude
Global	Member with length l	Bow	See Table 7.3
Local	Panel or subpanel with short span a or b	buckling shape	Min $(a/200, b/200)$
Local	Stiffener or flange subject to twist	Bow twist	1/50

Note: See Fig. 7.5 for the notation of a, b and l

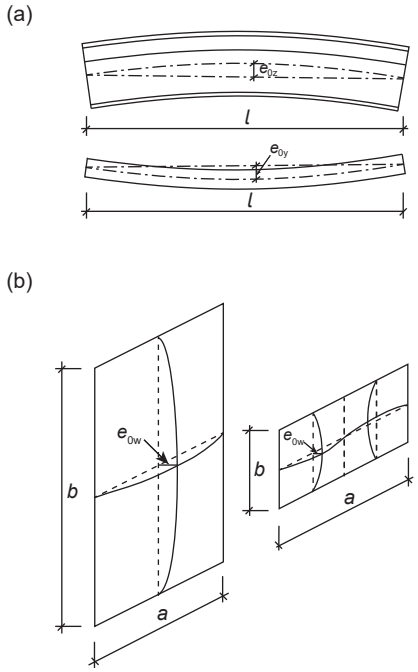

Figure 7.5: Modeling of equivalent geometric imperfections from EN 1993-1-5 [173]; (a) global member with length l (b) local panel or subpanel

AS/NZS 4600 [6] considers local and distortional buckling imperfections in the model by multiplying the local and distortional buckling modes by a factor. This factor, the unit maximum deformation, is determined by imperfection multipliers: the imperfection multiplier for local buckling is s_{ol} and the imperfection multiplier for distortional buckling is s_{od}, where $s_{ol} = 0.3t\sqrt{f_y/f_{ol}}$, and $s_{od} = 0.3t\sqrt{f_y/f_{od}}$, t is plate thickness, f_{ol} is elastic local buckling stress, and f_{od} is elastic distortional buckling stress. The scaled imperfections are superimposed onto the perfect geometry. The local and distortional buckling modes may be determined from a linear buckling analysis based on shell FE modeling or finite strip discretization of the member. However, for unbraced pitched roof cold-formed steel portal frames and unbraced cold-formed steel storage racks, local and distortional buckling imperfections are not required in the modeling.

Imperfection modeling recommendations from previous research

The effects of distortional buckling should be determined by performing linear or nonlinear buckling analysis [6], [171], which is a static method that accounts for material and geometric nonlinearities, using FE methods. Several studies performed buckling analyses and applied the imperfection magnitude and shape based on the analysis results. For example, Silvestre and Camotim [194] applied critical-mode initial imperfections to Z-section beams and columns with amplitudes of $\pm 0.15t$. Dinis et al. [195] incorporated a linear combination of critical buckling mode shapes with an initial imperfection amplitudes of $\pm 0.1t$ obtained from a post-buckling analysis of lipped channel columns. Landesmann et al. [196] considered distortional initial geometrical imperfections with an amplitude of $0.1t$ in numerical models of lipped channel, hat, and zed section columns.

Schafer and Pekoz [154] suggested a probabilistic approach for modeling the maximum imperfection magnitude as a random variable based on the distributions of collected data on the measured imperfection mag-

nitudes of CFS members. The CFS imperfections were categorized into two types including local imperfection in a stiffened element (Type 1) and deviation from straightness for a flange (Type 2). The imperfection values can be selected based on the given cumulative distribution function values of the two types of imperfections. The mean values of the maximum imperfection are 0.5t and 1.29t for Type 1 and Type 2, respectively, with the standard deviation values of 0.66 and 1.07.

Zeinoddini and Schafer [197] evaluated three methods for simulation of geometric imperfections in CFS members: (1) the Traditional Modal Approach that considers imperfections as a combination of buckling modes; the mode shapes are achieved from an eigenvalue buckling analysis of the member using five cross-sectional buckling mode shapes, (2) the 2D Spectra Approach that considers imperfections as a two-dimensional random field, and (3) 1D Modal Spectral Approach which is a combination of modal and spectral approaches; the spectral approach is used to generate the imperfection magnitudes in the longitudinal direction and the five mode shapes are considered in the transverse direction. A comparison of the simulation results obtained from the three methods shows that the Traditional Modal Approach is conservative for predicting the strength. The 2D Spectra Approach predicts the strength of models that have local and distortional failure with high accuracy, but it is less accurate when the global failure mode is dominant. The 1D Modal Spectral Approach accurately captures the imperfection distributions and the strength, axial flexibility, and failure mechanism of the member, it is thus the most appropriate method for simulation of imperfections in CFS members [197].

In summary, current standards mention that different types of geometric imperfections including frame, member, and cross-section should be considered in the analysis in directions which result in the worst case (e.g., lowest capacity). Global imperfections can be considered either directly in the structural model or applying notional loads for regular single or

multi-story framing structures [5], [6]. Imperfections should be determined based either on actual (measured) imperfections, if known [1], or on equivalent geometric imperfections indicated in the standards. Cross-sectional imperfections can be determined by linear/nonlinear buckling analysis using FE models [6], [171], [173]. The buckling modes with the lowest eigenmodes (critical-mode) should be chosen. The authors recommend that appropriate values for equivalent geometric imperfections for CFS members and structures be developed.

7.2.5 Residual stress

CFS design standards including AISI S100 [5] and EN 1993-1-3 [171] recommend considering stiffness reductions due to the effects of residual stresses and partial yielding. AISI S100 [5] includes the influence of residual stresses and partial yielding by using the reduction factor 0.9 and the additional factor τ_b, which considers the flexural stiffnesses, whereas Chapter C of AISC 360 [1] applies $0.8\tau_b$ to represent reduced stiffness. Appendix of AISC 360 [1] also considers stiffness reductions due to partial yielding of the cross section. Residual stresses shall be modeled indirectly through the stress-strain curve [6] or based on a stress pattern produced by the fabrication process with amplitudes equivalent to the mean (expected) values [171]. Advanced analysis provided in Chapter B4 of AS/NZS 4600 [6] suggests considering stiffness reductions due to the effects of residual stresses and partial yielding in addition to cross-section deformations or local and distortional deformations.

Residual stresses on cold-formed steel members typically consist of longitudinal membrane and bending components, which have constant and linear variations through the material thickness, respectively. Therefore, the residual stress pattern of combined membrane and bending is a linear relationship [154]. Residual stresses in the transverse direction can be assumed to be negligible [198]. Liu et al. [199] developed a simplified

residual stress model for cold-formed hollow steel sections by accounting for only the longitudinal bending component. The simplified model showed an error of less than 4% with the model that considered all residual stress components for the ultimate load prediction. This is because the longitudinal residual stress is more significant than the transverse residual stress, and the residual stress in the longitudinal direction is governed by the bending component rather than the membrane component.

The membrane residual stress component is relatively small compared to bending residual stresses in cold-formed sections, but it should be considered when modeling corner regions where membrane residual stresses primarily exist [154]. Mutafi et al. [200] simulated the cold forming process by performing three-dimensional FE analysis of one corner of 1.8 mm- and 1.63 mm-thick lipped channel sections and explored longitudinal residual strains at the corner region. The simulation resulted in high residual strains at the corner edge that exceed the yield strain, which is significantly different from the residual strains at the flat edge. Moen et al. [201] provided a method for predicting initial residual stresses in cold-formed steel members. The proposed method considers residual stresses resulting from two manufacturing processes including (1) sheet coiling, uncoiling, and flattening, and (2) cross section roll-forming. Equations for predicting the through-thickness residual stress in corner and flat regions resulting from the manufacturing processes are derived based on experimental results. The experimental results showed that corners have larger residual stresses than the flats. The equations of residual stresses resulting from sheet coiling, uncoiling, and flattening includes longitudinal residual stresses only, while the equations for cross section roll-forming represent the transverse and longitudinal residual stresses. Residual stresses can be considered in FE models by directly applying the equations which represent the manufacturing processes and corner/flat regions.

Residual stresses should be modeled in an analysis as they may result

in a reduced stiffness which can cause increased deflections and second-order bending moments. The membrane component can be ignored when modeling the flat regions where the bending component dominates the residual stresses in the longitudinal direction. When modeling residual stresses at the corner regions, however, both bending and membrane components should be considered. Residual stresses in the transverse direction could be ignored because of its reduced impact compared to the longitudinal residual stresses. Otherwise, the equations for cross section roll-forming provided by Moen et al. [201] could be used to consider both transverse and longitudinal components.

7.2.6 Second-order effects

The design standards for cold-formed steel (AISI S100 [5] and AS/NZS 4600 [6]) and hot-rolled steel (EN 1993-1-1 [4], AS 4100 [10], and AISC 360 [1]) require/suggest considering second-order effects in the analysis. AISI S100 [5] considers second-order effects $P-\Delta$ and $P-\delta$ only. AS 4100 [10] includes second-order effects in the analysis, while the type of second-order effects is not specified. EN 1993-1-1 [4] and AS/NZS 4600 [6] include second-order effects arising from deformed geometry not limited to $P-\Delta$ and $P-\delta$. Appendix 1 of AISC 360 [1] includes geometric nonlinearities such as $P-\Delta$, $P-\delta$, and twisting effects. Section 3 of AS 4084 [177] considers twist rotations and torsional internal actions including warping torsion in the analysis.

For non-doubly symmetric cross section members, however, the consideration of only $P-\Delta$ and $P-\delta$ in a second-order analysis is not enough to fully reflect behaviors related to asymmetry [202]. Sippel and Blum [202] analyzed the response of non-doubly symmetric cross-section beam members. The analysis results were used to evaluate that the methods can accurately capture behaviors related to asymmetry. The inclusion of only $P-\Delta$ and $P-\delta$ in a second-order analysis is not enough to fully

reflect the behavior of non-doubly symmetric sections. The consideration of twisting effects including warping, the center of twist, and second-order twist effects are important to the analysis of non-doubly symmetric cross sections. Moreover, the inclusion of asymmetric cross-section properties such as nonconcentric shear center and centroid affects the analysis results. It is examined that the inclusion of the asymmetric section properties in structural systems with non-symmetric sections formed from cold-formed steel members is important. Thus, the authors recommend including the effects from twisting effects in addition to the effects of $P-\Delta$ and $P-\delta$ when a non-doubly symmetric cross section is analyzed.

7.2.7 Connections

AISI S100 [5] and AS/NZS 4600 [6] provide requirements for modeling of connections. Connections shall have sufficient strength and ductility to avoid structural failure within the connections and ensure that the structure fails within the members. In addition, if connections show nonlinear behavior, it shall be included in the analysis [6]. Connection deformations and uncertainty in connection stiffness and strength shall be considered [5], [6].

Although the CFS design standards [5], [6], [171] have no classification of the type of connection model, the authors recommend referring to the hot-rolled steel design standards or to recent research on CFS connections. For connection modeling, for example, CSA S16 [7] provides three types of connections including simple, rigid, and semi-rigid. The design moment-rotation characteristic of a joint may adopt a simplified curve including a linearized approximation such as bi-linear or tri-linear when the simplified curve lies entirely below the design moment-rotation characteristic [4].

Since connections of CFS portal frames, storage racks, and built-up sections used in framing display semi-rigid behavior [203]–[205], the inclusion of semi-rigidity is significant for the modeling of CFS structures

and AS 4084 [177] suggests accounting for semi-rigidity of connections in storage racks. The type of connections can be determined by experimental results or previous experience in similar cases. However, the assumption of a pinned connection in racks or studs seated in track should be avoided because it leads to large displacement which decreases system stability [204], [205]. Rinchen and Rasmussen [206] investigated the connection behavior of CFS portal frames with single C-section members and proposed simplified multi-linear moment-rotation characteristics for eaves, apex, and column base connections, which can be used for modeling the semi-rigidity of connections.

Moment-resisting joints on CFS frames have been studied by several researchers, in particular bolted moment-connections between CFS members, which are formed through brackets bolted to the webs of the cross-section. Lim and Nethercot [207] suggested considering web buckling in the design of bolted moment connections. The concentration of load transfer from the bolts may cause web buckling, which results in the connections having a lower moment capacity than that of the connected CFS sections. Lim et al. [208] conducted a parametric study of bolted moment connections in CFS portal frames in which the connections are subjected to a combination of bending and bimoment. Phan et al. [209] considered the bolt-group length to determine the flexural strength of bolted moment connections in addition to the effect of bimoment. It was found that the effect of bimoment is particularly significant in the section adjacent to the connection for a short bolt-group as it reduces the moment capacity of the section. Therefore, the bimoment effect must be considered in CFS connection design.

Several design equations for CFS moment-resisting connections were previously proposed. Mojtabaei et al. [210] developed a practical design equation for CFS moment-resisting bolted connections. This equation overcomes the limitation of the previous equations proposed by Lim and

Nethercot [207] and Natesan and Madhavan [211], which are valid only within a certain range of design parameters. Design equations for the capacity of CFS bolted connections under combined axial compression, shear, and bending moment are proposed [212]. Chen et al. [213] proposed a design equation to predict the moment capacity of apex brackets in portal frames based on the results of an FE based parametric study.

For the modeling of structural steel joints, Zhu et al. [214] proposed a generalized component model that predicts the full range behavior of the steel connections, which is applicable to all types of steel connections. The developed tri-linear spring model can predict the three ranges of the moment-rotation curve, including the elastic, post-yielding, and post-ultimate regions. The authors recommend considering the effects of connection behavior, such as semi-rigid behavior and bimoment, and modeling them by applying the previously proposed moment-rotation characteristics of connections.

7.2.8 The effect of holes

Web crippling in thin walled members is a critical problem especially for beams with slender webs which are generally not stiffened against localized loads [215]. Cold-formed steel sections used as wall studs or floor joists contain web holes for convenient installation of services such as pipes and cables, and the design of these sections should consider the effect of holes, which may result in local buckling of the web. Section 6.1 of EN 1993-1-3 [171] suggests using testing by analysis particularly for cross-sections with high element slenderness involving web crippling. AISI S100 [5] permits using numerical methods for providing solutions for members with holes. In particular, the use of shell elements is preferred when modeling members that incorporate specialized details of the section along the member length.

Design recommendations for members that have web holes have been

provided by researchers based on the results of both experimental tests and FE analyses. Uzzaman et al. [215] and Lian et al. [216] conducted parametric studies to investigate the effect of circular web holes on the web crippling strength of lipped channel sections, and they proposed a reduction factor for the web crippling strength. The effects of web holes on the shear capacity of CFS members have been studied, such as channel sections with square and circular web holes [217], and channel sections with non-elongated and elongated web holes [218]. Design approaches to predict the shear strength of perforated members with non-elongated web holes [219] and elongated web holes [193] were provided. As the web holes in cold-formed steel members lead to a reduction in shear capacity, the effect of holes should be considered in numerical modeling of the members.

7.2.9 Uncertainty

It is difficult to predict the actual performance of cold-formed steel structures with certainty due to random variations in the input parameters. AISI S100 [5], AS/NZS 4600 [6], AISC 360 [1], and CSA S16 [7] include uncertainty in strength and stiffness which affect the behavior of structures in the analytical model. Consideration of uncertainty in the strength and stiffness properties must be modeled to obtain the most adverse effects on the structure [7]. A reduction factor of 0.9 shall be applied to yield stress and stiffness of all steel members and connections to account for the uncertainty in system, member, and connection strength and stiffness [1]. In addition, AS/NZS 4600 [6] provides capacity reduction factors (ϕ) for the strength and stability limit states of pre-qualified frames. Values of ϕ are determined from reliability analyses of the frames [220], [221]. The frames should support the factored limit states actions multiplied by $1/\phi$, where ϕ is 0.85 for CFS portal frames and 0.9 for steel storage racks.

Test-based design provided by Chapter K of AISI S100 [5] requires

structural performance to be established by tests or rational engineering analysis with confirmatory tests. The strength of the tested elements, assemblies, connections, or members is determined based on the same procedures used to calibrate the LRFD design criteria, as given in Eq. 7.1. The resistance factor (ϕ) computed by Eq. 7.2 considers the uncertainty in material and geometric properties, failure mode, and prediction of the resistance,

$$\sum \gamma_i Q_i \leqslant \phi R_n \tag{7.1}$$

where γ_i is load factors; Q_i is load effects; and R_n is nominal resistance

$$\phi = C_\phi (M_m F_m P_m) e^{-\beta_o \sqrt{V_M{}^2 + V_F{}^2 + C_P V_P{}^2 + V_Q{}^2}} \tag{7.2}$$

where

C_ϕ = calibration coefficient
β_o = target reliability index
V_Q = coefficient of variation of load effect, the values are given in AISI S100 [5].
M_m = mean value of material factor
F_m = mean value of fabrication factor
V_M = coefficient of variation of material factor
V_F = coefficient of variation of fabrication factor, the values are listed in Table K2.1.1.1-1 of AISI S100 [5].
C_P = correction factor, $(n+1)(n-1)/n(n-3)$ for $n \geqslant 4$ and 5.7 for $n = 3$ in which n is the number of tests not fewer than three.
P_m = mean value of professional factor for tested component, $(1/n)\sum_{i=1}^{n}(R_{t,i}/R_{n,i})$ in which $R_{t,i}$ is tested strength and $R_{n,i}$ is calculated nominal strength.
V_P = coefficient of variation of test results

R_n = average value of all test results

The correlation coefficient (C_c) between the tested strength and the nominal strength predicted from the rational engineering analysis model shall be greater than or equal to 0.8. The bias and variance between the measured and the nominally specified dimensions and material properties shall be reflected by including fabrication (F_m and V_F) and material (M_m and V_M) factors to the calculation of resistance factor. The authors recommend considering uncertainties in material and geometric properties because they affect the response of a member or a structure.

7.2.10 Benchmark test

When testing by analysis is implemented, it is important to validate against benchmark analytical solutions to demonstrate that the model is reliable. Annex C of EN 1993-1-5 [173], Appendix B of AS/NZS 4600 [6], and Chapter C and Appendix 1 of AISC 360 [1] require performing benchmark tests to prove the software is appropriate for the task. In Appendix 1 of AISC 360 [1], benchmark tests are used to check if the second-order effects resulting from the combination of axial force, flexure, and twist are being correctly performed in elastic analysis. Otherwise, according to Chapter C, benchmark problems are used to verify that the $P-\delta$ and $P-\Delta$ second-order analysis used in the direct analysis method provides a confidence level of the analysis results. Benchmark tests can be performed by well-documented experimental results or similar benchmark results [6].

Pham [191] used the finite-strip method as a benchmark test of the FE method for elastic buckling analysis and the results from the two methods agree within 2% error. Ziemian et al. [222] performed benchmark problems to ensure that the nonlinear analysis of an unbraced I-shaped

member subjected to in-plane and out-of-plane loading effects that have significant spatial behavior such as warping and twisting effects achieves accurate results. The benchmark problems are crucial in validating the proper use of nonlinear analysis when the modeling of spatial behavior is important. Denavit [223] verified the direct analysis method provided in AISC 360 [1] by providing benchmark studies for the second-order inelastic analysis results on wide ranges of cross section parameters such as depth, thickness, and width. Overall, it is recommended to perform benchmark tests to validate the accuracy of the software and modeling method.

7.2.11 Dimension: 2D or 3D

Annex O of CSA S16 [7] and Appendix B of AS/NZS 4600 [10] include provisions for dimension of the model. CSA S16 [7] requires using a three-dimensional model, but a two-dimensional model can be employed providing that the use of model is validated for design. For the use of a two-dimensional model, it is required to consider the out-of-plane response. AS/NZS 4600 [6] addresses the case of using a two-dimensional model without provisions for using three-dimensional analysis. A two-dimensional model can be used for analyzing regular building structures by considering them as a series of parallel two-dimensional substructures. The analysis should be carried out in two directions at right angles. However, the use of two-dimensional analysis is not applicable to structures that have significant load redistribution between the substructures. As it is important to consider the spatial behavior in analysis [202], [222], the authors recommend employing a three-dimensional model to achieve correct structural responses.

7.2.12 Superposition principle

ACI 318 [172] does not allow the use of the linear superposition principle, which considers the net response as the sum of the individual responses, e.g., when determining the ultimate inelastic response of a member, it is incorrect to analyze for service loads then combine the results linearly using load factors. A separate inelastic analysis will be performed for each factored load combination. The authors recommend not to use the superposition principle as it would result in different responses from the actual responses considering equilibrium on the deformed shape and second order effects.

7.2.13 Documentation of results

EN 1993-1-5 [173] suggests to document details of the analytical model including the mesh size, loading, boundary conditions, and other input/output data to be reproduced by third parties. To implement design by analysis, the authors recommend documenting the analytical model information and analysis results.

7.3 Selected Recent Research

This section introduces three studies regarded as good examples of testing by analysis using numerical modeling. These studies were selected because they employ multiple modeling aspects as detailed in this paper. While additional studies exist which utilize the recommended modeling methods for cold-formed steel structures, only three examples were selected because they illustrate the process that this paper outlines in Section 7.2. For example, the selected studies explored full nonlinear finite element models of CFS members and systems as well as discussed the challenges and solutions of testing by analysis of cold-formed steel struc-

tures. Moreover, the studies utilized numerical data to extend the physical testing database to cover a wider range of geometrical and material properties and loading conditions, thereby expanding the range of application of the design approach. The modeling methods and solutions provided by these studies demonstrate the application of virtual testing to cold-formed steel design. Although Abaqus [122] was used as the modeling software in the three studies, other finite element software packages with shell elements such as Ansys [224], SAP2000 [225], RISA [226], etc. could be employed. Mastan2 [183] with line elements could be used because it can accurately model the behaviors related to non-symmetric cross-sections. However, the line elements are not capable of directly considering local or distortional buckling [182].

7.3.1 Buchanan et al. (2020)

Buchanan et al. [192] conducted a numerical investigation of experiments on ferritic stainless steel circular hollow section beam-columns subjected to combined axial loading and bending moment. More than 2,000 simulations conducted in Abaqus [122] were generated to carry out a parametric study covering austenitic, duplex, and ferritic grades of stainless steel and a wide range of cross section, member slenderness, and applied loading eccentricities, while only 26 beam-column physical experiments were carried out.

The FE models utilized the 4-node doubly curved shell element (S4R). A mesh validation study was performed with the element size varying from 10t to t/3, where the thickness t is 1.34 mm. A size of t $\times$ t shell element was adopted as it yielded accurate failure load and deflection from the finest mesh, t/3, while maintaining computational efficiency. In addition, computational efficiency was increased by modeling half of the cross section and employing symmetrical boundary conditions. The FE models utilized the stress-strain relationships obtained from the

measured tensile coupons and compressive stub column responses. The effect of membrane residual stresses was neglected while the through-thickness residual stresses are implicitly considered by using measured material properties. The modeling of boundary conditions followed the test conditions. The form of local and global geometric imperfections adopted the lowest local and global buckling mode shapes from an elastic buckling analysis. The measured mid-point global imperfections (ω_o) and L/1000 were adopted for the global imperfections, and t/10 and t/100 were utilized for local imperfections, where L is the effective length and t is the section thickness.

In addition to the validation of the numerical models against the experimental results, parametric studies were conducted to support the development of new design rules for beam-columns in EN 1993-1-4 [227], with various amplitudes of imperfections and material properties including compressive and tensile properties. The numerical models were validated by comparing the ultimate load and the mid-height lateral deformation at the ultimate load. The predicted values of ultimate load and lateral deflection were within 5% error against the measured values using the compressive material properties, whereas beyond 10% error occurred when the tensile coupon properties were utilized. This demonstrates the importance of using the proper material models for the analysis, therefore the compressive material properties were adopted for the numerical models.

7.3.2 Pham et al. (2020)

Pham et al. [193] developed FE models using Abaqus [122] to validate against shear tests of cold-formed steel channel sections with both small and large web holes. A parametric study was performed to extend the experimental database. This study proposed a new Direct Strength Method of design of perforated channels in shear that can be applicable to a wider

range of sectional dimensions and thicknesses.

In the FE models, the S4R element with a mesh size of 5 mm was used for the cold-formed channel sections while the 8-node linear solid element (C3D8R) was used for the test set-up with a mesh size of 5 mm for the angle straps and 10 mm for other parts of the test set-up such as the stocky column, loading plates, and thick plates. The area surrounding the web openings adopted sweep meshing. The modeling of boundary conditions and connections followed the physical tests. The nonlinear behavior of the bolted connection was included in the analysis by using the nonlinear elastic properties obtained from the test results. For the material properties, the true stress-strain curve as previously shown in Fig. 7.1 was adopted with measured stress and strain from the tensile coupon tests. The initial geometric imperfections were specified by the buckling modes with the lowest eigenvalue because the lowest buckling modes normally represent the critical buckling modes. Two scaling factors for the imperfection, 0.15t [194] and 0.64t [154], were employed as the imperfection amplitudes to measure imperfection sensitivity.

The ultimate shear strengths produced by the FE models and the physical tests were compared and the maximum percent difference was 5.37%. Moreover, the FE models produced similar shear failure modes with the tests. It was shown that the developed FE models properly simulated the physical tests.

7.3.3 Kyvelou et al. (2018)

Kyvelou et al. [228] developed FE models of composite flooring systems composed of cold-formed steel channel section beams with two stiffeners and wood-based particle boards using Abaqus [122]. One hundred simulations were generated and the simulation results were validated against twelve physical test results. A parametric study was conducted to investigate the effect of key parameters on the performance of the flooring

systems including the depth and thickness, and the spacing of fasteners.

The material model adopted the two-stage Ramberg-Osgood model proposed by Gardner and Ashraf [229]. This study carried out corner coupon tests and it was determined that the corner regions have 17% higher yield strength than the flat regions. The strength enhancements in the corner regions were considered by assigning different material properties. The effect of through-thickness residual stresses was implicitly included in the stress-strain curves. The S4R shell elements with a longitudinal size of 10 mm were chosen for the modeling of the CFS beams. The C3D8R solid elements with a longitudinal size of 10 mm were used to model the wood-based flooring panels. The self-drilling screws, which acted as the shear connection between the joists and the flooring panels, were modeled with nonlinear spring elements that consider the load-slip response based on the push-out test results. For modeling of initial geometric imperfections, the pure local and distortional buckling mode shapes were obtained from CUFSM [184]. The obtained buckling modes were distributed longitudinally, through sinusoidal functions, and the deformed geometry was directly modeled in Abaqus [122]. The scaling factors for the local and distortional buckling mode shapes, 0.1t [230] and 0.3t [231], respectively, were employed as the imperfection magnitudes.

The ultimate moment capacities and flexural stiffnesses were compared to confirm if the developed FE models accurately predicted the test results. The mean ratios of predicted to tested results for moment capacities and flexural stiffnesses were 0.99 and 1.04, respectively. In addition, the FE models accurately predicted the exhibited failure modes, load-displacement responses, and strain distributions at the ultimate load. This study determined the key parameters for the flooring system behaviors by conducting parametric numerical studies.

7.4 Conclusion

Testing by analysis is a promising alternative to physical experimentation by reducing costs and time for performing the tests. The use of testing by analysis is becoming common in the cold-formed steel structural industry. This paper reviews the existing standards for cold-formed steel structures and other industries that include testing by analysis requirements and the studies that provide information about the factors to be considered in testing by analysis. Moreover, the selected research that implemented overall numerical analysis of cold-formed steel members and systems are reviewed. The main recommendations on the use of virtual testing for cold-formed steel design can be summarized as follows:

- The material model should include the nonlinear stress-strain relationships which can capture the inelastic behavior of structural members or systems.
- As the modeling of a cross section without consideration of the rounded corners decreases the modeling accuracy, the effects of the rounded corners should be considered.
- Appropriate mesh size should be determined by performing validation sensitivity checks with successive refinement. Otherwise, the proposed mesh size-to-thickness ratio of 4.4, which is the mean value based on the discussed studies, can be used.
- Frame, member, and cross-sectional imperfections should be included in the analysis in the direction which results in the most conservative results (lowest capacity). The values of imperfections can adopt either the equivalent geometric imperfections given in the existing standards or the values based on actual measurements.

- It is recommended to include the effects of residual stress as their presence may result in a reduced member stiffness thereby causing increased lateral deflections and second-order bending moments. Residual stresses may be incorporated by either indirectly modeling their effects through the material stress-strain curve or by modeling the stress pattern produced by the fabrication process. Additionally, equations which predict the residual stresses based on the fabrication process may be utilized.

- To accurately analyze the behavior of nonsymmetric cross section members, twisting effects should be considered in addition to $P - \Delta$ and $P - \delta$.

- Cold-formed steel connections can be classified into simple, rigid, and semi-rigid, which are referenced from the hot-rolled steel design standards. As cold-formed steel structural systems showed semi-rigid behavior in connections, the effects of semi-rigid should be considered in connection modeling. The moment-rotation characteristics for connections proposed by the discussed studies could be used for the modeling.

- It is recommended to consider the effect of web holes in members as the holes result in a reduction of shear capacity.

- Uncertainties in strength and stiffness should be included because they affect the structural behaviors.

- In order to validate that the software used for testing by analysis is reliable, benchmark analytical solutions should be provided.

8.1 Summary and Conclusions

Current advancements in the steel industry have spurred the need for detailed guidance in using advanced analysis methods. Ultimately, this dissertation augmented data-driven and advanced analysis approaches for steel design.

Data-driven approaches were implemented into structural steel analysis to address the existing challenges in using conventional design methods. As discussed in Chapter 2, when assessing the effect of uncertainty on the failure of steel frames, a conventional reliability-based sensitivity analysis method demands a high computational cost and time since it requires evaluations of the performance function. The proposed machine learning-based sensitivity analysis framework improved the computation efficiency by considering all the uncertainties at once to estimate their effects. Moreover, the proposed framework was able to determine the parameters that have negligible impact on the system failure. Removal of the redundant parameters showed a higher prediction accuracy compared with considering all parameters in model training. Large-scale engineering problems often carry a large number of uncertain parameters, which exacerbates the challenge of using the conventional method for sensitivity analysis. This demonstrated the proposed framework has benefits for the system-level design of steel structures.

Most structures are designed to have a low probability of failure, therefore a dataset classified based on the failure status is mostly imbalanced due to a small sample size of failures and a large sample set of safe structures. Imbalanced data may lead to poor predictive performance. Three countermeasures were considered to address the class imbalance problems: (1) The minority class, structural failure, was oversampled to have

the same number of the majority class, safe structures, in a training set. (2) a larger portion of data was used for model testing because of a scarce number of failures in the dataset. (3) an evaluation metric reliable for imbalanced classification problems, which is the Matthews correlation coefficient, was used to evaluate the predictive performance.

In addition to implementing data-driven approaches into the system-level design, the approaches were adopted for member-level design to predict the buckling capacity of steel hollow sections in Chapter 3. This investigation highlighted the use of a large dataset that covers a wide range of material and geometric properties. This addresses the limitation of the existing provisions which have limited scope such as the lack of high-strength steel for hollow section design and lack of specifics for residual stresses of a recent formation method. The predictive performance of the developed data-driven models showed high accuracy over the range of the member slenderness ratio and across different steel grades and fabrication techniques. Moreover, it was demonstrated that the data-driven models lead to consistent performance over the range of the parameters compared with the results obtained by the existing design rules which have relatively large errors and variance.

The Chapter 3 study compared the predictive performance of the data-driven models by experimental data only, finite element data only, and combined data. The model assessment with the experimental data showed the lowest accuracy due to its small sample size, but it was higher than the demanded performance for estimating structural responses. This indicated that the use of both data sources in machine learning could inform future generations of design specifications.

Analytical studies on rotary-straightened steel members were conducted in Chapters 4 and 5 to update the finite element analysis method for steel members considering the recent manufacturing technology. Rotary-straightened sections have a different residual stress distribution from

the sections fabricated without rotary-straightening, but the effect of their residual stresses is not reflected in the stiffness reduction models specified in the existing design provisions. The projects conducted a parametric study on the stiffness reduction models that reflect different residual stress patterns for W-shapes and rotary-straightened W-shapes. Limit load analyses were conducted for columns and beam-columns under various axial load conditions, member slenderness ratio, and axis of bending. The stiffness reduction model for rotary-straightened members resulted in larger capacities for members with large slenderness ratios or members under high axial compression loads compared with the stiffness reduction models for hot-rolled steel members. This may lead to unconservative analysis results of rotary-straightened members when their residual stress distribution is ignored. The results of Chapter 4 emphasizes the use of an appropriate residual stress pattern for rotary-straightened members in finite element analysis.

Building upon the parametric study on the stiffness reduction models, data-driven models were developed to predict their limit load capacity and explore the applicability of a data-driven approach for the stability design of steel members. Although the predictive performance of the developed data-driven models was high overall, the performance was inconsistent in different random split cases. This can be improved by increasing the sample size.

An experimental study on residual stress of cold-formed steel members was conducted in Chapter 6. This study quantified residual stresses in advanced high-strength steel sections using the hole-drilling method. Lipped angles fabricated from dual-phase steel sheets were used for the experiment. The hole-drilling method assumes the linearity of materials to estimate residual stresses while advanced high-strength steel incorporates a rounded stress-strain curve. Therefore, experimental calibration was also conducted to consider the nonlinearity of the material and update

calibration constants for the material. Residual stresses were estimated based on the measured residual strains and calibration constants. It was observed that higher residual stress occurred at the near corner regions compared with the flat regions in a cross section. The residual stress values were compared with the results derived by the sectioning method. The comparison demonstrated that the hole-drilling results are comparable with the sectioning results.

Overall, advanced analysis techniques were shown to be promising for steel structural design and analysis. This study presented cases of how to address existing challenges in using the current methods for estimating the behaviors of steel members and frames. The guidance provided in this study will assist engineers in understanding how to develop reliable data-driven approaches to solve structural engineering problems and implement novel technologies into structural design.

8.2 Future work

This dissertation has provided detailed information for the implementation of data-driven approaches and advanced analysis into steel structural design and analysis, which supports structural engineers to utilize the recent techniques including machine learning and numerical analysis in practice. Future work may include the following tasks regarding the use of data-driven and advanced analysis for steel structural design:

1. Additional machine learning algorithms could be evaluated to further validate the proposed sensitivity analysis method. Logistic regression and a decision tree, which are one of representative regression-based and tree-based classifiers, were examined for sensitivity analysis of steel frames. The models showed different performance curves from each other. Benchmark studies on the feature importance ap-

proach with multiple machine learning methods might be a potential way to generalize the presented sensitivity analysis approach.

2. Data-driven models need to achieve a better prediction for the minority class, which is a system failure in this project. This is highlighted for a frame with a complex failure mode, which was progressive yielding according to Chapter 2. The frame had a larger imbalanced ratio as well as a higher dimension space than the other frame with a simple failure mode, which is the instability of a single column in this study. Future research may include training a deep learning model to achieve high accuracy for high-dimensional data. In addition, dimension reduction techniques such as generalized sliced inverse regression using active learning [232] or feature selection techniques using deep learning [233] can be utilized.

3. Studies on the correlations between the imbalanced ratio, data space, and the degree of complexity in failure modes would help enhance the presented approach. For a frame with a complicated failure mode, which had a high imbalanced ratio, the number of observations was increased to obtain more samples of the minority class in a dataset, therefore increasing the data complexity and computational cost. Model development using data for structures with various failure modes, which would have different imbalanced ratios and data space, would provide suggestions for future implementation of machine learning-based structural analysis.

4. As for research about rotary-straightened steel sections, more investigation could be conducted on the frame analysis of rotary-straightened sections considering the effect of residual stresses on stiffness reduction. Since beam-columns with major or minor axis bending had different cross section dimensional characteristics that

affect the limit load capacity, the bending axis conditions should be considered in the frame analysis.

5. Model validation studies on previous experimental data for rotary-straightened columns and beam-columns could be conducted. Since rotary-straightened W-shapes are commonly used in the construction industry, the study would help determine an appropriate stiffness reduction factor for systems with these members.

6. Elaborate frame models such as three-dimensional shell FE models can be developed to examine the effect of residual stresses on behaviors of rotary-straightened sections in detail.

7. Chapter 7 provided recommendations for testing by analysis for cold-formed steel structures. Investigations on the design of cold-formed steel structures following the recommendations could be conducted to provide a further understanding of the practical use of testing by analysis.

BIBLIOGRAPHY

[1] *Specification for structural steel buildings*, 360, ANSI/AISC, Chicago, IL, 2016.

[2] X. Meng and L. Gardner, "Behavior and design of normal-and high-strength steel shs and rhs columns," *J Struct Eng*, vol. 146, no. 11, p. 04 020 227, 2020. DOI: 10.1061/(ASCE)ST.1943-541X.0002728.

[3] X. Ge and J. Yura, "The strength of rotary-straightened steel columns," in *Proceedings of the 2019 SSRC Annual Stability Conference*, St. Louis, MO, 2019.

[4] European Committee for Standardization, *Eurocode 3—Design of steel structures—Part 1-1: General rules and rules for buildings*. Brussels, Belgium: EN 1993-1-1, 2014.

[5] AISI S100-16, *North American Specification for the Design of Cold-Formed Steel Structural Members*. AISI, 2016.

[6] AS/NZS 4600, *Cold-Formed Steel Structures*. Standards Australia, 2018.

[7] CSA S16:19, *Design of Steel Structures*. Canadian Standards Association, 2019.

[8] H. Sun, H. V. Burton, and H. Huang, "Machine learning applications for building structural design and performance assessment: State-of-the-art review," *J Build Eng*, vol. 33, p. 101 816, 2021. DOI: 10.1016/j.jobe.2020.101816.

[9] O. A. Sediek, T.-Y. Wu, J. McCormick, and S. El-Tawil, "Prediction of seismic collapse behavior of deep steel columns using machine learning," *Struct*, vol. 40, pp. 163–175, 2022. DOI: 10.1016/j.istruc.2022.04.021.

[10] AS 4100, *Steel Structures*. Standards Australia, 1998.

[11] T. Chen and C. Guestrin, "Xgboost: A scalable tree boosting system," in *Proc. of the 22nd acm sigkdd international conference on knowledge discovery and data mining*, 2016, pp. 785–794.

[12] R. Ziemian, W. McGuire, and S. Liu, *MASTAN2 v5.1.20*, 2019.

[13] Y.-T. Wu, "Computational methods for efficient structural reliability and reliability sensitivity analysis," *AIAA J*, vol. 32, no. 8, pp. 1717–1723, 1994. DOI: 10.2514/3.12164.

[14] R. Y. Rubinstein and D. P. Kroese, *Simulation and the Monte Carlo method*. John Wiley & Sons, 2016, vol. 10. DOI: 10.1002/9781118631980.

[15] A. J. Torii, R. H. Lopez, and L. F. F. Miguel, "Probability of failure sensitivity analysis using polynomial expansion," *Probabilistic Eng Mech*, vol. 48, pp. 76–84, 2017. DOI: 10.1016/j.probengmech.2017.06.001.

[16] C. Proppe, "Local reliability based sensitivity analysis with the moving particles method," *Reliab Eng Syst Saf*, vol. 207, p. 107 269, 2021. DOI: 10.1016/j.ress.2020.107269.

[17] R. E. Bellman, *Adaptive control processes: a guided tour*. Princeton university press, 1961. DOI: 10.1515/9781400874668.

[18] G. H. Dunteman, *Principal components analysis*. Sage, 1989.

[19] L. Hawchar, C.-P. El Soueidy, and F. Schoefs, "Principal component analysis and polynomial chaos expansion for time-variant reliability problems," *Reliab Eng Syst Saf*, vol. 167, pp. 406–416, 2017. DOI: 10.1016/j.ress.2017.06.024.

[20] A. Bommert, X. Sun, B. Bischl, J. Rahnenführer, and M. Lang, "Benchmark for filter methods for feature selection in high-dimensional classification data," *Comput Stat Data Anal*, vol. 143, p. 106 839, 2020.

[21] Y. Saeys, I. Inza, and P. Larranaga, "A review of feature selection techniques in bioinformatics," *Bioinform*, vol. 23, no. 19, pp. 2507–2517, 2007. DOI: 10.1093/bioinformatics/btm344.

[22] S. Khalid, T. Khalil, and S. Nasreen, "A survey of feature selection and feature extraction techniques in machine learning," in *2014 science and information conference*, IEEE, 2014, pp. 372–378. DOI: 10.1109/SAI.2014.6918213.

[23] K. Tadist, S. Najah, N. S. Nikolov, F. Mrabti, and A. Zahi, "Feature selection methods and genomic big data: A systematic review," *J Big Data*, vol. 6, no. 1, pp. 1–24, 2019. DOI: 10.1186/s40537-019-0241-0.

[24] M. A. Hambali, T. O. Oladele, and K. S. Adewole, "Microarray cancer feature selection: Review, challenges and research directions," *International Journal of Cognitive Computing in Engineering*, vol. 1, pp. 78–97, 2020. DOI: 10.1016/j.ijcce.2020.11.001.

[25] P. Branco, L. Torgo, and R. P. Ribeiro, "A survey of predictive modeling on imbalanced domains," *ACM Comput Surv*, vol. 49, no. 2, pp. 1–50, 2016. DOI: 10.1145/2907070.

[26] A. Fernández, S. García, M. Galar, R. C. Prati, B. Krawczyk, and F. Herrera, *Learning from imbalanced data sets*. Springer, 2018, vol. 10.

[27] R. Blagus and L. Lusa, "Class prediction for high-dimensional class-imbalanced data," *BMC bioinform*, vol. 11, no. 1, pp. 1–17, 2010. DOI: 10.1186/1471-2105-11-523.

[28] D. Chicco and G. Jurman, "The advantages of the matthews correlation coefficient (mcc) over f1 score and accuracy in binary classification evaluation," *BMC genom*, vol. 21, no. 1, pp. 1–13, 2020. DOI: 10.1186/s12864-019-6413-7.

[29] B. Ellingwood, "Probability-based codified design: Past accomplishments and future challenges," *J Struct Saf*, vol. 13, no. 3, pp. 159–176, 1994. DOI: 10.1016/0167-4730(94)90024-8.

[30] *Minimum design loads for buildings and other structures*, ASCE, Reston, VA: ASCE/SEI, 2016.

[31] M. R. Sheidaii and R. Bahraminejad, "Evaluation of compression member buckling and post-buckling behavior using artificial neural network," *J Constr Steel Res*, vol. 70, pp. 71–77, 2012. DOI: 10.1016/j.jcsr.2011.10.020.

[32] Y. Pu and E. Mesbahi, "Application of artificial neural networks to evaluation of ultimate strength of steel panels," *Eng Struct*, vol. 28, no. 8, pp. 1190–1196, 2006. DOI: 10.1016/j.engstruct.2005.12.009.

[33] S. Chiew, A. Gupta, and N. Wu, "Neural network-based estimation of stress concentration factors for steel multiplanar tubular xt-joints," *J Constr Steel Res*, vol. 57, no. 2, pp. 97–112, 2001. DOI: 10.1016/S0143-974X(00)00016-X.

[34] M. Dabiri, M. Ghafouri, H. R. Raftar, and T. Björk, "Utilizing artificial neural networks for stress concentration factor calculation in butt welds," *J Constr Steel Res*, vol. 138, pp. 488–498, 2017. DOI: 10.1016/j.jcsr.2017.08.009.

[35] V. V. Degtyarev, "Neural networks for predicting shear strength of cfs channels with slotted webs," *J Constr Steel Res*, vol. 177, p. 106 443, 2021. DOI: 10.1016/j.jcsr.2020.106443.

[36] J. Rahman, K. S. Ahmed, N. I. Khan, K. Islam, and S. Mangalathu, "Data-driven shear strength prediction of steel fiber reinforced concrete beams using machine learning approach," *Eng Struct*, vol. 233, p. 111 743, 2021. DOI: 10.1016/j.engstruct.2020.111743.

[37] D.-C. Feng, W.-J. Wang, S. Mangalathu, G. Hu, and T. Wu, "Implementing ensemble learning methods to predict the shear strength of rc deep beams with/without web reinforcements," *Eng Struct*, vol. 235, p. 111 979, 2021. DOI: 10.1016/j.engstruct.2021.111979.

[38] M. Almustafa and M. Nehdi, "Machine learning model for predicting structural response of rc slabs exposed to blast loading," *Eng Struct*, vol. 221, p. 111 109, 2020. DOI: 10.1016/j.engstruct.2020.111109.

[39] M. Naser and V. Kodur, "Explainable machine learning using real, synthetic and augmented fire tests to predict fire resistance and spalling of rc columns," *Eng Struct*, vol. 253, p. 113 824, 2022. DOI: 10.1016/j.engstruct.2021.113824.

[40] J. Kiani, C. Camp, and S. Pezeshk, "On the application of machine learning techniques to derive seismic fragility curves," *Comput Struct*, vol. 218, pp. 108–122, 2019. DOI: 10.1016/j.compstruc.2019.03.004.

[41] H. D. Nguyen, J. M. LaFave, Y.-J. Lee, and M. Shin, "Rapid seismic damage-state assessment of steel moment frames using machine learning," *Eng Struct*, vol. 252, p. 113 737, 2022. DOI: 10.1016/j.engstruct.2021.113737.

[42] S.-H. Hwang, S. Mangalathu, J. Shin, and J.-S. Jeon, "Machine learning-based approaches for seismic demand and collapse of ductile reinforced concrete building frames," *J Build Eng*, vol. 34, p. 101 905, 2021. DOI: 10.1016/j.jobe.2020.101905.

[43] S. Mangalathu, H. Jang, S.-H. Hwang, and J.-S. Jeon, "Data-driven machine-learning-based seismic failure mode identification of reinforced concrete shear walls," *Eng Struct*, vol. 208, p. 110 331, 2020. DOI: 10.1016/j.engstruct.2020.110331.

[44] H. Huang and H. V. Burton, "Classification of in-plane failure modes for reinforced concrete frames with infills using machine learning," *J Build Eng*, vol. 25, p. 100 767, 2019. DOI: 10.1016/j.jobe.2019.100767.

[45] H. Koh and H. B. Blum, "Machine learning-based feature importance approach for sensitivity analysis of steel frames," *engrXiv*, 2021. DOI: 10.31224/osf.io/mvkf3.

[46] M. Fernández-Delgado, E. Cernadas, S. Barro, and D. Amorim, "Do we need hundreds of classifiers to solve real world classification problems?" *J Mach Learn Res*, vol. 15, no. 1, pp. 3133–3181, 2014. DOI: 10.5555/2627435.2697065.

[47] P. Orzechowski, W. La Cava, and J. H. Moore, "Where are we now? a large benchmark study of recent symbolic regression methods," in *Proceedings of the Genetic and Evolutionary Computation Conference*, 2018, pp. 1183–1190. DOI: 10.1145/3205455.3205539.

[48] D. H. Wolpert, "The lack of a priori distinctions between learning algorithms," *Neural comput*, vol. 8, no. 7, pp. 1341–1390, 1996. DOI: 10.1162/neco.1996.8.7.1341.

[49] A. S. Nowak and K. R. Collins, *Reliability of structures*. CRC press, 2012.

[50] T. Parr, J. D. Wilson, and J. Hamrick, "Nonparametric feature impact and importance," *arXiv preprint arXiv:2006.04750*, 2020.

[51] H. Peng, F. Long, and C. Ding, "Feature selection based on mutual information criteria of max-dependency, max-relevance, and min-redundancy," *IEEE Trans Pattern Anal Mach Intell*, vol. 27, no. 8, pp. 1226–1238, 2005. DOI: 10.1109/TPAMI.2005.159.

[52] C. Spearman, "The proof and measurement of association between two things," *Am J Psychol*, vol. 15, no. 1, pp. 72–101, 1904. DOI: 10.2307/1422689.

[53] L. Breiman, "Random forests," *Mach Learn*, vol. 45, no. 1, pp. 5–32, 2001. DOI: 10.1023/A:1010933404324.

[54] S. Lundberg and S.-I. Lee, "A unified approach to interpreting model predictions," *arXiv preprint arXiv:1705.07874*, 2017.

[55] D. W. Hosmer Jr, S. Lemeshow, and R. X. Sturdivant, *Applied logistic regression*. John Wiley & Sons, 2013.

[56] B. W. Matthews, "Comparison of the predicted and observed secondary structure of t4 phage lysozyme," *Biochim Biophys Acta, Protein Struct*, vol. 405, no. 2, pp. 442–451, 1975. DOI: 10.1016/0005-2795(75)90109-9.

[57] A. J. Izenman, *Modern multivariate statistical techniques: Regression, classification and manifold learning*. New York City, NY: Springer, 2013.

[58] F. Fu, "Fire induced progressive collapse potential assessment of steel framed buildings using machine learning," *J Constr Steel Res*, vol. 166, p. 105 918, 2020. DOI: 10.1016/j.jcsr.2019.105918.

[59] M. Sokolova, N. Japkowicz, and S. Szpakowicz, "Beyond accuracy, f-score and roc: A family of discriminant measures for performance evaluation," in *Australasian joint conference on artificial intelligence*, 2006, pp. 1015–1021. DOI: 10.1007/11941439_114.

[60] R. Melchers and A. T. Beck, *Structural reliability analysis and prediction*, 3rd. Hoboken, NJ: John Wiley & Sons Ltd, 2018.

[61] J. M. Chambers, *Graphical methods for data analysis*. CRC Press, 1983. DOI: 10.1201/9781351072304.

[62] S. G. Buonopane, "Strength and reliability of steel frames with random properties," *J Struct Eng*, vol. 134, no. 2, pp. 337–344, 2008. DOI: 10.1061/(ASCE)0733-9445(2008)134:2(337).

[63] S. Szyniszewski, "Effects of random imperfections on progressive collapse propagation," in *Structures Congress 2010*, 2010, pp. 3572–3577. DOI: 10.1061/41130(369)322.

[64] S. Shayan, K. J. Rasmussen, and H. Zhang, "On the modelling of initial geometric imperfections of steel frames in advanced analysis," *J Constr Steel Res*, vol. 98, pp. 167–177, 2014. DOI: 10.1016/j.jcsr.2014.02.016.

[65] H.-T. Thai, B. Uy, W.-H. Kang, and S. Hicks, "System reliability evaluation of steel frames with semi-rigid connections," *J Constr Steel Res*, vol. 121, pp. 29–39, 2016. DOI: 10.1016/j.jcsr.2016.01.009.

[66] H. Zhang, H. Liu, B. R. Ellingwood, and K. J. Rasmussen, "System reliabilities of planar gravity steel frames designed by the inelastic method in aisc 360-10," *J Struct Eng*, vol. 144, no. 3, p. 04 018 011, 2018. DOI: 10.1061/(ASCE)ST.1943-541X.0001991.

[67] F. S. Cardoso, H. Zhang, K. J. Rasmussen, and S. Yan, "Reliability calibrations for the design of cold-formed steel portal frames by advanced analysis," *Eng Struct*, vol. 182, pp. 164–171, 2019. DOI: 10.1016/j.engstruct.2018.12.054.

[68] R. D. Ziemian, "Advanced methods of inelastic analysis in the limit states design of steel structures.," Ph.D. dissertation, Cornell University, Ithaca, NY, 1990.

[69] S. G. Buonopane and B. W. Schafer, "Reliability of steel frames designed with advanced analysis," *J Struct Eng*, vol. 132, no. 2, pp. 267–276, 2006. DOI: 10.1061/(ASCE)0733-9445(2006)132:2(267).

[70] S. Mazzoni, F. McKenna, M. H. Scott, G. L. Fenves, *et al.*, *OpenSees command language manual*. University of California, Berkeley, 2006.

[71] T. V. Galambos and R. L. Ketter, "Columns under combined bending and thrust," *J Eng Mech Div*, vol. 85, no. 2, pp. 1–30, 1959. DOI: 10.1061/JMCEA3.0000084.

[72] B. Ellingwood, J. G. MacGregor, T. V. Galambos, and C. A. Cornell, "Probability based load criteria: Load factors and load combinations," *Journal of the Structural Division*, vol. 108, no. 5, pp. 978–997, 1982.

[73] F. M. Bartlett, R. J. Dexter, M. D. Graeser, J. J. Jelinek, B. J. Schmidt, and T. V. Galambos, "Updating standard shape material properties database for design and reliability," *Eng J AISC*, vol. 40, no. 1, pp. 2–14, 2003.

[74] J. Lindner and R. Gietzelt, "Imperfektionsannahmen für stützenschiefstellungen," *Der Stahlbau*, vol. 52, no. 4, pp. 97–101, 1984.

[75] S. Shayan, K. J. R. Rasmussen, and H. Zhang, "Probabilistic modelling of residual stress in advanced analysis of steel structures," *J Constr Steel Res*, vol. 101, pp. 407–414, 2014. DOI: 10.1016/j.jcsr.2014.05.028.

[76] J. Melcher, Z. Kala, M. Holicky, M. Fajkus, and L. Rozlivka, "Design characteristics of structural steels based on statistical analysis of metallurgical products," *J Constr Steel Res*, vol. 60, pp. 795–808, 2004. DOI: 10.1016/S0143-974X(03)00144-5.

[77] N. V. Chawla, K. W. Bowyer, L. O. Hall, and W. P. Kegelmeyer, "Smote: Synthetic minority over-sampling technique," *J Artif Intell Res*, vol. 16, pp. 321–357, 2002. DOI: 10.1613/jair.953.

[78] P. Hajibabaee, F. Pourkamali-Anaraki, and M. A. Hariri-Ardebili, "An empirical evaluation of the t-sne algorithm for data visualization in structural engineering," in *2021 20th IEEE International Conference on Machine Learning and Applications (ICMLA)*, 2021, pp. 1674–1680. DOI: 10.1109/ICMLA52953.2021.00267.

[79] J. Brownlee, *Imbalanced classification with Python: better metrics, balance skewed classes, cost-sensitive learning*. Machine Learning Mastery, 2020.

[80] H. He and E. A. Garcia, "Learning from imbalanced data," *IEEE Trans Knowl Data Eng*, vol. 21, no. 9, pp. 1263–1284, 2009. DOI: 10.1109/TKDE.2008.239.

[81] Y. Sun, A. K. Wong, and M. S. Kamel, "Classification of imbalanced data: A review," *Int J Pattern Recognit Artif Intell*, vol. 23, no. 04, pp. 687–719, 2009. DOI: 10.1142/S0218001409007326.

[82] N. V. Chawla, N. Japkowicz, and A. Kotcz, "Special issue on learning from imbalanced data sets," *ACM SIGKDD explorations newsletter*, vol. 6, no. 1, pp. 1–6, 2004. DOI: 10.1145/1007730.1007733.

[83] S. Maldonado, J. López, and C. Vairetti, "An alternative smote oversampling strategy for high-dimensional datasets," *Appl Soft Comput*, vol. 76, pp. 380–389, 2019. DOI: 10.1016/j.asoc.2018.12.024.

[84] W. El-Dakhakhni, "Data analytics in structural engineering," 2021. DOI: 10.1061/(ASCE)ST.1943-541X.0003112.

[85] T. C. Lux, L. T. Watson, T. H. Chang, Y. Hong, and K. Cameron, "Interpolation of sparse high-dimensional data," *Numer Algorithms*, vol. 88, no. 1, pp. 281–313, 2021.

[86] Y. Xu, B. Zheng, and M. Zhang, "Capacity prediction of cold-formed stainless steel tubular columns using machine learning methods," *J Constr Steel Res*, vol. 182, p. 106 682, 2021. DOI: 10.1016/j.jcsr.2021.106682.

[87] M. D'Aniello, E. M. Güneyisi, R. Landolfo, and K. Mermerdaş, "Analytical prediction of available rotation capacity of cold-formed rectangular and square hollow section beams," *Thin-Walled Structures*, vol. 77, pp. 141–152, 2014.

[88] S.-H. Kim, X. Song, C. Cho, and C.-H. Lee, "Strength prediction of steel chs x-joints via leveraging finite element method and machine learning solutions," *Journal of Constructional Steel Research*, vol. 176, p. 106 394, 2021.

[89] Z. Fang, K. Roy, B. Chen, C.-W. Sham, I. Hajirasouliha, and J. B. Lim, "Deep learning-based procedure for structural design of cold-formed steel channel sections with edge-stiffened and un-stiffened holes under axial compression," *Thin-Walled Structures*, vol. 166, p. 108 076, 2021.

[90] M. Kumar and N. Yadav, "Buckling analysis of a beam–column using multilayer perceptron neural network technique," *Journal of the Franklin Institute*, vol. 350, no. 10, pp. 3188–3204, 2013.

[91] M. Abambres, K. Rajana, K. D. Tsavdaridis, and T. P. Ribeiro, "Neural network-based formula for the buckling load prediction of i-section cellular steel beams," *Computers*, vol. 8, no. 1, p. 2, 2018.

[92] V. V. Degtyarev and K. D. Tsavdaridis, "Buckling and ultimate load prediction models for perforated steel beams using machine learning algorithms," *J Build Eng*, vol. 51, p. 104 316, 2022. DOI: doi.org/10.1016/j.jobe.2022.104316.

[93] Y. Dai, K. Roy, Z. Fang, B. Chen, G. M. Raftery, and J. B. Lim, "A novel machine learning model to predict the moment capacity of cold-formed steel channel beams with edge-stiffened and un-stiffened web holes," *J Build Eng*, vol. 53, p. 104 592, 2022. DOI: 10.1016/j.jobe.2022.104592.

[94] M. Pala, "A new formulation for distortional buckling stress in cold-formed steel members," *Journal of Constructional Steel Research*, vol. 62, no. 7, pp. 716–722, 2006.

[95] R. Tide, "Reasonable column design equations," in *Proceedings 1985 Annual Technical Session*, Bethlehem, PA: Structural Stability Research Council, 1985.

[96] R. Bjorhovde, "Columns-from theory to practice," *ENG J-AISC*, vol. 25, no. 1, pp. 21–34, 1988.

[97] T. V. Galambos, *Guide to stability design criteria for metal structures*, 5th ed. John Wiley & Sons, 1998.

[98] H. Beer and G. Schulz, "Bases théoriques des courbes européennes de flambement," *Construction Métallique*, vol. 3, pp. 37–57, 1970.

[99] J. Strating and H. Vos, "Computer simulation of the eccs buckling curve using a monte-carlo method," in *Proc. of the International Colloquium on Column STrength*, 1972.

[100] D. Sfintesco and A. Carpena, "Experimental bases of the eccs column curves, 2nd intern," in *Intern. Coll. on Stability_Introductory report, Tokyo*, (Liege, Washington), 1977, pp. 68–75.

[101] T. M. Chan, L. Gardner, and K. H. Law, "Structural design of elliptical hollow sections: A review," *Proc. of the Institution of Civil Engineers-Structures and Buildings*, vol. 163, no. 6, pp. 391–402, 2010. DOI: 10.1680/stbu.2010.163.6.391.

[102] A. Taras and R. Greiner, "New design curves for lateral–torsional buckling—proposal based on a consistent derivation," *J Const Steel Res*, vol. 66, no. 5, pp. 648–663, 2010. DOI: 10.1016/j.jcsr.2010.01.011.

[103] European Committee for Standardization, *Eurocode 3—Design of steel structures—Part 1-12: General - High strength steels*. Brussels, Belgium: EN 1993-1-12, 2007.

[104] G. Sedlacek, B. Kuhn, J. Rondal, and P. Boeraeve, "Buckling behaviour of hot-formed shs in high strength steel grade e-460," Comite international pour le developpement et l'etude de la construction tubulaire, Cidect report 2T-2/99, Altendorf, Switzerland, Tech. Rep., 1999.

[105] J.-L. Ma, T.-M. Chan, and B. Young, "Experimental investigation on stub-column behavior of cold-formed high-strength steel tubular sections," *J Struct Eng*, vol. 142, no. 5, p. 04 015 174, 2016. DOI: 10.1061/(ASCE)ST.1943-541X.0001456.

[106] J. Wang and L. Gardner, "Flexural buckling of hot-finished high-strength steel shs and rhs columns," *J Struct Eng*, vol. 143, no. 6, p. 04 017 028, 2017. DOI: 10.1061/(ASCE)ST.1943-541X.0001763.

[107] P. Guiaux, "Essais de flambement sur profils creux formes a froid, carres et circulaires," CIDECT 72/28/F, Altendorf, Switzerland, Tech. Rep., 1972.

[108] R. Bjorhovde, "Strength and behavior of cold-formed hss columns," Rep. No. 65. Edmonton, AB, Canada: Univ. of Alberta, Tech. Rep., 1977.

[109] M. Braham, M. CC, *et al.*, "Flambement des profils creux a parois minces. cas des profils rectangulaires charges axialement," CIDECT 2H 79/19. Altendorf, Switzerland: Committee for International Development and Education on Construction of Tubular Structures., Tech. Rep., 1980.

[110] P. W. Key, S. W. Hasan, and G. J. Hancock, "Column behavior of cold-formed hollow sections," *J Struct Eng*, vol. 114, no. 2, pp. 390–407, 1988. DOI: 10.1061/(ASCE)0733-9445(1988)114:2(390).

[111] G. Sedlacek, J. Rondal, P. Boeraeve, N. Stranghöner, R. Schneider, and D. Grotmann, "Buckling behaviour of a new generation of cold

formed hollow sections," Final CIDECT report 2R-2/96., Aachen University, Aachen, Germany, Tech. Rep., 1996.

[112] B. Somodi and B. Kövesdi, "Flexural buckling resistance of cold-formed hss hollow section members," *J Constr Steel Res*, vol. 128, pp. 179–192, 2017. DOI: 10.1016/j.jcsr.2016.08.014.

[113] P. Virtanen, R. Gommers, T. E. Oliphant, *et al.*, "SciPy 1.0: Fundamental Algorithms for Scientific Computing in Python," *Nature Methods*, vol. 17, pp. 261–272, 2020. DOI: 10.1038/s41592-019-0686-2.

[114] F. Pedregosa, G. Varoquaux, A. Gramfort, *et al.*, "Scikit-learn: Machine learning in python," *the Journal of machine Learning research*, vol. 12, pp. 2825–2830, 2011.

[115] J. R. Quinlan, "Induction of decision trees," *Mach Learn*, vol. 1, no. 1, pp. 81–106, 1986. DOI: 10.1007/BF00116251.

[116] W. Ayrton and J. Perry, "On struts," *The engineer*, vol. 62, no. 464–465, pp. 513–515, 1886.

[117] J. Barber and P. Birkemoe, *An experimental investigation of the column behaviour of cold-formed stress-relieved hollow structural steel sections*. Department of Civil Engineering, University of Toronto, 1978.

[118] R. M. Sully and G. J. Hancock, "Behavior of cold-formed shs beam-columns," *J Struct Eng*, vol. 122, no. 3, pp. 326–336, 1996. DOI: 10.1061/(ASCE)0733-9445(1996)122:3(326).

[119] L. Pavlovčič, B. Froschmeier, U. Kuhlmann, and D. Beg, "Finite element simulation of slender thin-walled box columns by implementing real initial conditions," *Adv Eng Softw*, vol. 44, no. 1, pp. 63–74, 2012. DOI: 10.1016/j.advengsoft.2011.05.036.

[120] SSAB, "Axial resistance of double grade (s355, s420) hollow sections manufactured by ssab, statistical evaluation based on tests," Helsinki, Finland, Tech. Rep., 2014.

[121] J. Rondal, "Contribution à l'étude de la stabilité des profils creux à parois minces," Ph.D. dissertation, Université de Liège, Faculté des sciences appliquées, 1984.

[122] Dassault Systems, *Abaqus/CAE*. Johnston, RI: Dassault Systems: V6.16, 2015.

[123] R. B. Cruise and L. Gardner, "Strength enhancements induced during cold forming of stainless steel sections," *J Constr Steel Res*, vol. 64, no. 11, pp. 1310–1316, 2008. DOI: 10.1016/j.jcsr.2008.04.014.

[124] S. Afshan, B. Rossi, and L. Gardner, "Strength enhancements in cold-formed structural sections—part i: Material testing," *J Constr Steel Res*, vol. 83, pp. 177–188, 2013. DOI: 10.1016/j.jcsr.2012.12.008.

[125] E. W. Cheney and W. A. Light, *A course in approximation theory*. American Mathematical Soc., 2009, vol. 101.

[126] O. B. Olalusi and P. O. Awoyera, "Shear capacity prediction of slender reinforced concrete structures with steel fibers using machine learning," *Engineering Structures*, vol. 227, p. 111 470, 2021. DOI: 10.1016/j.engstruct.2020.111470.

[127] H. Dabiri, A. Kheyroddin, and A. Faramarzi, "Predicting tensile strength of spliced and non-spliced steel bars using machine learning- and regression-based methods," *Construction and Building Materials*, vol. 325, p. 126 835, 2022. DOI: 10.1016/j.conbuildmat.2022.126835.

[128] H. Koh and H. B. Blum, "Machine learning-based sensitivity of steel frames with highly imbalanced and high-dimensional data," *Eng Struct*, vol. 259, p. 114 126, 2022. DOI: 10.1016/j.engstruct.2022.114126.

[129] A. Huber and L. Beedle, "Residual stress and the compressive strength of steel," Lehigh Univ Bethlehem Pa Fritz Engineering Lab, Tech. Rep., 1953.

[130] L. S. Beedle and L. Tall, "Basic column strength," *J Struct Div*, vol. 86, no. 7, pp. 139–173, 1960. DOI: 10.1061/JSDEAG.0000539.

[131] C. Jez-Gala, "Residual stresses in rolled i-sections.," *Proc Inst Civ Eng*, vol. 23, no. 3, pp. 361–378, 1962. DOI: 10.1680/iicep.1962.10874.

[132] B. W. Young, *Residual stresses in hot-rolled sections*. University of Cambridge, 1971.

[133] ECCS, "Ultimate limit state calculation of sway frames with rigid joints," *TC 8 of European Convention for Constructional Steelwork (ECCS)*, vol. No. 33, 1984.

[134] AISC, *Specification for Structural Steel Buildings ANSI/AISC 360-22*. Chicago, IL: American Institute of Steel Construction, 2022, p. 676.

[135] R. D. Ziemian and W. McGuire, "Modified tangent modulus approach, a contribution to plastic hinge analysis," *Journal of Structural Engineering*, vol. 128, no. 10, pp. 1301–1307, 2002.

[136] A. E. Surovek-Maleck and D. W. White, "Alternative approaches for elastic analysis and design of steel frames. i: Overview," *J Struct Eng*, vol. 130, no. 8, pp. 1186–1196, 2004. DOI: 10.1061/(ASCE)0733-9445(2004)130:8(1186).

[137] A. Landesmann and E. de Miranda Batista, "Advanced analysis of steel framed buildings using the brazilian standard and eurocode-3," *J Constr Steel Res*, vol. 61, no. 8, pp. 1051–1074, 2005. DOI: 10.1016/j.jcsr.2005.02.008.

[138] A. Barszcz and M. Gizejowski, "An equivalent stiffness approach for modelling the behaviour of compression members according to eurocode 3," *J Constr Steel Res*, vol. 63, no. 1, pp. 55–70, 2007. DOI: 10.1016/j.jcsr.2006.03.003.

[139] A. H. Zubydan, "A simplified model for inelastic second order analysis of planar frames," *Eng Struct*, vol. 32, no. 10, pp. 3258–3268, 2010. DOI: 10.1016/j.engstruct.2010.06.015.

[140] A. H. Zubydan, "Inelastic second order analysis of steel frame elements flexed about minor axis," *Engineering Structures*, vol. 33, no. 4, pp. 1240–1250, 2011.

[141] M. Kucukler, L. Gardner, and L. Macorini, "A stiffness reduction method for the in-plane design of structural steel elements," *Engineering Structures*, vol. 73, pp. 72–84, 2014.

[142] M. Kucukler, L. Gardner, and L. Macorini, "Development and assessment of a practical stiffness reduction method for the in-plane design of steel frames," *J Constr Steel Res*, vol. 126, pp. 187–200, 2016. DOI: 10.1016/j.jcsr.2016.06.002.

[143] B. Rosson, "Modeling the influence of residual stress on the ultimate load conditions of steel frames," in *Proceedings of the 2018 SSRC Annual Stability Conference*, 2018.

[144] B. Rosson, "Beam element material models for straightened hot rolled sections and welded HSS sections," in *Proceedings of the 2021 SSRC Annual Stability Conference*, St. Louis, MO, 2021.

[145] B. Rosson, "Major and minor axis stiffness reduction of steel beam-columns under axial compression and tension conditions," in *Proceedings of the 2017 SSRC Annual Stability Conference*, San Antonio, TX, 2017.

[146] M. R. Attalla, G. G. Deierlein, and W. McGuire, "Spread of plasticity: Quasi-plastic-hinge approach," *Journal of Structural Engineering*, vol. 120, no. 8, pp. 2451–2473, 1994.

[147] B. Rosson and R. Ziemian, "Validation study of a new inelastic material model for steel w-shapes," in *Proceedings of the 2019 SSRC Annual Stability Conference*, St. Louis, MO, 2019.

[148] L. Duan and W. Chen, "A yield surface equation for doubly symmetrical sections," *Eng Struct*, vol. 12, no. 2, pp. 114–119, 1990. DOI: 10.1016/0141-0296(90)90016-L.

[149] L. Schaper, T. Tankova, L. S. Silva, and M. Knobloch, "A novel residual stress model for welded i-sections," *J Constr Steel Res*, vol. 188, p. 107 017, 2022. DOI: 10.1016/j.jcsr.2021.107017.

[150] S. Santathadaporn and W. Chen, *Interaction curves for sections under combined biaxial bending and axial force*. Weld Res Counc, 1970.

[151] L. Ingvarsson, "Cold-forming residual stresses effect on buckling," 1975.

[152] C. Weng and T. Pekoz, "Residual stresses in cold-formed steel members," *Journal of Structural Engineering*, vol. 116, pp. 1611–1625, 1990.

[153] E. de M Batista and F. Rodrigues, "Residual stress measurements on cold-formed profiles," *Experimental Techniques*, vol. 16, no. 5, pp. 25–29, 1992.

[154] B. W. Schafer and T. Pekoz, "Computational modeling of cold-formed steel: Characterizing geometric imperfections and residual stresses," *J Constr Steel Res*, vol. 47, pp. 193–210, 1998. DOI: 10.1016/S0143-974X(98)00007-8.

[155] R. Spoorenberg, H. Snijder, and J. Hoenderkamp, "Experimental investigation of residual stresses in roller bent wide flange steel sections," *Journal of Constructional Steel Research*, vol. 66, pp. 737–747, 2010.

[156] J. Ma, T. Chan, and B. Young, "Material properties and residual stresses of cold-formed high strength steel hollow sections," *Journal of Constructional Steel Research*, vol. 109, pp. 152–165, 2015.

[157] L. Tong, G. Hou, Y. Chen, F. Zhou, K. Shen, and A. Yang, "Experimental investigation on longitudinal residual stresses for cold-formed thick-walled square hollow sections," *Journal of Constructional Steel Research*, vol. 73, pp. 105–116, 2012.

[158] Y. Wang, G. Li, and S. Chen, "The assessment of residual stresses in welded high strength steel box sections," *Journal of Constructional Steel Research*, vol. 76, pp. 93–99, 2012.

[159] X. Zhang, S. Liu, M. Zhao, and S. Chiew, "Comparative experimental study of hot-formed, hot-finished and cold-formed rectangular hollow sections," *Case Studies in Structural Engineering*, vol. 6, pp. 115–129, 2016.

[160] ASTM, "Standard test method for determining residual stresses by the hole-drilling strain-gage method," in *E 837-20a*, Philadelphia, Pa.: ASTM International, 2020.

[161] M. Beghini, L. Bertini, and P. Raffaelli, "An account of plasticity in the hole-drilling method of residual stress measurement," *The Journal of Strain Analysis for Engineering Design*, vol. 30, no. 3, pp. 227–233, 1995.

[162] M. Clarin and O. Lagerqvist, "Residual stresses in square hollow sections made of high strength steel," *Fourth International Conference on Advances in Steel Structures*, vol. 76, pp. 1577–1582, 2005.

[163] G. Schajer, "Application of finite element calculations to residual stress measurements," *Journal of Engineering Materials and Technology*, 1981.

[164] G. Schajer and E. Altus, "Stress calculation error analysis for incremental hole-drilling residual stress measurements," *Journal of Engineering Materials and Technology*, 1996.

[165] A. Ghasemi and M. Mohammadi, "Residual stress measurement of fiber metal laminates using incremental hole-drilling technique in consideration of the integral method," *International Journal of Mechanical Sciences*, vol. 114, pp. 246–256, 2016.

[166] Y. Li, J. Wu, B. Qiang, S. Zhou, W. Liu, and C. Yao, "Measurements of residual stresses in a welded orthotropic steel deck by the hole-drilling method considering stress biaxiality," *Engineering Structures*, vol. 230, p. 111 690, 2021.

[167] G. Schajer and P. Whitehead, *Hole-Drilling Method for Measuring Residual Stresses*. Morgan & Claypool Publishers, 2018.

[168] T. N. TN, "Measurement of residual stresses by the hole-drilling* strain gage method," 1993.

[169] A. Scaramangas, R. P. Goff, and R. Leggatt, "On the correction of residual stress measurements obtained using the centre-hole method," *Strain*, vol. 18, no. 3, pp. 88–97, 1982.

[170] Y. Xia and H. Blum, "Experimental study on residual stresses in press-braked advanced high-strength cold-formed steel lipped angles by sectioning method," *Proceedings of the Cold-Formed Steel Research Consortium Colloquium*, 2022.

[171] EN 1993-1-3, *Eurocode 3: Design of Steel Structures - Part 1-3: General rules - Supplementary rules for cold-formed members and sheeting*. European Committee for Standardisation, 2006.

[172] ACI Committee 318, *Building Code Requirements for Structural Concrete and Commentary on Building Code Requirements for Structural Concrete (ACI 318R-14)*. ACI, 2014.

[173] EN 1993-1-5, *Eurocode 3: Design of Steel Structures - Part 1-5: Plated Structural Elements*. European Committee for Standardisation, 2009.

[174] AITC, *Timber Construction Manual*. American Institute of Timber Construction, 2012.

[175] ANSI/AWC, *National Design Specification for Wood Construction*. American National Standards Institute/American Wood Council, 2018.

[176] ANSI/TPI, *National design standard for metal plate connected wood truss construction*. American National Standards Institute/Truss Plate Institute, 2014.

[177] AS 4084, *Steel Storage Racking*. Standards Australia, 2012.

[178] L. Gardner and X. Yun, "Description of stress-strain curves for cold-formed steels," *Constr Build*, vol. 189, pp. 527–538, 2018. DOI: 10.1016/j.conbuildmat.2018.08.195.

[179] W. Ramberg and W. R. Osgood, "Description of stress-strain curves by three parameters," Washington, D.C., USA, Tech. Rep. No. 902, 1943.

[180] B. Rossi, S. Afshan, and L. Gardner, "Strength enhancements in cold-formed structural sections—part ii: Predictive models," *J Constr Steel Res*, vol. 83, pp. 189–196, 2013. DOI: 10.1016/j.jcsr.2012.12.007.

[181] L. Gardner, N. Saari, and F. Wang, "Comparative experimental study of hot-rolled and cold-formed rectangular hollow sections," *Thin-Walled Struct*, vol. 48, no. 7, pp. 495–507, 2010. DOI: 10.1016/j.tws.2010.02.003.

[182] S. W. Liu, G. L. Gao, and R. D. Ziemian, "Improved line-element formulations for the stability analysis of arbitrarily shaped open-section beam-columns," *Thin-Walled Struct*, vol. 141, pp. 526–539, 2019. DOI: 10.1016/j.tws.2019.106290.

[183] R. D. Ziemian, W. McGuire, and S. W. Liu, *MASTAN2*. 2019.

[184] Z. Li and B. W. Schafer, "Buckling analysis of cold-formed steel members with general boundary conditions using cufsm conventional and constrained finite strip methods," in *International Specialty Conference on Cold-Formed Steel Structures*, 2010.

[185] J. E. Akin, *Finite element analysis concepts: Via solidworks*. World Scientific, 2010.

[186] Lysaght Professionals, *Zeds and Cees user's guide for design and installation professionals*. 2014.

[187] ClarkDietrich, *ClarkDietrich COLD-FORMED STEEL C-STUDS*. 2021.

[188] M. Theofanous, T. M. Chan, and L. Gardner, "Flexural behaviour of stainless steel oval hollow sections," *Thin-Walled Structures*, vol. 47, pp. 776–787, 2009.

[189] P. Natario, N. Silvestre, and D. Camotim, "Computational modelling of flange crushing in cold-formed steel sections," *Thin-Walled Struct*, vol. 84, pp. 393–405, 2014. DOI: 10.1016/j.tws.2014.07.006.

[190] P. Keerthan and M. Mahendran, "Improved shear design rules for lipped channel beams with web openings," *J Constr Steel Res*, vol. 97, pp. 127–142, 2014. DOI: 10.1016/j.jcsr.2014.01.011.

[191] C. Pham, "Shear buckling of plates and thin-walled channel sections with holes," *J Constr Steel Res*, vol. 128, pp. 800–811, 2017. DOI: 10.1016/j.jcsr.2016.10.013.

[192] C. Buchanan, O. Zhao, E. Real, and L. Gardner, "Cold-formed stainless steel chs beam-columns–testing, simulation and design," *Eng Struct*, vol. 213, p. 110 270, 2020. DOI: 10.1016/j.engstruct.2020.110270.

[193] D. K. Pham, C. Pham, and G. Hancock, "Parametric study for shear design of cold-formed channels with elongated web openings," *J Constr Steel Res*, vol. 172, p. 106 222, 2020. DOI: 10.1016/j.jcsr.2020.106222.

[194] N. Silvestre and D. Camotim, "Gbt-based analysis of the distortional post-buckling behaviour of cold-formed steel z-section columns and beams," in *Thin-walled structures*, CRC press, 2004, pp. 243–250.

[195] P. B. Dinis, D. Camotim, and N. Silvestre, "Fem-based analysis of the local-plate/distortional mode interaction in cold-formed steel lipped channel columns," *Comput Struct*, vol. 85, no. 19-20, pp. 1461–1474, 2007. DOI: 10.1016/j.compstruc.2007.02.013.

[196] A. Landesmann, D. Camotim, and C. Basaglia, "Distortional post-buckling behavior and strength of cold-formed steel columns: How does the cross-section geometry affect it?" In *Proceedings of the Annual Stability Conference Structural Stability Research Council, St. Louis, Missouri*, 2013.

[197] V. M. Zeinoddini and B. W. Schafer, "Simulation of geometric imperfections in cold-formed steel members using spectral repre-

sentation approach," *Thin-Walled Struct*, vol. 60, pp. 105–117, 2012. DOI: 10.1016/j.tws.2012.07.001.

[198] P. W. Key and G. J. Hancock, "A theoretical investigation of the column behaviour of cold-formed square hollow sections," *Thin-Walled Struct*, vol. 16, no. 1-4, pp. 31–64, 1993. DOI: 10.1016/0263-8231(93)90040-H.

[199] W. Liu, K. J. Rasmussen, and H. Zhang, "Modelling and probabilistic study of the residual stress of cold-formed hollow steel sections," *Eng Struct*, vol. 150, pp. 986–995, 2017. DOI: 10.1016/j.engstruct.2017.08.004.

[200] A. Mutafi, N. Yidris, M. Ishak, and R. Zahari, "An investigation on longitudinal residual strains distribution of thin-walled press-braked cold formed steel sections using 3d fem technique," *Heliyon*, vol. 4, no. 11, e00937, 2018. DOI: 10.1016/j.heliyon.2018.e00937.

[201] C. D. Moen, T. Igusa, and B. W. Schafer, "Prediction of residual stresses and strains in cold-formed steel members," *Thin-Walled Struct*, vol. 46, pp. 1274–1289, 2008. DOI: 10.1016/j.tws.2008.02.002.

[202] E. J. Sippel and H. B. Blum, "Structural analysis of steel structures with non-symmetric members," *Eng Struct*, vol. 245, p. 112 739, 2021. DOI: 10.1016/j.engstruct.2021.112739.

[203] H. B. Blum and K. J. R. Rasmussen, "Experimental and numerical study of connection effects in long-span cold-formed steel double channel portal frames," *J Constr Steel Res*, vol. 155, pp. 480–491, 2019. DOI: 10.1016/j.jcsr.2018.11.013.

[204] A. M. S. Freitas, F. T. Souza, and M. S. R. Freitas, "Analysis and behavior of steel storage drive-in racks," *Thin-Walled Struct*, vol. 48, pp. 110–117, 2010. DOI: 10.1016/j.tws.2009.09.003.

[205] D. C. Fratamico, S. Torabian, X. Zhao, and K. J. R. Rasmussen, "Experimental study on the composite action in sheathed and bare built-up cold-formed steel columns," *Thin-Walled Struct*, vol. 127, pp. 290–305, 2018. DOI: 10.1016/j.tws.2018.02.002.

[206] Rinchen and K. J. Rasmussen, "Behaviour and modelling of connections in cold-formed steel single c-section portal frames," *Thin-Walled Structures*, vol. 143, p. 106 233, 2019. DOI: 10.1016/j.tws.2019.106233.

[207] J. B. Lim and D. A. Nethercot, "Ultimate strength of bolted moment-connections between cold-formed steel members," *Thin-Walled Struct*, vol. 41, no. 11, pp. 1019–1039, 2003. DOI: 10.1016/S0263-8231(03)00045-4.

[208] J. B. Lim, G. J. Hancock, G. C. Clifton, C. H. Pham, and R. Das, "Dsm for ultimate strength of bolted moment-connections between cold-formed steel channel members," *J Constr Steel Res*, vol. 117, pp. 196–203, 2016. DOI: 10.1016/j.jcsr.2015.10.005.

[209] D. T. Phan, S. M. Mojtabaei, I. Hajirasouliha, T. Lau, and J. B. Lim, "Design and optimization of cold-formed steel sections in bolted moment connections considering bimoment," *J Struct Eng*, vol. 146, no. 8, p. 04 020 153, 2020. DOI: 10.1061/(ASCE)ST.1943-541X.0002715.

[210] S. M. Mojtabaei, J. Becque, and I. Hajirasouliha, "Local buckling in cold-formed steel moment-resisting bolted connections: Behavior, capacity, and design," *J Struct Eng*, vol. 146, no. 9, p. 04 020 167, 2020. DOI: 10.1061/(ASCE)ST.1943-541X.0002730.

[211] V. Natesan and M. Madhavan, "Structural performance on bolted sleeved connections between two cfs channel sections subjected to combined bending and shear," vol. 20, pp. 794–812, 2019. DOI: 10.1016/j.istruc.2019.06.026.

[212] S. M. Mojtabaei, J. Becque, and I. Hajirasouliha, "Behavior and design of cold-formed steel bolted connections subjected to combined actions," *J Struct Eng*, vol. 147, no. 4, p. 04 021 013, 2021. DOI: 10.1061/(ASCE)ST.1943-541X.0002966.

[213] X. Chen, H. Blum, K. Roy, P. Pouladi, A. Uzzaman, and J. B. Lim, "Cold-formed steel portal frame moment-resisting joints: Behaviour, capacity and design," *J Constr Steel Res*, vol. 183, p. 106 718, 2021.

[214] C. Zhu, K. J. R. Rasmussen, and S. Yan, "Generalized component model for structural steel joints," *J Constr Steel Res*, vol. 153, pp. 330–342, 2019. DOI: 10.1016/j.jcsr.2018.10.026.

[215] A. Uzzaman, J. B. Lim, D. Nash, J. Rhodes, and B. Young, "Web crippling behaviour of cold-formed steel channel sections with offset web holes subjected to interior-two-flange loading," *Thin-Walled Struct*, vol. 50, no. 1, pp. 76–86, 2012. DOI: 10.1016/j.tws.2011.09.009.

[216] Y. Lian, A. Uzzaman, J. B. Lim, G. Abdelal, D. Nash, and B. Young, "Effect of web holes on web crippling strength of cold-formed steel channel sections under end-one-flange loading condition–part i: Tests and finite element analysis," *Thin-Walled Struct*, vol. 107, pp. 443–452, 2016. DOI: 10.1016/j.tws.2016.06.025.

[217] S. H. Pham, C. H. Pham, and G. J. Hancock, "Direct strength method of design for channel sections in shear with square and circular web holes," *J Struct Eng*, vol. 143, no. 6, p. 04 017 017, 2017. DOI: 10.1061/(ASCE)ST.1943-541X.0001765.

[218] D. K. Pham, C. H. Pham, S. H. Pham, and G. J. Hancock, "Experimental investigation of high strength cold-formed channel sections in shear with rectangular and slotted web openings," *J Constr Steel Res*, vol. 165, p. 105 889, 2020. DOI: 10.1016/j.jcsr.2019.105889.

[219] S. H. Pham, C. H. Pham, C. A. Rogers, and G. J. Hancock, "Shear strength experiments and design of cold-formed steel channels with web holes," *J Struct Eng*, vol. 146, no. 1, p. 04 019 173, 2020. DOI: 10.1061/(ASCE)ST.1943-541X.0002464.

[220] F. S. Cardoso, H. Zhang, K. J. R. Rasmussen, and S. Yan, "Reliability calibrations for the design of cold-formed steel portal frames by advanced analysis," *Eng Struct*, vol. 182, pp. 164–171, 2019. DOI: 10.1016/j.engstruct.2018.12.054.

[221] F. S. Cardoso, H. Zhang, and K. J. R. Rasmussen, "System reliability-based criteria for the design of steel storage rack frames by advanced analysis: Part ii – reliability analysis and design applications," *Thin-Walled Struct*, vol. 141, pp. 725–739, 2019. DOI: 10.1016/j.tws.2019.03.021.

[222] R. D. Ziemian, J. C. B. Abreu, M. D. Denavit, and T. L. Denavit, "Three-dimensional benchmark problems for design by advanced analysis: Impact of twist," *J Struct Eng*, vol. 144, no. 12, p. 04 018 220, 2018. DOI: 10.1061/\%28ASCE\%29ST.1943-541X.0002224.

[223] M. D. Denavit, "Expanded benchmark studies on the aisc direct analysis method," in *Proceedings of the Annual Stability Conference*, Louisville, Kentucky, 2021.

[224] ANSYS, Inc., *ANSYS Mechanical*. R2, 2021.

[225] Computers and Structures, Inc., *SAP2000*. 2021.

[226] RISA tech, Inc., *Rapid Interactive Structural Analysis – Version 19-General Reference*. 2020.

[227] EN 1993-1-4, *Eurocode 3: Design of Steel Structures - Part 1-4: General rules - Supplementary rules for stainless steels*. European Committee for Standardisation, 2006.

[228] P. Kyvelou, L. Gardner, and D. A. Nethercot, "Finite element modelling of composite cold-formed steel flooring systems," *Eng Struct*, vol. 158, pp. 28–42, 2018. DOI: 10.1016/j.engstruct.2017.12.024.

[229] L. Gardner and M. Ashraf, "Structural design for non-linear metallic materials," *Eng Struct*, vol. 28, pp. 926–934, 2006. DOI: 10.1016/j.engstruct.2005.11.001.

[230] P. Kyvelou, "Structural behaviour of composite cold-formed steel systems," Ph.D. dissertation, Imperial College, London, UK, 2017.

[231] Boutell, B., and Hui, C., *Imperfections used in finite element analysis*. No. A3. Report, 2013.

[232] J. Yin and X. Du, "Active learning with generalized sliced inverse regression for high-dimensional reliability analysis," *Struct Saf*, vol. 94, p. 102 151, 2022. DOI: 10.1016/j.strusafe.2021.102151.

[233] Y. Li, C.-Y. Chen, and W. W. Wasserman, "Deep feature selection: Theory and application to identify enhancers and promoters," *J Comput Biol*, vol. 23, no. 5, pp. 322–336, 2016. DOI: 10.1089/cmb.2015.0189.